

Perturbative dynamics and relativistic effects of a dyonic Kalb–Ramond black hole

A. A. Araújo Filho^{1,2,3,*}

¹*Departamento de Física, Universidade Federal da Paraíba,
Caixa Postal 5008, 58051-970, João Pessoa, Paraíba, Brazil.*

²*Departamento de Física, Universidade Federal de Campina Grande Caixa Postal 10071,
58429-900 Campina Grande, Paraíba, Brazil.*

³*Center for Theoretical Physics, Khazar University,
41 Mehseti Street, Baku, AZ-1096, Azerbaijan.*

(Dated: May 28, 2026)

Abstract

We investigate perturbative dynamics, tidal effects, and relativistic frequency shifts in a dyonic Kalb–Ramond black hole generated by a Lorentz–violating antisymmetric tensor background. The geometry is controlled by the mass M , the electric charge Q , the magnetic charge p , and the Lorentz–violating parameter ℓ , with the dyonic sector entering through the effective combination $P_\ell^2 = Q^2/(1-\ell)^2 + p^2/(1-2\ell)$. First, we analyze the gravitational Doppler effect for radial signal exchange between freely falling and static observers, showing how the dyonic charges weaken the redshift by shifting the frequency ratio toward unity. We then compute the radial and angular tidal forces in a freely falling frame and determine the characteristic radii at which the usual stretching and compression patterns are reversed. The gravitational time delay is also evaluated for null trajectories, showing that the electric and magnetic sectors reduce the delay relative to the reference configuration. In the perturbative sector, we derive the scalar, vector, tensor, and spinor effective potentials and compute the corresponding quasinormal frequencies through the sixth–order WKB method. The numerical spectra indicate that the Lorentz–violating parameter gives the dominant correction, increasing the oscillation frequencies and modifying the damping rates, while the dyonic charges produce milder shifts. Finally, the time–domain profiles confirm the presence of damped quasinormal ringing followed by late–time power–law tails.

arXiv:2605.28580v1 [gr-qc] 27 May 2026

*Electronic address: dilto@fisica.ufc.br

Contents

I. Introduction	3
II. The dyonic Kalb–Ramond black hole	6
III. The gravitational Doppler effect	8
IV. Tidal forces	11
A. Tidal forces for static and spherically symmetric spacetimes	11
B. Radial tidal force	13
C. Angular tidal forces	14
V. Time delay	17
VI. The corresponding effective potentials	20
A. Bosonic sector	20
B. Fermionic sector	21
VII. Quasinormal frequencies	22
A. Scalar perturbations	22
B. Vector perturbations	26
C. Tensor perturbations	28
D. Spinor perturbations	32
VIII. Time–domain solution	36
A. Scalar perturbations	39
B. Vector perturbations	40
C. Tensor perturbations	41
D. Spinor perturbations	43
IX. Conclusion	45
Acknowledgments	51
Data Availability Statement	51
References	51

I. INTRODUCTION

At energies where quantum-gravitational effects may leave residual traces in the effective space-time description, local Lorentz invariance need not remain an exact symmetry. This possibility has motivated extensive work on effective frameworks in which tiny deviations from Lorentz symmetry are incorporated without abandoning the low-energy field-theoretic setting [1–5]. In many such scenarios, the symmetry is broken spontaneously: a dynamical field acquires a nonzero vacuum configuration and thereby selects privileged spacetime directions. The bumblebee model realizes this mechanism in one of its simplest forms. In this approach, a vector field develops a vacuum expectation value, and its coupling to gravity produces well-defined modifications of the general relativistic dynamics [6–11].

Bumblebee scenarios offer a direct realization of spontaneous Lorentz breaking in gravitational physics. Instead of assuming Lorentz invariance as an exact microscopic symmetry, these models allow it to arise only as an effective low-energy limit. Their formulation was influenced by string-motivated mechanisms in which tensor fields acquire nonzero vacuum values [4, 12], by vector-tensor modifications of Einstein gravity [13], and by effective field-theory descriptions that incorporate fixed background configurations associated with symmetry breaking [3, 7]. In the bumblebee case, the dynamics of the vector field B_μ are governed by a potential $V(B_\mu B^\mu \mp b^2)$, which forces the field toward a vacuum state with $B_\mu B^\mu = \pm b^2$. Once this vacuum configuration is reached, spacetime contains a distinguished direction, and local Lorentz symmetry is spontaneously violated [6, 7]. The excitations around this vacuum split into massless Nambu-Goldstone modes, which may behave as photon-like degrees of freedom [7], and massive modes, which measure deviations away from the fixed-norm vacuum condition [6].

Bumblebee gravity has also been extended to curved spacetimes, where the nonzero vacuum value of the vector field participates directly in the gravitational dynamics and changes the resulting geometry [14]. Black hole spacetimes constitute one of the main arenas in which these effects have been examined. The solution proposed in Ref. [15] became a reference point for many later analyses, ranging from quantum processes near the horizon [16, 17] and Lorentz-violating corrections to gravitational wave propagation [18] to quasinormal spectra [19] and even-parity perturbations [20]. Further extensions have incorporated topological-defect-like structures [21], non-commutative effects [22, 23], cosmological constant contributions [24], cosmological applications [25], nonlinear electrodynamics [26], and approximate rotating geometries [27, 28]. Light propagation in these spacetimes has likewise been analyzed through weak- and strong-deflection methods, including Gauss-Bonnet techniques, direct geodesic treatments, perturbative rotation schemes, and Newman-Janis-based constructions [29–32]. More recently, mass-ratio inspirals in bumblebee gravity have also been used to extract phenomenological constraints on Lorentz-violating parameters [33].

A different route to Lorentz–symmetry breaking can be built from an antisymmetric tensor field instead of a vector degree of freedom. The Kalb–Ramond field, introduced as a rank–two tensor in bosonic string theory [34], provides such a framework when it is coupled nonminimally to gravity. Under suitable conditions, this tensor sector develops a nonzero vacuum configuration, so that spacetime no longer remains directionally neutral [35, 36]. In this case, the preferred background (similarly to the bumblebee case) is generated by the vacuum structure of the antisymmetric field, and Lorentz symmetry is broken spontaneously.

Tensor–based extensions of Lorentz–violating gravity have led to what is commonly referred to as Kalb–Ramond gravity, in which the antisymmetric sector replaces the vector order parameter used in bumblebee models. In this context, black hole configurations have formed a central class of exact backgrounds. The static and spherically symmetric geometry obtained in Ref. [37] provided the first explicit realization (as far as we know), after which the motion of particles and fields around this spacetime was investigated in Ref. [38]. This solution has since been used to study quasinormal modes [39], greybody factors and transmission bounds [40], weak– and strong–field lensing signatures [41], phenomenological bounds on the symmetry-breaking scale [42], and gravitational wave emission from periodic orbits [43]. Related analyses have also addressed circular motion and quasi–periodic oscillations [44], accretion modeled by Vlasov gases [45], particle production effects [17, 46], and neutrino propagation [47, 48].

On the other hand, charged Kalb–Ramond black holes were later obtained in Ref. [49], opening the way to analyses of their thermodynamic properties, emission mechanisms, geometric observables and energy extraction [50–55]. A non–commutative version of the Kalb–Ramond solution was subsequently proposed in Ref. [56]. The class of available geometries has also been enlarged by solutions surrounded by anisotropic fluids [57], ModMax sectors [58, 59], clouds of strings [60], perfect fluid dark matter [61], dyonic ModMax fields [62], and other configurations [63, 64]. Rotating extensions have provided another direction of development. In the slow–rotation regime, the corresponding shadow profiles were investigated in Ref. [65], while the scalar, vector, and tensor quasinormal spectra were computed in Ref. [66]. Kalb–Ramond black holes carrying a global–monopole contribution have also been derived, further broadening the range of Lorentz–violating compact objects described by this antisymmetric tensor sector [67].

More recently, the Kalb–Ramond black hole sector was extended through the construction of a charged dyonic configuration [68]. Despite this progress, the dynamical and observational properties of this spacetime remain largely unexplored. In particular, its quasinormal spectrum, time–domain response, tidal behavior, and related relativistic effects have not yet been analyzed. The present work addressed this gap by developing an initial study of the gravitational properties associated with the dyonic Kalb–Ramond black hole.

Black holes now serve as remarkable laboratories for probing deviations from general relativity

in the strong-field regime. This role has become even more prominent after the direct detection of gravitational waves by the LIGO and VIRGO collaborations, which made it possible to test compact-object dynamics through interferometric observations [69]. At the same time, the Event Horizon Telescope has resolved horizon-scale structures associated with supermassive compact objects, which provides independent observational access to the geometry of the near-horizon region [70, 71].

Black hole perturbations provide a direct set of probes for the geometry of compact objects. In the post-merger stage, the distorted remnant approaches equilibrium through a ringdown signal governed by complex quasinormal frequencies [72–78]. The real part fixes the oscillation scale, whereas the imaginary part controls the damping time. Since both quantities are determined by the background metric, the perturbing sector, and the boundary conditions, any Lorentz-violating modification of the black hole spacetime can shift the ringdown spectrum. Quasinormal modes therefore offer a useful diagnostic for distinguishing modified geometries from their general-relativistic counterparts. Their role is also connected with other observables, since relations have been explored between the eikonal quasinormal spectrum and shadow properties [79], as well as between perturbative dynamics and greybody emission [80, 81]. Although the identification of individual modes in present gravitational wave data remains debated [82].

This study examines the dynamics of perturbations, tidal responses, and relativistic frequency shifts in a dyonic Kalb–Ramond black hole that arises from a Lorentz-violating antisymmetric tensor background. The spacetime is specified by the mass M , the electric charge Q , the magnetic charge p , and the Lorentz-violating parameter ℓ . The charge contribution enters the metric through the effective combination $P_\ell^2 = Q^2/(1-\ell)^2 + p^2/(1-2\ell)$, which allows the electric and magnetic sectors to be treated within a single radial structure. We first consider the gravitational Doppler shift associated with radial signal propagation between a freely falling emitter and a static receiver. The analysis shows that the dyonic charges drive the frequency ratio closer to unity, thereby reducing the redshift effect relative to less charged configurations. We then evaluate the tidal-force components in the freely falling frame. This calculation identifies the radii where the standard radial stretching and angular compression can change character due to the combined influence of Q , p , and ℓ . The null propagation sector is addressed through the gravitational time delay, for which the electric and magnetic charges lower the delay with respect to the reference case. The perturbative part of the work is devoted to scalar, vector, tensor, and spinor test fields. For each sector, we obtain the corresponding effective potential and compute the quasinormal frequencies with the sixth-order WKB approximation. The numerical results show that the Lorentz-violating parameter produces the strongest changes in the spectra, increasing the real oscillation frequencies and altering the damping rates. By contrast, the electric and magnetic charges generate weaker corrections. The time-domain evolution supports the frequency-domain analysis, displaying an intermediate stage

in which damped quasinormal ringing dominates and a late-time regime in which power-law tails control the signal.

II. THE DYONIC KALB–RAMOND BLACK HOLE

The starting point of our analysis is a dyonic black hole spacetime arising from a Lorentz-violating theory driven by a Kalb–Ramond background. In this setup, the gravitational dynamics receive contributions from the antisymmetric tensor $B_{\mu\nu}$ through a nonminimal curvature coupling. The action for the theory is written as

$$S = \int d^4x \sqrt{-g} \left[\frac{1}{2\kappa} (R - 2\Lambda + \xi B_\mu{}^\rho B_{\nu\rho} R^{\mu\nu}) - \frac{1}{12} H_{\mu\nu\rho} H^{\mu\nu\rho} - V(X) + \mathcal{L}_m \right], \quad (1)$$

with, in this notation, $\kappa = 8\pi G/c^4$ fixes the gravitational coupling, Λ represents the cosmological constant, and ξ sets the strength of the nonminimal interaction between the Kalb–Ramond tensor and the Ricci curvature. The antisymmetric field $B_{\mu\nu}$ gives rise to the field strength $H_{\mu\nu\rho} = \partial_\mu B_{\nu\rho} + \partial_\nu B_{\rho\mu} + \partial_\rho B_{\mu\nu}$. The self-interaction potential is written as a function of $X = B_{\mu\nu} B^{\mu\nu} \pm b^2$, where b^2 fixes the vacuum scale of the tensor field. Once $V(X)$ reaches its minimum, the Kalb–Ramond field develops a nonzero vacuum expectation value, thereby selecting preferred spacetime directions and inducing spontaneous Lorentz–symmetry breaking.

The electromagnetic contribution is also deformed by the Kalb–Ramond background. In this sector, the gauge field A_μ enters through the Maxwell tensor $F_{\mu\nu} = \partial_\mu A_\nu - \partial_\nu A_\mu$, and its dynamics are supplemented by two curvature-independent interactions involving $B_{\mu\nu}$ and $F_{\mu\nu}$. With these contributions included, the matter Lagrangian takes the form

$$\mathcal{L}_m = -\frac{1}{2\kappa} (F_{\mu\nu} F^{\mu\nu} + \gamma_1 B^{\mu\nu} B^{\rho\sigma} F_{\mu\nu} F_{\rho\sigma} + \gamma_2 B^{\mu\nu} B_{\mu\nu} F_{\rho\sigma} F^{\rho\sigma}), \quad (2)$$

with the constants γ_1 and γ_2 determine the strength of the two electromagnetic nonminimal interactions. Varying the full action with respect to $g_{\mu\nu}$, A_μ , and $B_{\mu\nu}$ yields the corresponding gravitational, gauge field, and Kalb–Ramond equations, namely

$$G_{\mu\nu} + \Lambda g_{\mu\nu} = \kappa (T_{\mu\nu}^{\text{KR}} + T_{\mu\nu}^{\text{EM}}), \quad (3)$$

$$\nabla_\nu [(1 + \gamma_2 B_{\alpha\beta} B^{\alpha\beta}) F^{\mu\nu} + \gamma_1 B_{\alpha\beta} F^{\alpha\beta} B^{\mu\nu}] = 0, \quad (4)$$

and

$$\nabla_\alpha H^{\mu\nu\alpha} - 4B^{\mu\nu} V'(X) - \frac{2\gamma_1}{\kappa} B_{\alpha\beta} F^{\alpha\beta} F^{\mu\nu} - \frac{2\gamma_2}{\kappa} F_{\alpha\beta} F^{\alpha\beta} B^{\mu\nu} - \frac{\xi}{\kappa} (R^\mu{}_\alpha B^{\nu\alpha} - R^\nu{}_\alpha B^{\mu\alpha}) = 0. \quad (5)$$

The resulting field equations make the coupling structure explicit: the Maxwell and Kalb–Ramond contributions interact through the parameters γ_1 and γ_2 , while their backreaction on the metric provides an additional gravitational channel connecting both sectors.

We consider a static, spherically symmetric geometry described by the line element

$$ds^2 = -F(r)dt^2 + \frac{dr^2}{F(r)} + r^2 (d\theta^2 + \sin^2 \theta d\phi^2). \quad (6)$$

A pseudo-electric ansatz is adopted for the Kalb–Ramond background, so that the tensor field carries only a temporal–radial component,

$$B_{\mu\nu} = \begin{pmatrix} 0 & \frac{b}{\sqrt{2}}\sqrt{F(r)G(r)} & 0 & 0 \\ -\frac{b}{\sqrt{2}}\sqrt{F(r)G(r)} & 0 & 0 & 0 \\ 0 & 0 & 0 & 0 \\ 0 & 0 & 0 & 0 \end{pmatrix}. \quad (7)$$

Notice that, with this choice, the Kalb–Ramond invariant is fixed by $B_{\mu\nu}B^{\mu\nu} = -b^2$, while its field strength vanishes, $H_{\mu\nu\rho} = 0$. The dyonic sector is incorporated through the gauge potential $A_\mu = (-\Phi(r), 0, 0, p \cos \theta)$, where p denotes the magnetic charge. This potential produces the electric component $F_{tr} = -F_{rt} = -\Phi'(r)$ and the magnetic component $F_{\theta\phi} = -F_{\phi\theta} = -p \sin \theta$.

We restrict the solution to the asymptotically non–flat branch with $\Lambda = 0$ and choose the quadratic potential $V(X) = \lambda X^2/2$. The vacuum configuration follows from $X = 0$, which also gives $V(X) = 0$ and $V'(X) = 0$. An exact dyonic black hole geometry arises after fixing the electromagnetic couplings according to $\gamma_1 + \gamma_2 = \xi/2$ and $\gamma_2 = \xi/(2b^2\xi - 2)$. The Lorentz–violating contribution is encoded in the dimensionless parameter $\ell = \xi b^2/2$. After expressing the solution in terms of the physical electric charge Q , the electrostatic potential becomes $\Phi(r) = -Q/[(1 - \ell)r]$. The corresponding metric function takes the form

$$F(r) = \frac{1}{1 - \ell} - \frac{2M}{r} + \frac{Q^2}{(1 - \ell)^2 r^2} + \frac{p^2}{(1 - 2\ell)r^2}. \quad (8)$$

The resulting dyonic Kalb–Ramond black hole geometry can therefore be written as [68]

$$ds^2 = - \left[\frac{1}{1 - \ell} - \frac{2M}{r} + \frac{Q^2}{(1 - \ell)^2 r^2} + \frac{p^2}{(1 - 2\ell)r^2} \right] dt^2 + \left[\frac{1}{1 - \ell} - \frac{2M}{r} + \frac{Q^2}{(1 - \ell)^2 r^2} + \frac{p^2}{(1 - 2\ell)r^2} \right]^{-1} dr^2 + r^2 d\Omega^2, \quad (9)$$

Here, $d\Omega^2 = d\theta^2 + \sin^2 \theta d\phi^2$ denotes the metric on the unit two–sphere. The constants M , Q , and p characterize, respectively, the mass, electric charge, and magnetic charge of the black hole, whereas ℓ parametrizes the correction generated by the Kalb–Ramond background. When the Lorentz–violating contribution is switched off, $\ell \rightarrow 0$, the metric function becomes $F(r) \rightarrow 1 - 2M/r + (Q^2 + p^2)/r^2$, and the usual dyonic Reissner–Nordström spacetime is recovered. The sector $p = 0$ gives the electrically charged Kalb–Ramond black hole, while the choice $Q = p = 0$ leaves the neutral Lorentz–violating Kalb–Ramond solution.

The subsequent analysis employs the metric (9) as the fixed background for the study of perturbations, time–domain evolution, tidal behavior, and relativistic effects in the dyonic Kalb–Ramond geometry.

III. THE GRAVITATIONAL DOPPLER EFFECT

We next consider the gravitational Doppler shift produced by radial photon exchange in the dyonic Kalb–Ramond spacetime. The emitting source follows a freely falling trajectory, whereas the receivers are taken to be static observers. Our treatment uses the usual construction of local velocity measurements and frequency ratios in static black hole geometries [83–87]. It also generalizes the charged Kalb–Ramond case studied in Ref. [88] by including both electric and magnetic charges. Since the metric function has already been specified in Eq. (8), we only introduce here the effective dyonic charge parameter

$$\mathcal{P}_\ell^2 \equiv \frac{Q^2}{(1-\ell)^2} + \frac{p^2}{1-2\ell}. \quad (10)$$

In this notation, the roots of $F(r) = 0$ determine the horizon radii,

$$r_\pm = (1-\ell) \left[M \pm \sqrt{M^2 - \frac{Q^2}{(1-\ell)^3} - \frac{p^2}{(1-\ell)(1-2\ell)}} \right], \quad (11)$$

where these radii exist when the radicand remains non-negative. The limiting case in which this quantity vanishes defines the extremal dyonic Kalb–Ramond configuration.

For radial motion along a timelike trajectory, the four velocity normalization $u_\mu u^\mu = -1$ leads to

$$-F(r)\dot{t}^2 + \frac{\dot{r}^2}{F(r)} = -1. \quad (12)$$

Here, a dot indicates differentiation with respect to the proper time τ . The static character of the geometry implies the existence of a conserved energy per unit rest mass, written as

$$E = F(r)\dot{t}. \quad (13)$$

In this manner, the radial geodesic equation turns out to be

$$\dot{r}^2 = E^2 - F(r). \quad (14)$$

For a particle that starts from rest at $r = b$, the conserved energy satisfies $E^2 = F(b)$. When the initial position is taken in the asymptotic region, the non-flat behavior of the spacetime at large r instead leads to

$$E^2 = F(\infty) = \frac{1}{1-\ell}. \quad (15)$$

In the exterior domain, a static observer assigns to the infalling particle a local velocity defined by

$$d\tau^2 = -F(r)dt^2 (1 - v^2), \quad v^2 = \frac{1}{F(r)^2} \left(\frac{dr}{dt} \right)^2. \quad (16)$$

Combining Eqs. (13) and (14), the velocity becomes

$$v^2(r) = \frac{E^2 - F(r)}{E^2}. \quad (17)$$

For an infalling particle whose initial rest position is placed at spatial infinity, Eq. (17) simplifies to

$$v^2(r) = (1 - \ell) \left(\frac{2M}{r} - \frac{\mathcal{P}_\ell^2}{r^2} \right). \quad (18)$$

At the outer horizon, $r = r_+$, the metric function vanishes, $F(r_+) = 0$. Consequently, the local free-fall speed satisfies $v(r_+) = 1$, meaning that a static observer outside the black hole measures the infalling particle as reaching the speed of light at the horizon.

In the interval bounded by the inner and outer horizons, $r_- < r < r_+$, the radial and temporal coordinates interchange their causal roles. The free-fall motion in this interior domain is therefore characterized by the velocity

$$V^2(r) = \frac{E^2}{E^2 - F(r)}. \quad (19)$$

For $E^2 = 1/(1 - \ell)$, this yields

$$V^2(r) = \frac{r^2}{(1 - \ell)(2Mr - \mathcal{P}_\ell^2)}. \quad (20)$$

The minimum of $V(r)$ is obtained from $dV^2/dr = 0$, giving

$$r_m = \frac{\mathcal{P}_\ell^2}{M} = \frac{1}{M} \left[\frac{Q^2}{(1 - \ell)^2} + \frac{p^2}{1 - 2\ell} \right]. \quad (21)$$

For non-extremal black holes, this radius remains inside the region $r_- < r < r_+$ and marks the transition between the redshift and blueshift sectors of the interior geometry.

We now describe radial photon propagation by introducing the wave vector $k^\mu = dx^\mu/d\sigma$, where σ is an affine parameter along the null trajectory. The condition $k_\mu k^\mu = 0$ then gives

$$g_{\mu\nu} k^\mu k^\nu = 0. \quad (22)$$

The conserved photon energy gives

$$k^t = \frac{\omega_\infty}{F(r)}, \quad k^r = \pm \omega_\infty, \quad (23)$$

with the plus sign describes an outgoing radial photon, whereas the minus sign refers to an ingoing one. For an observer with u^μ , the measured photon frequency is

$$\omega = -k_\mu u^\mu. \quad (24)$$

We initially consider the photon emitted by the freely falling source and detected by a static observer located at the release radius $r = b$. Using the initial rest condition $E^2 = F(b)$, the frequency measured at reception relative to the emitted one is

$$\frac{\omega_b^{(r)}}{\omega_{\text{ff}}^{(s)}} = 1 - v(r). \quad (25)$$

When the source approaches the event horizon, $v \rightarrow 1$, and we have

$$\frac{\omega_b^{(r)}}{\omega_{\text{ff}}^{(s)}} \rightarrow 0. \quad (26)$$

Consequently, the radiation produced by the freely falling emitter is observed in the exterior frame with an unbounded redshift.

On the other hand, when the photon is sent from the static observer at $r = b$ and detected by the freely falling observer, the corresponding frequency ratio is

$$\frac{\omega_{\text{ff}}^{(r)}}{\omega_b^{(s)}} = \frac{1}{1 + v(r)}. \quad (27)$$

In addition, at the outer horizon, this ratio becomes

$$\frac{\omega_{\text{ff}}^{(r)}}{\omega_b^{(s)}} \longrightarrow \frac{1}{2}. \quad (28)$$

This nonreciprocal behavior is a direct consequence of the horizon causal structure. Once the emitter crosses the outer horizon, photons directed outward no longer return to the exterior region, while photons sent inward from outside the black hole may still intercept the falling observer.

In the interior domain, $r_- < r < r_+$, an observer placed between the two horizons measures the frequency ratio as

$$\frac{\omega_{r_0}^{(r)}}{\omega_{\text{ff}}^{(s)}} = (1 + V^{-1})^{-1}. \quad (29)$$

Also, taking into account Eq. (20), we obtain

$$\frac{\omega_{r_0}^{(r)}}{\omega_{\text{ff}}^{(s)}} = \left[1 + \sqrt{(1 - \ell) \left(\frac{2M}{r} - \frac{\mathcal{P}_\ell^2}{r^2} \right)} \right]^{-1}. \quad (30)$$

Since the metric function vanishes at the two horizons, $F(r_\pm) = 0$, the interior velocity satisfies $V(r_\pm) = 1$. In this manner,

$$\frac{\omega_{r_0}^{(r)}}{\omega_{\text{ff}}^{(s)}} \longrightarrow \frac{1}{2}, \quad r \rightarrow r_\pm. \quad (31)$$

The frequency ratio reaches its lowest value at $r = r_m$. In the interval $r_+ > r > r_m$, the signal received by the interior observer is Doppler redshifted, which reflects the expansion like character of the region between the horizons. After crossing r_m , namely for $r_m > r > r_-$, the ratio starts to grow again, indicating a Doppler blueshift as the trajectory approaches the Cauchy horizon.

When the Lorentz-violating parameter is removed, $\ell \rightarrow 0$, Eq. (30) recovers the dyonic Reissner–Nordström expression,

$$\frac{\omega_{r_0}^{(r)}}{\omega_{\text{ff}}^{(s)}} \longrightarrow \left[1 + \sqrt{\frac{2M}{r} - \frac{Q^2 + p^2}{r^2}} \right]^{-1}. \quad (32)$$

Notice that by setting $p = 0$ gives the purely electric Kalb–Ramond case. If both charges vanish, $Q = p = 0$, the inner horizon disappears and the redshift–blueshift transition inside the black hole ceases to occur. In that neutral sector, the Doppler behavior is restricted to the exterior gravitational redshift produced by the single event horizon.

Figure 1 displays the radial profile of the frequency ratio $\omega_{r_0}^{(r)}/\omega_{\text{ff}}^{(s)}$ obtained from Eq. (30) for several dyonic configurations with $Q = p$, fixing $M = 1$ and $\ell = 0.1$. The ratio remains below

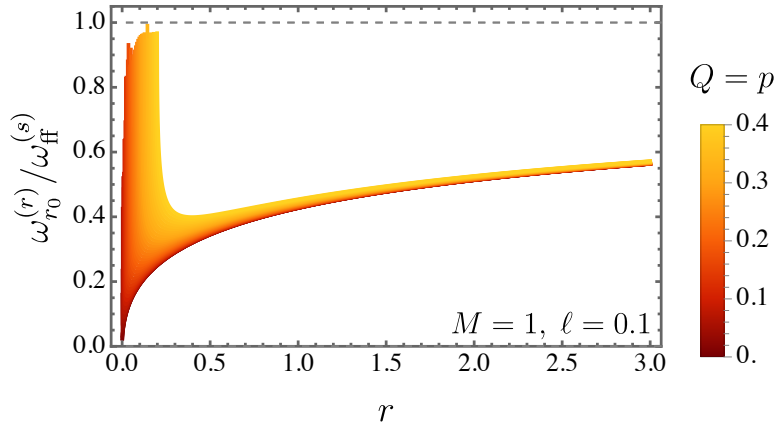


Figure 1: Radial behavior of the gravitational Doppler frequency ratio $\omega_{r_0}^{(r)}/\omega_{ff}^{(s)}$ for different values of the dyonic charge parameter, assuming $Q = p$, with $M = 1$ and $\ell = 0.1$.

unity in the plotted branch, indicating a redshift of the received signal with respect to the emitted one. The electric and magnetic charges enter through P_ℓ^2 and reduce the square root contribution. Consequently, larger values of $Q = p$ shift the curves upward and bring the ratio closer to unity, corresponding to a weaker Doppler redshift. The minimum occurs near $r_m = P_\ell^2/M$, which separates the redshift and blueshift sectors in the two-horizon region.

IV. TIDAL FORCES

We study the tidal response of a neutral test body falling radially into the dyonic Kalb–Ramond black hole. In this setting, tidal forces are obtained from the relative acceleration of nearby geodesics and give a local characterization of the curvature acting on an extended body [89–92]. In charged black hole spacetimes, the standard Schwarzschild behavior – radial stretching together with angular compression – may be altered, since charge terms can change the sign of the tidal components near the inner region [83, 93]. For the dyonic Kalb–Ramond solution, the electric and magnetic charges contribute with distinct Lorentz–violating factors. As a result, the radii at which the radial and angular tidal sectors change sign depend explicitly on ℓ .

A. Tidal forces for static and spherically symmetric spacetimes

The analysis is based on the static, spherically symmetric metric given in Eq. (9). To keep the tidal expressions compact, we define the effective dyonic charge parameter

$$P_\ell^2 \equiv \frac{Q^2}{(1-\ell)^2} + \frac{p^2}{1-2\ell}, \quad (33)$$

and with this definition, the metric function in Eq. (8) assumes the compact form

$$F(r) = \frac{1}{1-\ell} - \frac{2M}{r} + \frac{P_\ell^2}{r^2}. \quad (34)$$

When the Lorentz-violating parameter is removed, $\ell \rightarrow 0$, the effective charge reduces to $P_\ell^2 \rightarrow Q^2 + p^2$, and the metric returns to the usual dyonic Reissner–Nordström form. The sector with $p = 0$ instead gives the electrically charged Kalb–Ramond solution.

The tidal acceleration is governed by the geodesic deviation equation,

$$\frac{D^2 \eta^\mu}{D\tau^2} + R^\mu{}_{\nu\alpha\beta} u^\nu \eta^\alpha u^\beta = 0, \quad (35)$$

where, in this expression, η^μ denotes the separation vector between neighboring geodesics, while u^μ represents the four-velocity of the radially infalling observer. For a timelike radial trajectory, the condition $u_\mu u^\mu = -1$ yields

$$-F(r)\dot{t}^2 + \frac{\dot{r}^2}{F(r)} = -1, \quad (36)$$

where the dot denotes differentiation with respect to the proper time τ . The time translation symmetry of the spacetime leads to a conserved energy per unit rest mass, given by

$$E = F(r)\dot{t}. \quad (37)$$

Now, let us substitute Eq. (37) into Eq. (36), so that

$$\dot{r}^2 = E^2 - F(r). \quad (38)$$

For inward radial motion, the radial component satisfies $\dot{r} < 0$. In the freely falling frame, one may introduce the following comoving orthonormal tetrad:

$$e_0^\mu = \left(\frac{E}{F(r)}, -\sqrt{E^2 - F(r)}, 0, 0 \right), \quad (39)$$

$$e_1^\mu = \left(-\frac{\sqrt{E^2 - F(r)}}{F(r)}, E, 0, 0 \right), \quad (40)$$

$$e_2^\mu = \left(0, 0, \frac{1}{r}, 0 \right), \quad e_3^\mu = \left(0, 0, 0, \frac{1}{r \sin \theta} \right). \quad (41)$$

This local frame satisfies

$$g_{\mu\nu} e_a^\mu e_b^\nu = \eta_{\hat{a}\hat{b}}, \quad \eta_{\hat{a}\hat{b}} = \text{diag}(-1, 1, 1, 1). \quad (42)$$

It is worth mentioning that the tetrad is normalized so that $e_0^\mu = u^\mu$. After Eq. (35) is projected onto this locally inertial frame, the radial component of the tidal acceleration takes the form

$$\frac{D^2 \eta^{\hat{1}}}{D\tau^2} = -\frac{F''(r)}{2} \eta^{\hat{1}}, \quad (43)$$

whereas the angular components satisfy

$$\frac{D^2 \eta^{\hat{i}}}{D\tau^2} = -\frac{F'(r)}{2r} \eta^{\hat{i}}, \quad \hat{i} = \hat{2}, \hat{3}. \quad (44)$$

For the metric function considered here, (34), the derivatives are

$$F'(r) = \frac{2M}{r^2} - \frac{2P_\ell^2}{r^3}, \quad F''(r) = -\frac{4M}{r^3} + \frac{6P_\ell^2}{r^4}. \quad (45)$$

In other words, the projected equations give the radial stretching/compression and the transverse tidal response measured by the freely falling observer.

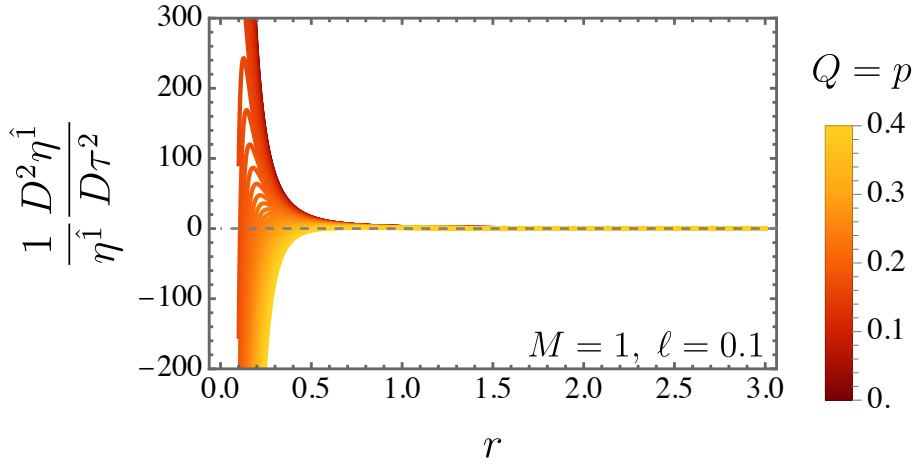


Figure 2: Radial tidal force for different values of the dyonic charges with $Q = p$, fixing $M = 1$ and $\ell = 0.1$. The dashed horizontal line separates radial stretching from radial compression.

B. Radial tidal force

Substituting the derivatives in Eq. (45) into the general radial relation (43), one obtains the radial tidal acceleration for the dyonic Kalb–Ramond geometry as

$$\frac{D^2 \eta^{\hat{1}}}{D\tau^2} = \left(\frac{2M}{r^3} - \frac{3P_\ell^2}{r^4} \right) \eta^{\hat{1}}. \quad (46)$$

Equivalently, it can be written as

$$\frac{D^2 \eta^{\hat{1}}}{D\tau^2} = \frac{1}{2} \left[\frac{4M}{r^3} - \frac{6}{r^4} \left(\frac{Q^2}{(1-\ell)^2} + \frac{p^2}{1-2\ell} \right) \right] \eta^{\hat{1}}. \quad (47)$$

The term $2M/r^3$ represents the Schwarzschild part and gives rise to radial stretching. The charge dependent term, $-3P_\ell^2/r^4$, has the opposite sign and becomes dominant sufficiently close to the central region. Then, in direct analogy with the Reissner–Nordström spacetime, the radial tidal component can pass from stretching to compression.

Figure 2 shows the radial tidal acceleration per unit separation, $(D^2 \eta^{\hat{1}}/D\tau^2)/\eta^{\hat{1}}$, as a function of r for several dyonic configurations with $Q = p$, keeping $\ell = 0.1$ fixed. Positive values describe radial stretching, while negative values correspond to radial compression. At large distances, the Schwarzschild–like contribution $2M/r^3$ controls the behavior, so the radial tidal force remains positive. Moving toward smaller radii, the dyonic term $-3P_\ell^2/r^4$ grows faster and eventually reverses the sign of the force. The transition occurs at $R_0^{\text{rad}} = 3P_\ell^2/(2M)$. Larger values of the common charge $Q = p$ increase P_ℓ^2 , displacing the radial maximum and the zero crossing radius toward larger values of r .

Here, notice that the radial tidal force vanishes when

$$\frac{2M}{r^3} - \frac{3P_\ell^2}{r^4} = 0, \quad (48)$$

which gives us

$$R_0^{\text{rad}} = \frac{3P_\ell^2}{2M} = \frac{3}{2M} \left[\frac{Q^2}{(1-\ell)^2} + \frac{p^2}{1-2\ell} \right]. \quad (49)$$

The sign of the radial tidal component changes at R_0^{rad} . For $r > R_0^{\text{rad}}$, the acceleration is positive, and an extended body is pulled apart along the radial direction. For $r < R_0^{\text{rad}}$, the same component becomes negative, so the radial separation between neighboring parts of the body decreases. The stationary point of Eq. (46) is obtained by imposing $d[(D^2\eta^{\hat{1}}/D\tau^2)/\eta^{\hat{1}}]/dr = 0$, which gives

$$R_{\text{max}}^{\text{rad}} = \frac{2P_\ell^2}{M} = \frac{2}{M} \left[\frac{Q^2}{(1-\ell)^2} + \frac{p^2}{1-2\ell} \right]. \quad (50)$$

The radial tidal component attains its maximum at this point. For $P_\ell^2 > 0$, larger values of Q or p move both R_0^{rad} and $R_{\text{max}}^{\text{rad}}$ outward. The parameter ℓ modifies these characteristic radii through the weights $(1-\ell)^{-2}$ and $(1-2\ell)^{-1}$. For $0 < \ell < 1/2$, the magnetic sector is amplified by the factor $(1-2\ell)^{-1}$, whereas the electric sector is scaled by $(1-\ell)^{-2}$. Around $\ell = 0$, the two charge sectors acquire the same leading-order relative correction. However, as ℓ approaches $1/2$, the magnetic contribution increases more strongly.

If we take into account the limit $\ell \rightarrow 0$, Eq. (46) becomes

$$\frac{D^2\eta^{\hat{1}}}{D\tau^2} \rightarrow \left[\frac{2M}{r^3} - \frac{3(Q^2 + p^2)}{r^4} \right] \eta^{\hat{1}}, \quad (51)$$

which coincides with the dyonic Reissner–Nordström expression. In the neutral limit, $Q = p = 0$, the result reduces to the Schwarzschild form,

$$\frac{D^2\eta^{\hat{1}}}{D\tau^2} = \frac{2M}{r^3} \eta^{\hat{1}}. \quad (52)$$

In the neutral configuration, the local radial tidal component is independent of ℓ . Nevertheless, the Lorentz–violating parameter still affects the spacetime through the constant contribution appearing in $F(r)$, and this modifies the position of the horizon.

C. Angular tidal forces

The transverse tidal sector follows from Eq. (44). After inserting the derivatives listed in Eq. (45), the angular components take the form

$$\frac{D^2\eta^{\hat{i}}}{D\tau^2} = \left(\frac{P_\ell^2}{r^4} - \frac{M}{r^3} \right) \eta^{\hat{i}}, \quad \hat{i} = \hat{2}, \hat{3}. \quad (53)$$

Equivalently,

$$\frac{D^2\eta^{\hat{i}}}{D\tau^2} = \frac{1}{r^4} \left[\frac{Q^2}{(1-\ell)^2} + \frac{p^2}{1-2\ell} - Mr \right] \eta^{\hat{i}}, \quad \hat{i} = \hat{2}, \hat{3}. \quad (54)$$

Notice that the angular tidal force vanishes at

$$R_0^{\text{ang}} = \frac{P_\ell^2}{M} = \frac{1}{M} \left[\frac{Q^2}{(1-\ell)^2} + \frac{p^2}{1-2\ell} \right], \quad (55)$$

and its corresponding minimum occurs at

$$R_{\min}^{\text{ang}} = \frac{4P_\ell^2}{3M} = \frac{4}{3M} \left[\frac{Q^2}{(1-\ell)^2} + \frac{p^2}{1-2\ell} \right]. \quad (56)$$

The angular tidal component changes sign at R_0^{ang} . Outside this radius, $r > R_0^{\text{ang}}$, the transverse acceleration is negative, so the body undergoes compression along the angular directions. Inside this radius, $r < R_0^{\text{ang}}$, the angular component becomes positive. Therefore, sufficiently close to the inner region, the dyonic charge contribution overturns the Schwarzschild transverse compression and produces angular stretching.

For a particle starting from rest in the asymptotic region, the conserved energy satisfies

$$E^2 = F(\infty) = \frac{1}{1-\ell}. \quad (57)$$

The radial turning point is fixed by the condition $E^2 = F(r)$, or equivalently by solving

$$R_{\text{stop}}^2 = \frac{P_\ell^2}{2M} = \frac{1}{2M} \left[\frac{Q^2}{(1-\ell)^2} + \frac{p^2}{1-2\ell} \right]. \quad (58)$$

For $P_\ell^2 > 0$, the corresponding radii read

$$R_{\text{stop}} < R_0^{\text{ang}} < R_{\min}^{\text{ang}} < R_0^{\text{rad}} < R_{\max}^{\text{rad}}.$$

Because the falling body evolves from larger toward smaller radii, this hierarchy shows that the radial sector changes sign before the angular one. Along the trajectory, the radial tidal component first attains its maximum at R_{\max}^{rad} and then crosses zero at R_0^{rad} . The transverse component follows a different sequence: it reaches its minimum at R_{\min}^{ang} and becomes zero only afterward, at R_0^{ang} .

Figure 3 presents the angular tidal acceleration per unit separation, $(D^2\eta^{\hat{i}}/D\tau^2)/\eta^{\hat{i}}$, as a function of r for several dyonic configurations with $Q = p$, while keeping $\ell = 0.1$. Unlike the radial component, the angular sector is negative in the large-distance region, which corresponds to transverse compression. This behavior is controlled by the Schwarzschild-like contribution $-M/r^3$. At smaller radii, the dyonic term \mathcal{P}_ℓ^2/r^4 grows faster and may overcome the Schwarzschild part, turning the transverse compression into angular stretching. The zero of the angular component occurs at $R_0^{\text{ang}} = \mathcal{P}_\ell^2/M$, whereas the maximum compression is reached at $R_{\min}^{\text{ang}} = 4\mathcal{P}_\ell^2/(3M)$. As the common charge $Q = p$ increases, \mathcal{P}_ℓ^2 also increases, pushing both characteristic radii outward.

When the Lorentz-violating parameter is switched off, $\ell \rightarrow 0$, Eq. (53) takes the dyonic Reissner–Nordström form,

$$\frac{D^2\eta^{\hat{i}}}{D\tau^2} \rightarrow \left[\frac{Q^2 + p^2}{r^4} - \frac{M}{r^3} \right] \eta^{\hat{i}}, \quad \hat{i} = \hat{2}, \hat{3}. \quad (59)$$

In the neutral limit, $Q = p = 0$, the angular sector reduces to the Schwarzschild transverse compression,

$$\frac{D^2\eta^{\hat{i}}}{D\tau^2} = -\frac{M}{r^3} \eta^{\hat{i}}, \quad \hat{i} = \hat{2}, \hat{3}. \quad (60)$$

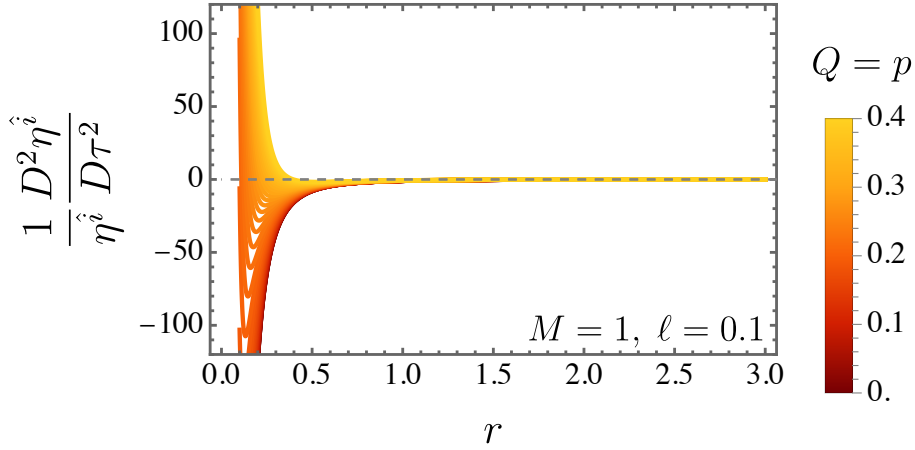


Figure 3: Angular tidal force for different values of the dyonic charges with $Q = p$, fixing $M = 1$ and $\ell = 0.1$. The dashed horizontal line separates angular compression from angular stretching.

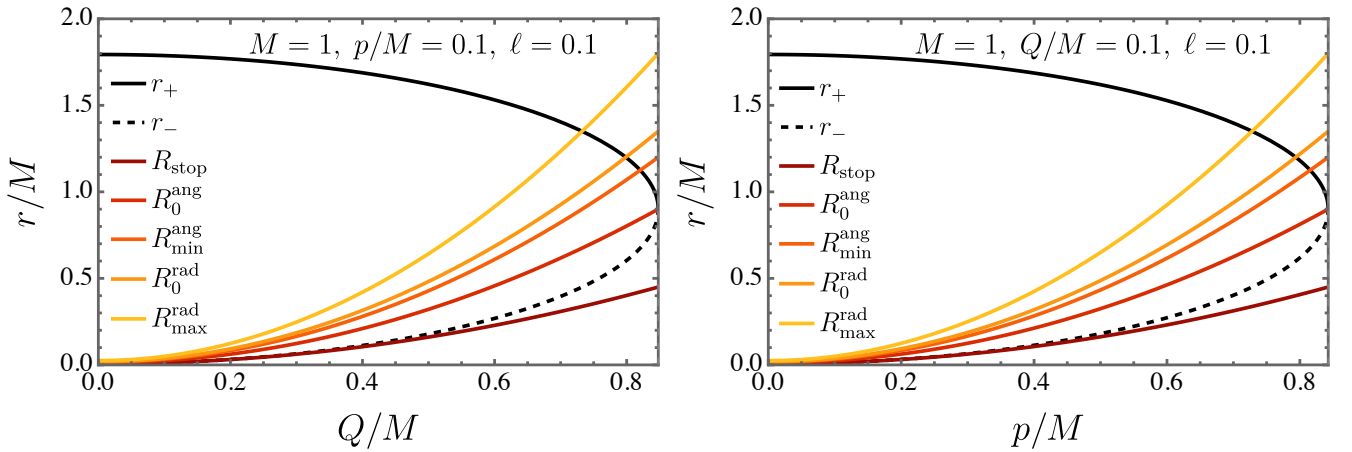


Figure 4: Horizon radii and characteristic tidal radii as functions of the charge parameters. On the left panel, the variation with Q/M for fixed $p/M = 0.1$. On the right one, the variation with p/M for fixed $Q/M = 0.1$. In both panels we set $M = 1$ and $\ell = 0.1$, while the vertical dashed line marks the extremal limit where $r_+ = r_-$.

Figure 4 compares the horizon positions with the main tidal radii in the electric and magnetic sectors. The left panel varies Q/M at fixed $p/M = 0.1$, while the right panel varies p/M with $Q/M = 0.1$. In both panels, a larger charge increases the effective combination \mathcal{P}_ℓ^2 , moving R_{stop} , R_0^{ang} , $R_{\text{min}}^{\text{ang}}$, R_0^{rad} , and $R_{\text{max}}^{\text{rad}}$ to larger values of r . The horizons exhibit the opposite trend: r_+ moves inward and r_- moves outward, so the two roots approach each other as the extremal limit is approached. The vertical dashed line identifies the critical charge at which the horizons coincide. Throughout the allowed interval, the hierarchy $R_{\text{stop}} < R_0^{\text{ang}} < R_{\text{min}}^{\text{ang}} < R_0^{\text{rad}} < R_{\text{max}}^{\text{rad}}$ remains unchanged, indicating that an infalling body encounters the radial sign reversal before the angular one.

V. TIME DELAY

The present discussion follows the approach of Ref. [94]. We begin by formulating photon motion in a generic static and spherically symmetric spacetime, instead of introducing the time delay expression directly. Since light rays follow null geodesics, their trajectories are fixed by the geodesic equations together with the condition $ds^2 = 0$. If the null curve is parameterized by λ , the spacetime symmetries generate conserved quantities along the photon path. In particular, the Killing field associated with time translations defines the conserved photon energy,

$$E = F(r) \frac{dt}{d\lambda}, \quad (61)$$

where the spherical symmetry provides a second conserved quantity, namely the photon angular momentum. Restricting the trajectory to the equatorial plane, $\theta = \pi/2$, this constant may be written as

$$L = r^2 \sin^2 \theta \frac{d\phi}{d\lambda}. \quad (62)$$

The photon trajectory is completed by the null constraint imposed on the four velocity. This condition follows from the metric Lagrangian \mathcal{L} and relates the radial motion to the conserved quantities E and L . Once written in this form, the geodesic system contains all the ingredients needed for the later computation of the gravitational time delay. Using the Lagrangian formulation, we get

$$\mathcal{L} = g_{\mu\nu} dx^\mu dx^\nu = F(r) \left(\frac{dt}{d\lambda} \right)^2 - \frac{1}{F(r)} \left(\frac{dr}{d\lambda} \right)^2 - r^2 \left(\frac{d\theta}{d\lambda} \right)^2 - r^2 \sin^2 \theta \left(\frac{d\phi}{d\lambda} \right)^2. \quad (63)$$

Owing to spherical symmetry, the motion can be restricted without loss of generality to the equatorial plane, $\theta = \pi/2$. With this choice, the geodesic system is reduced to the variables r and ϕ , together with the constants E and L , which determine the radial and angular evolution of the light ray

$$\frac{1}{2} \left(\frac{dr}{d\lambda} \right)^2 + \frac{1}{2} F(r) \left[\frac{L^2}{r^2} + \mathcal{L} \right] = \frac{1}{2} \left(\frac{dr}{d\lambda} \right)^2 + V(r) = \frac{1}{2} E^2. \quad (64)$$

In a static and spherically symmetric geometry, the radial part of the null geodesic equations can be written in the form of an effective one dimensional motion. After the constants of motion are introduced, the radial evolution is governed by a single function whose zeros determine the possible turning points of the photon trajectory. This function plays the role of an effective potential and, for the geometry under consideration, is given by

$$V(r) = \frac{F(r)}{2} \left[\frac{L^2}{r^2} + \mathcal{L} \right]. \quad (65)$$

The impact parameter is introduced as the length scale fixed by the conserved quantities, $b = |L/E|$. For photons, the null condition sets the norm of the four velocity to zero, so the Lagrangian contribution \mathcal{L} drops out of the radial constraint. After this restriction is applied to the lightlike

trajectory, the radial equation assumes the reduced form

$$\frac{dr}{dt} = \frac{dr}{d\lambda} \frac{d\lambda}{dt} = \pm F(r) \sqrt{1 - b^2 \frac{F(r)}{r^2}}. \quad (66)$$

For lightlike motion, the constraint $\mathcal{L} = 0$ eliminates the norm contribution from the geodesic system, while the conserved energy enters through Eq. (61). The resulting radial equation contains two branches, distinguished by the sign \pm . These branches describe the two portions of the photon trajectory: one in which the photon approaches the compact object and another in which it moves away from it. During the incoming part, r decreases until the orbit reaches the closest-approach radius r_0 . At this point, the radial derivative changes sign, and the photon continues along the outgoing branch. With this interpretation, the trajectory is described by the two relations

$$\frac{dr}{dt} = -F(r) \sqrt{1 - b^2 \frac{F(r)}{r^2}} < 0. \quad (67)$$

The null orbit separates into an ingoing and an outgoing portion. Along the ingoing segment, the radial coordinate decreases until the photon reaches the closest approach radius r_0 , where the radial motion turns around. After this turning point, the trajectory follows the outgoing branch, and r increases as the photon moves away from the gravitational source. In this split description, the radial geodesic equations are written as

$$\frac{dr}{dt} = F(r) \sqrt{1 - b^2 \frac{F(r)}{r^2}} > 0, \quad (68)$$

After crossing the point of closest approach r_0 , the photon follows the outgoing branch, and the radial coordinate increases until the ray reaches the observer at $r = r_O$; also, $b = r_0/\sqrt{F(r_0)}$ is the impact parameter. The source is located at $r = r_S$, while the detector is placed at $r = r_O$. The coordinate time collected over the ingoing and outgoing parts of the trajectory contains the delay produced by the gravitational field. Using the prescription of Ref. [94], this time delay is expressed as

$$\begin{aligned} \Delta T &= T - T_0 \\ &= - \int_{r_S}^{r_0} \frac{dr}{F(r) \sqrt{1 - \frac{b^2 F(r)}{r^2}}} + \int_{r_0}^{r_O} \frac{dr}{F(r) \sqrt{1 - \frac{b^2 F(r)}{r^2}}} - T_0 \\ &= \int_{r_0}^{r_S} \frac{dr}{F(r) \sqrt{1 - \frac{b^2 F(r)}{r^2}}} + \int_{r_0}^{r_O} \frac{dr}{F(r) \sqrt{1 - \frac{b^2 F(r)}{r^2}}} - \sqrt{r_S^2 - r_0^2} - \sqrt{r_O^2 - r_0^2}. \end{aligned} \quad (69)$$

In the absence of gravitational effects, the propagation time for a light ray emitted at r_S , detected at r_O , and passing through the closest-approach radius r_0 is given by the corresponding flat-space result

$$T_0 = \sqrt{r_S^2 - r_0^2} + \sqrt{r_O^2 - r_0^2}. \quad (70)$$

When curvature effects are included, the coordinate travel time acquires an additional contribution, which is identified with the gravitational time delay. This correction grows when the source

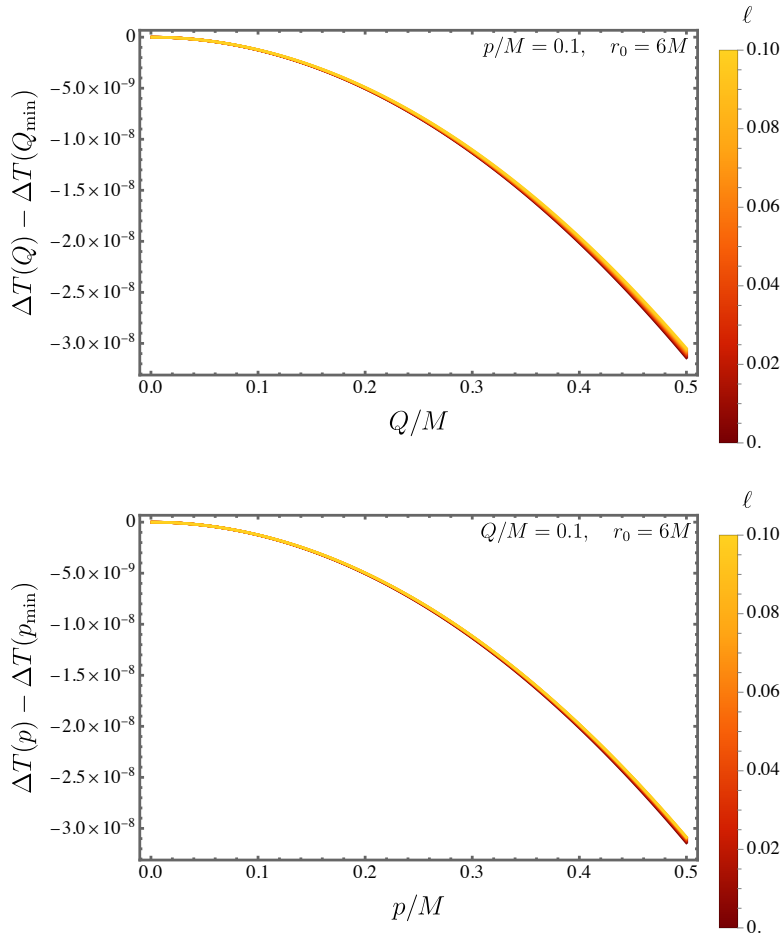


Figure 5: Shifted time delay as a function of the normalized electric and magnetic charges. Upper panel: $\Delta T(Q) - \Delta T(Q_{\min})$ versus Q/M for fixed $p/M = 0.1$. Bottom panel: $\Delta T(p) - \Delta T(p_{\min})$ versus p/M for fixed $Q/M = 0.1$. In both panels, $M = 1$, $r_0 = 6M$, and $r_S = r_O = 80M$, while the color gradient denotes the variation of the Lorentz-violating parameter ℓ in the interval $0 \leq \ell \leq 0.1$.

or the observer is moved farther away from the lens. In the regime of small electric and magnetic charges, the general expression derived above can be reduced to a simpler form.

Figure 5 shows the charge-induced variation of the time delay after subtracting the value computed at the smallest charge in the numerical range. This subtraction removes the common offset and isolates the dependence on the parameters of the dyonic Kalb–Ramond geometry. In the upper panel, the shifted quantity $\Delta T(Q) - \Delta T(Q_{\min})$ is plotted against Q/M for fixed $p/M = 0.1$, with $M = 1$, $r_0 = 6M$, and $r_S = r_O = 80M$. Each curve corresponds to a different value of the Lorentz-violating parameter ℓ within $0 \leq \ell \leq 0.1$. The lower panel repeats the same procedure for $\Delta T(p) - \Delta T(p_{\min})$ as a function of p/M , keeping $Q/M = 0.1$ fixed. In both panels, the shifted delay decreases as the varied charge increases, showing that both the electric and magnetic contributions reduce the travel time relative to the reference configuration.

VI. THE CORRESPONDING EFFECTIVE POTENTIALS

The dynamics of quantum fields on a curved spacetime can be reduced to an effective scattering problem in one spatial dimension. For bosonic and fermionic perturbations, described respectively by the Klein–Gordon and Dirac equations, the angular dependence is separated first. This procedure isolates the radial sector and allows the corresponding wave equation to be written in a Schrödinger–type form, with an effective potential $V_{s,v,t,\psi}$.

Here, V_s , V_v , V_t , and V_ψ denote the potentials associated with scalar, vector, tensor, and spinor perturbations, respectively. These functions control how the perturbing field propagates across the black hole geometry, fixing the reflection and transmission properties of the radial modes. They also enter directly in the calculation of quasinormal frequencies, absorption probabilities, and greybody factors. We therefore derive the explicit form of $V_{s,v,t,\psi}$ for each spin sector before analyzing the quasinormal spectra and the time–domain profiles.

Although the metric used in the present work, Eq. (6), has the simplified structure $-g_{tt} = 1/g_{rr}$, it is useful to formulate the perturbation equations in a more general static and spherically symmetric background. We therefore consider

$$ds^2 = -A(r)dt^2 + \frac{dr^2}{B(r)} + r^2 (d\theta^2 + \sin^2 \theta d\phi^2),$$

which allows the effective potentials for the different spin sectors to be obtained in a form that can later be specialized to the dyonic Kalb–Ramond geometry.

A. Bosonic sector

Bosonic perturbations with spin $s = 0, 1$, and 2 may be cast into a Schrödinger–like radial equation after the angular variables are separated. The construction is performed separately for each sector, since the scalar, vector, and tensor fields obey different covariant equations and therefore lead to distinct effective potentials. For the scalar case, $s = 0$, the starting point is the Klein–Gordon equation

$$\frac{1}{\sqrt{-g}} \partial_\mu (\sqrt{-g} g^{\mu\nu} \partial_\nu \Psi) = 0. \quad (71)$$

After a separation ansatz is imposed, the scalar field is written as a product of temporal, radial, and angular factors. This decomposition reduces the covariant Klein–Gordon equation to separate equations for each coordinate sector

$$\Psi_{\omega\ell m}(\mathbf{r}, t) = \frac{\psi_{\omega\ell}(r)}{r} Y_{\ell m}(\theta, \varphi) e^{-i\omega t}, \quad (72)$$

After introducing the tortoise coordinate r^* , the radial sector takes the form

$$dr^* = \frac{dr}{\sqrt{A(r)B(r)}}, \quad (73)$$

With this coordinate choice, the radial part of the Klein–Gordon equation is rewritten as a one-dimensional Schrödinger–like equation for the scalar radial mode,

$$\left[\frac{d^2}{dr^{*2}} + (\omega^2 - V_s) \right] \psi_{\omega\ell}(r) = 0. \quad (74)$$

For the vector sector, $s = 1$, the perturbation is described by the Proca field equation,

$$\nabla_\nu F^{\mu\nu} + m^2 A^\mu = 0, \quad (75)$$

and after the angular sector is separated and the radial components are combined into a single master variable, the vector perturbation equation can also be written in the same radial form as Eq. (74).

For tensor perturbations, $s = 2$, the linearized Einstein equations split into axial and polar sectors, described respectively by Regge–Wheeler–type and Zerilli–type equations. Each sector is governed by its own effective potential. In the present analysis, we restrict attention to the axial gravitational sector only.

In this manner, scalar, vector, and axial tensor perturbations in a static and spherically symmetric background can be described by a unified master equation, with the spin dependence encoded in the corresponding effective potential. For the general metric in Eq. (71), the scalar potential follows the form reported in Refs. [95–98]

$$V_s = A(r) \left[\frac{l(l+1)}{r^2} + \frac{1}{r\sqrt{A(r)B(r)^{-1}}} \frac{d}{dr} \sqrt{A(r)B(r)} \right] \quad (76)$$

vector, on the other hand, reads [99–101]

$$V_v = A(r) \left[\frac{l(l+1)}{r^2} \right] \quad (77)$$

and, moreover, the tensor perturbations are governed by [96, 98, 99, 102–106]

$$V_t = A(r) \left[\frac{2(B(r) - 1)}{r^2} + \frac{l(l+1)}{r^2} - \frac{1}{r\sqrt{A(r)B^{-1}(r)}} \frac{\partial}{\partial r} \left(\sqrt{A(r)B(r)} \right) \right]. \quad (78)$$

It is important to mention that the effective potentials determine how each spin sector probes the black hole background. They contain the curvature contributions that enter the radial wave equation and therefore fix the scattering behavior of the perturbing field. Through these functions, we can analyze, for instance, the wave propagation, reflection and transmission coefficients, absorption probabilities, and the quasinormal mode spectrum of the massless bosonic perturbations.

B. Fermionic sector

The fermionic sector is treated separately from the bosonic perturbations. It is represented by a spin- $\frac{1}{2}$ field whose dynamics in the curved black hole background are governed by the covariant

Dirac equation

$$\gamma^\alpha(\partial_\alpha - \omega_\alpha)\Psi = 0, \quad (79)$$

where, γ^α denote the gamma matrices adapted to the curved spacetime, and ω_α is the spin connection constructed from the tetrad frame. Once the spinor field is decomposed into its angular and radial sectors, the Dirac equation reduces to a pair of radial equations. These equations can be decoupled by introducing the functions Ψ^\pm , which satisfy wave equations of Schrödinger type and define the corresponding spinor effective potentials

$$\left[\frac{d^2}{dr^{*2}} + (\omega^2 - V_\psi^\pm) \right] \Psi^\pm = 0. \quad (80)$$

It is worth empathizing that the signs \pm distinguish the two independent spinor sectors obtained after decoupling the radial Dirac equations. The corresponding effective potentials have been obtained in Refs. [107–110] and can be written as

$$V_\psi^\pm = \frac{(l + \frac{1}{2})^2}{r^2} A(r) \pm \left(l + \frac{1}{2} \right) \sqrt{A(r)B(r)} \partial_r \left(\frac{\sqrt{A(r)}}{r} \right). \quad (81)$$

The potentials V_ψ^+ and V_ψ^- form a supersymmetric partner pair. In the subsequent analysis, we use the positive branch as the reference spinor potential and write it simply as $V_\psi \equiv V_\psi^+$

$$V_\psi = \frac{(l + \frac{1}{2})^2}{r^2} A(r) + \left(l + \frac{1}{2} \right) \sqrt{A(r)B(r)} \partial_r \left(\frac{\sqrt{A(r)}}{r} \right). \quad (82)$$

After obtaining the potentials V_s , V_v , V_t , and V_ψ , we use them as the starting point for the dynamical analysis. The next sections compute the quasinormal spectra and construct the corresponding time–domain profiles associated with these all perturbative sectors.

VII. QUASINORMAL FREQUENCIES

This section analyzes the role of the Lorentz–violating parameter ℓ , together with the electric and magnetic charges Q and p , in shaping the field perturbations supported by the black hole geometry.

A. Scalar perturbations

Using the metric of Eq. (9) in the scalar perturbation potential introduced in Eq. (76) gives

$$V_s = \left(\frac{1}{1-\ell} - \frac{2M}{r} + \frac{Q^2}{r^2(1-\ell)^2} + \frac{p^2}{r^2(1-2\ell)} \right) \left(\frac{l(l+1)}{r^2} + \frac{2M}{r^3} - \frac{2Q^2}{r^4(1-\ell)^2} - \frac{2p^2}{r^4(1-2\ell)} \right). \quad (83)$$

In the simultaneous limit $Q, p, \ell \rightarrow 0$, the scalar potential recovers the usual Schwarzschild expression, which provides a direct consistency check of the result.

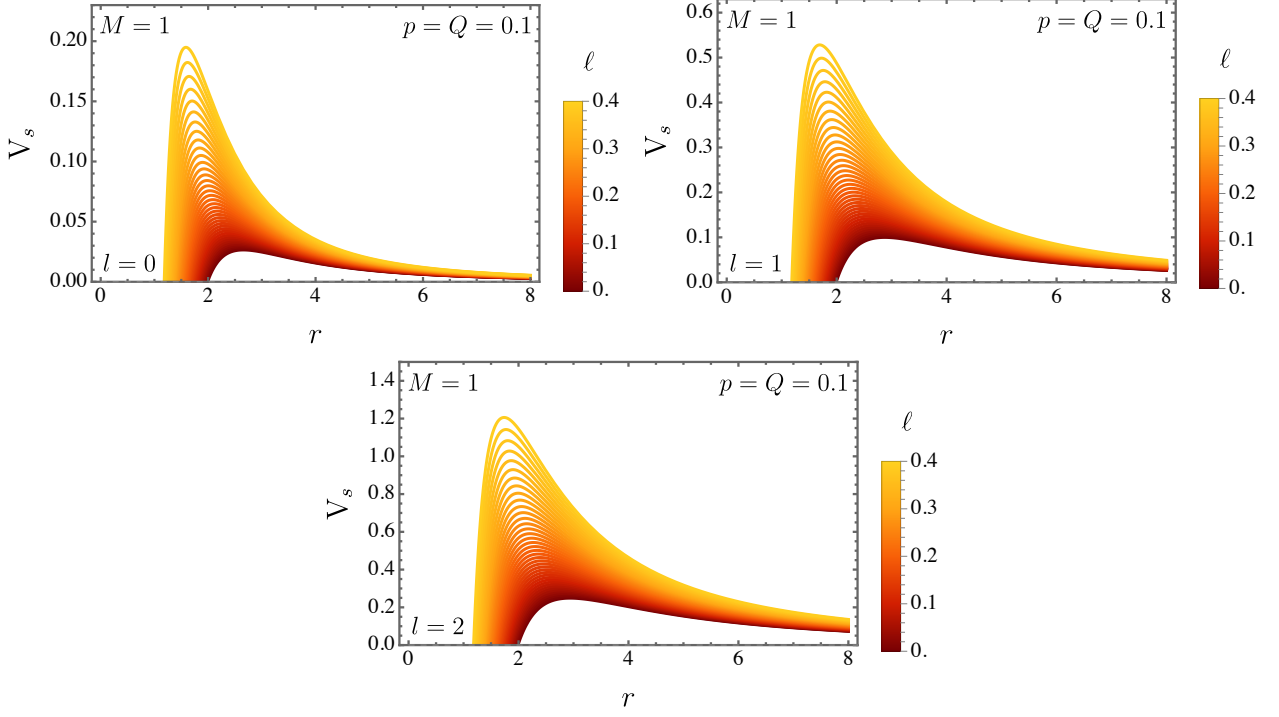


Figure 6: The scalar effective potential V_s as a function of the radial coordinate r for $M = 1$ and several values of ℓ . The panels correspond to different multipole numbers: top-left, $l = 0$; top-right, $l = 1$; and bottom, $l = 2$.

Figure 6 displays the scalar effective potential as a function of the radial coordinate r for different choices of l and ℓ . The potential barrier becomes higher as the Lorentz-violating parameter grows, showing that ℓ strengthens the radial barrier experienced by the scalar modes. A complementary description follows from rewriting V_s in terms of the tortoise coordinate r^* . Substitution of the metric in Eq. (9) into Eq. (73) gives

$$r^* = r(1 - \ell) + M(\ell - 1)^2 \ln \left[p^2(\ell - 1)^2 - (2\ell - 1)(Q^2 - r(\ell - 1)(2M(\ell - 1) + r)) \right] + \frac{\sqrt{\ell - 1}(-2M^2(2\ell - 1)(\ell - 1)^3 + p^2(\ell - 1)^2 + Q^2(1 - 2\ell)) \tan^{-1} \left(\frac{\sqrt{\ell - 1}\sqrt{2\ell - 1}(M(\ell - 1) + r)}{\sqrt{-M^2(2\ell - 1)(\ell - 1)^3 + p^2(\ell - 1)^2 + Q^2(1 - 2\ell)}} \right)}{\sqrt{2\ell - 1}\sqrt{-M^2(2\ell - 1)(\ell - 1)^3 + p^2(\ell - 1)^2 + Q^2(1 - 2\ell)}}. \quad (84)$$

Figure 7 shows V_s in terms of the tortoise coordinate r^* for several values of the multipole number l , while the remaining parameters are fixed as $M = 1$ and $\ell = p = Q = 0.1$. The resulting profile forms a smooth barrier with a single maximum, which makes the WKB scheme appropriate for extracting the corresponding quasinormal frequencies. Increasing l raises the barrier height, in agreement with the behavior commonly found for scalar perturbations in Schwarzschild, bumblebee, and Kalb–Ramond black hole geometries. For each value of l , the potential contains only one peak; therefore, no secondary (and so forth) barrier appears in this sector. This feature indicates that echo-like contributions are not expected, a point that will be checked below through

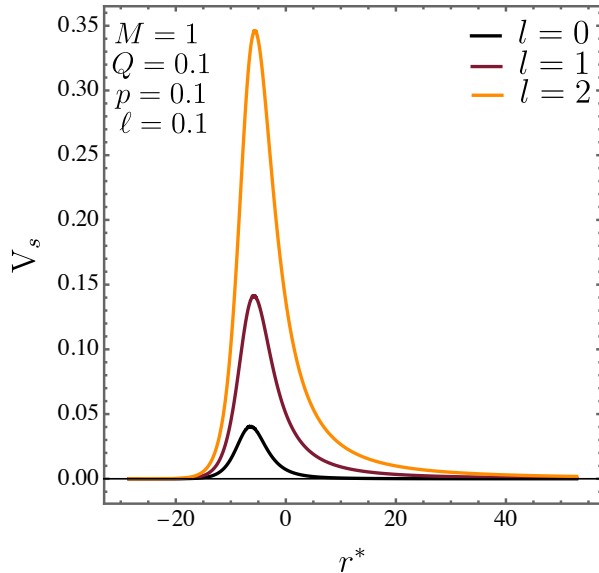


Figure 7: Scalar effective potential V_s as a function of the tortoise coordinate r^* for $M = 1$ and $\ell = p = Q = 0.1$. The curves correspond to the multipole numbers $l = 0, 1, 2$.

the time-domain evolution.

After characterizing the behavior of V_s , we proceed to the scalar quasinormal spectrum computed with the 6th-order WKB method. The numerical implementation follows the publicly available code of Ref. [75]. The frequencies obtained for $l = 0$, $l = 1$, and $l = 2$ are reported in Tables I, II, and III, respectively. In all cases, the mass is fixed at $M = 1$, while the Lorentz-violating parameter ℓ and the dyonic charges Q and p are varied.

The data in Tables I–III reveal two distinct patterns. When $\ell = 0.1$ is kept fixed and the dyonic sector is varied through $Q = p$, the scalar frequencies receive only modest corrections. For $l = 0$, the fundamental frequency is almost unchanged (at least for the values considered here); both $\text{Re}(\omega_0)$ and $|\text{Im}(\omega_0)|$ decrease slightly as the common charge value increases. The sectors with $l = 1$ and $l = 2$ behave differently: larger values of $Q = p$ increase the oscillation frequency and produce a small enhancement of the damping rate. In other words, the influence of the charge sector becomes more pronounced for higher multipoles.

The parameter ℓ produces a more significant modification of the spectrum. For fixed $Q = p = 0.1$, increasing ℓ raises both $\text{Re}(\omega_n)$ and $|\text{Im}(\omega_n)|$ in all scalar sectors analyzed here. Therefore, the Lorentz-violating contribution makes the scalar modes oscillate at higher frequencies and attenuate more quickly. Rather than reducing dissipation, this correction strengthens the decay of the ringdown signal.

For any fixed configuration, the fundamental mode ω_0 carries the largest real part and the weakest damping, so it governs the late-time signal. The overtones ω_1 and ω_2 have lower oscillation frequencies and larger imaginary magnitudes, which causes them to fade more rapidly and restricts their contribution mainly to the initial stage of the quasinormal ringing.

Table I: Scalar quasinormal spectrum for the $l = 0$ sector with $M = 1$. The frequencies ω_n are evaluated by the 6th-order WKB approximation while varying the Lorentz-violating parameter ℓ and the electric/magnetic charges Q and p .

$M, Q = p, \ell$	ω_0	ω_1	ω_2
1.0, 0.01, 0.1	0.287539 - 0.113893 <i>i</i>	0.243968 - 0.363698 <i>i</i>	0.195306 - 0.658771 <i>i</i>
1.0, 0.10, 0.1	0.287537 - 0.113891 <i>i</i>	0.243966 - 0.363694 <i>i</i>	0.195306 - 0.658772 <i>i</i>
1.0, 0.15, 0.1	0.287528 - 0.113880 <i>i</i>	0.243975 - 0.363653 <i>i</i>	0.195340 - 0.658668 <i>i</i>
1.0, 0.20, 0.1	0.287502 - 0.113852 <i>i</i>	0.243983 - 0.363561 <i>i</i>	0.195398 - 0.658495 <i>i</i>
1.0, 0.25, 0.1	0.287447 - 0.113785 <i>i</i>	0.244014 - 0.363335 <i>i</i>	0.195551 - 0.658010 <i>i</i>
1.0, 0.1, 0.10	0.287537 - 0.113891 <i>i</i>	0.243966 - 0.363694 <i>i</i>	0.195306 - 0.658772 <i>i</i>
1.0, 0.1, 0.15	0.311256 - 0.127374 <i>i</i>	0.261361 - 0.408102 <i>i</i>	0.207713 - 0.741232 <i>i</i>
1.0, 0.1, 0.20	0.338391 - 0.143401 <i>i</i>	0.280805 - 0.461163 <i>i</i>	0.221540 - 0.840070 <i>i</i>
1.0, 0.1, 0.21	0.344289 - 0.146969 <i>i</i>	0.284973 - 0.473001 <i>i</i>	0.224511 - 0.862133 <i>i</i>
1.0, 0.1, 0.22	0.350356 - 0.150671 <i>i</i>	0.289226 - 0.485320 <i>i</i>	0.227530 - 0.885159 <i>i</i>

Table II: Scalar mode quasinormal spectrum in the $l = 1$ sector for $M = 1$. The frequencies ω_n are evaluated with the 6th-order WKB scheme for several configurations of ℓ , Q , and p .

$M, Q = p, \ell$	ω_0	ω_1	ω_2
1.0, 0.01, 0.1	0.428794 - 0.116308 <i>i</i>	0.396036 - 0.360452 <i>i</i>	0.346656 - 0.633063 <i>i</i>
1.0, 0.10, 0.1	0.429855 - 0.116404 <i>i</i>	0.397185 - 0.360706 <i>i</i>	0.347944 - 0.633380 <i>i</i>
1.0, 0.15, 0.1	0.431222 - 0.116520 <i>i</i>	0.398673 - 0.361009 <i>i</i>	0.349624 - 0.633739 <i>i</i>
1.0, 0.20, 0.1	0.433194 - 0.116670 <i>i</i>	0.400831 - 0.361392 <i>i</i>	0.352078 - 0.634158 <i>i</i>
1.0, 0.25, 0.1	0.435834 - 0.116841 <i>i</i>	0.403744 - 0.361805 <i>i</i>	0.355422 - 0.634523 <i>i</i>
1.0, 0.1, 0.10	0.429855 - 0.116404 <i>i</i>	0.397185 - 0.360706 <i>i</i>	0.347944 - 0.633380 <i>i</i>
1.0, 0.1, 0.15	0.467159 - 0.130361 <i>i</i>	0.429627 - 0.404685 <i>i</i>	0.374017 - 0.712181 <i>i</i>
1.0, 0.1, 0.20	0.510236 - 0.146992 <i>i</i>	0.466772 - 0.457233 <i>i</i>	0.403602 - 0.806588 <i>i</i>
1.0, 0.1, 0.21	0.519658 - 0.150700 <i>i</i>	0.474853 - 0.468966 <i>i</i>	0.410006 - 0.827696 <i>i</i>
1.0, 0.1, 0.22	0.529376 - 0.154550 <i>i</i>	0.483171 - 0.481159 <i>i</i>	0.416580 - 0.849657 <i>i</i>

Table III: Scalar quasinormal spectrum for the $l = 2$ multipole with $M = 1$. The values of ω_n are obtained from the 6th-order WKB approximation for different choices of the Lorentz-violating parameter ℓ and the dyonic charges Q and p .

$M, Q = p, \ell$	ω_0	ω_1	ω_2
1.0, 0.01, 0.1	0.621985 - 0.117548 <i>i</i>	0.598108 - 0.358525 <i>i</i>	0.556536 - 0.615621 <i>i</i>
1.0, 0.10, 0.1	0.624209 - 0.117687 <i>i</i>	0.600428 - 0.358916 <i>i</i>	0.559025 - 0.616190 <i>i</i>
1.0, 0.15, 0.1	0.627082 - 0.117857 <i>i</i>	0.603428 - 0.359394 <i>i</i>	0.562251 - 0.616876 <i>i</i>
1.0, 0.20, 0.1	0.631231 - 0.118086 <i>i</i>	0.607769 - 0.360030 <i>i</i>	0.566932 - 0.617771 <i>i</i>
1.0, 0.25, 0.1	0.636799 - 0.118359 <i>i</i>	0.613611 - 0.360779 <i>i</i>	0.573254 - 0.618785 <i>i</i>
1.0, 0.1, 0.10	0.624209 - 0.117687 <i>i</i>	0.600428 - 0.358916 <i>i</i>	0.559025 - 0.616190 <i>i</i>
1.0, 0.1, 0.15	0.679585 - 0.131888 <i>i</i>	0.652222 - 0.402603 <i>i</i>	0.604985 - 0.692206 <i>i</i>
1.0, 0.1, 0.20	0.743775 - 0.148832 <i>i</i>	0.712033 - 0.454797 <i>i</i>	0.657757 - 0.783203 <i>i</i>
1.0, 0.1, 0.21	0.757849 - 0.152612 <i>i</i>	0.725116 - 0.466452 <i>i</i>	0.66926 - 0.803548 <i>i</i>
1.0, 0.1, 0.22	0.772381 - 0.156539 <i>i</i>	0.738614 - 0.478562 <i>i</i>	0.681115 - 0.824692 <i>i</i>

B. Vector perturbations

We now apply the same procedure to the vector sector. Inserting the metric of Eq. (9) into the general vector potential in Eq. (77) yields the following effective potential:

$$V_v = \left(\frac{1}{1-\ell} - \frac{2M}{r} + \frac{Q^2}{r^2(1-\ell)^2} + \frac{p^2}{r^2(1-2\ell)} \right) \left(\frac{l(l+1)}{r^2} \right). \quad (85)$$

As it is straightforward to be verified, in the Schwarzschild limit, obtained by taking $\ell, Q, p \rightarrow 0$, this expression recovers the usual effective potential for vector perturbations.

Figure 8 presents the vector effective potential V_v as a function of the radial coordinate r for several choices of l, ℓ, Q , and p . The plots show that larger values of the Lorentz-violating parameter raise the height of the potential barrier. As in the scalar sector, the parameter ℓ strengthens the radial barrier governing the propagation of the vector modes.

To complete this description, V_v is also written in terms of the tortoise coordinate r^* , following the same construction used above. Figure 9 displays the corresponding profiles for $M = 1$ and $\ell = Q = p = 0.1$, considering the multipole numbers $l = 0, 1, 2$. The right panel extends the range of r^* and makes the single-barrier structure clear for each multipole. Since no secondary maximum appears, the vector sector does not indicate the presence of echo-like contributions.

The vector quasinormal frequencies obtained from the 6th-order WKB approximation are collected in Tables IV–VI. These tables correspond, respectively, to the multipole sectors $l = 1, l = 2$,

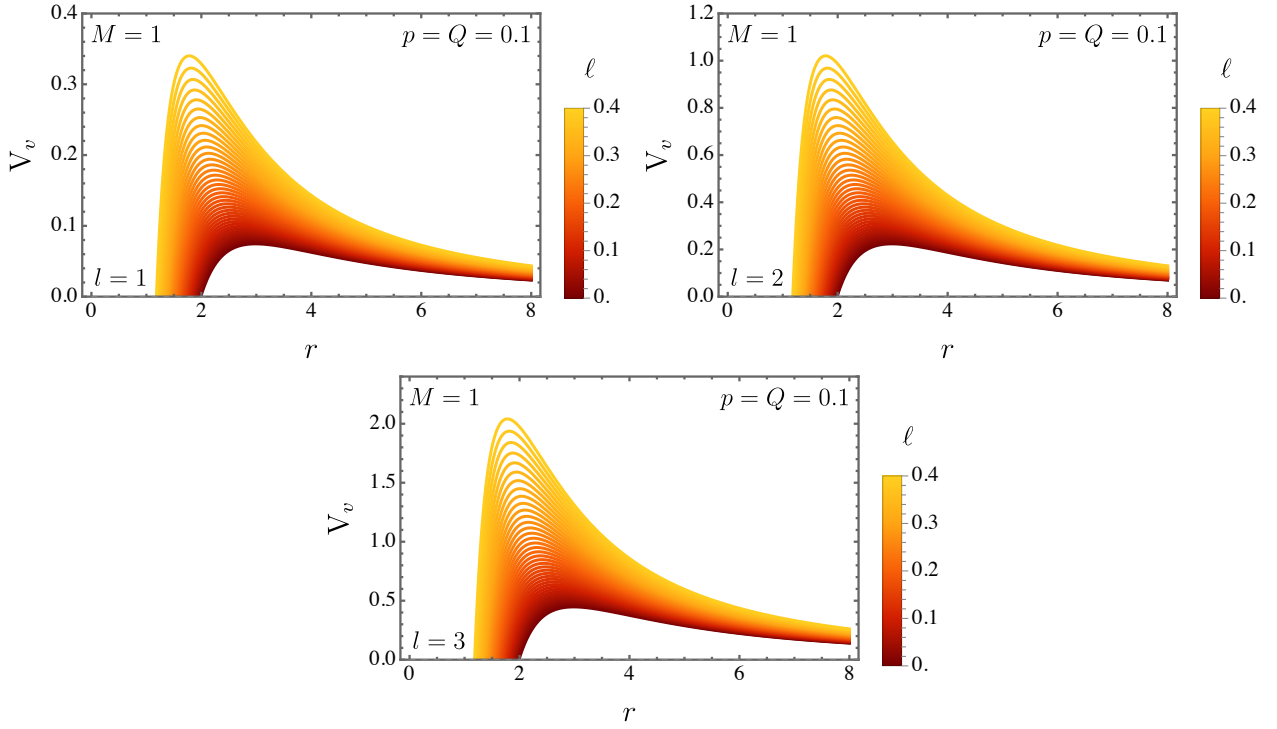


Figure 8: Vector effective potential V_v as a function of the radial coordinate r for $M = 1$ and several values of ℓ . The panels correspond to the multipole sectors $l = 1$ top-left, $l = 2$ top-right, and $l = 3$ bottom.

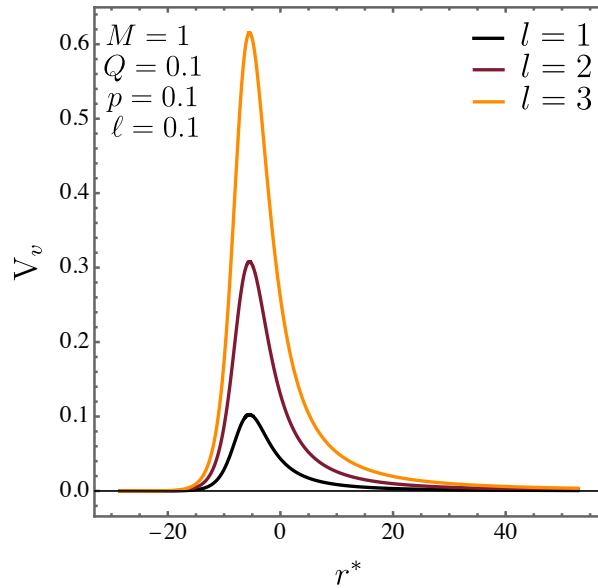


Figure 9: Vector effective potential V_v expressed in terms of the tortoise coordinate r^* for $M = 1$ and $\ell = Q = p = 0.1$, considering the multipole sectors $l = 1, 2, 3$.

and $l = 3$, with the mass normalized to $M = 1$. The remaining parameters are varied so that the separate effects of the dyonic charges and of the Lorentz-violating contribution can be compared.

A first pattern emerges when the Lorentz-violating parameter is fixed at $\ell = 0.1$ and the electric and magnetic charges are increased together, $Q = p$. Under this variation, the vector spectrum

changes only moderately. The real part of ω_n grows with the charge value for all multipoles considered, showing that the oscillatory component becomes slightly faster. The imaginary sector follows the same tendency in magnitude, but the change is weaker; then, the damping rate receives only a small enhancement. This charge-induced shift becomes more apparent for larger l , with the $l = 3$ modes reaching the highest real frequencies among the vector cases listed.

The dependence on ℓ is considerably more pronounced. When the charges are held fixed at $Q = p = 0.1$, larger values of ℓ increase both $\text{Re}(\omega_n)$ and $|\text{Im}(\omega_n)|$ throughout the vector spectrum. Therefore, the Lorentz-violating parameter does not delay the decay of the perturbation. Instead, it drives the ringdown toward higher oscillation frequencies and faster attenuation. This behavior matches the potential profiles discussed above, where increasing ℓ raises and narrows the effective barrier.

The ordering with respect to the multipole number also follows the expected structure. For fixed M , Q , p , and ℓ , the real part of the frequency rises as one goes from $l = 1$ to $l = 3$. Thus, higher vector multipoles oscillate more rapidly. The damping of the fundamental mode varies less dramatically with l , so the main multipolar effect appears in the oscillation frequency rather than in the decay rate. Within each multipole sector, ω_0 remains the least damped mode and therefore controls the late-time signal, while ω_1 and ω_2 decay more quickly and affect mostly the early ringdown stage.

A comparison with the scalar results shows that, for the same parameter choices and the same multipole number, the vector modes generally oscillate at lower frequencies. Their damping rates are also slightly smaller for the lowest modes. Even so, the qualitative response to the parameters is the same in both sectors: the dyonic charges produce relatively mild corrections, whereas the Lorentz-violating parameter ℓ gives the dominant enhancement of the oscillation frequency and of the damping rate.

C. Tensor perturbations

We close the bosonic part of the analysis with the tensor, or axial, perturbative sector. Following the same construction adopted for the scalar and vector fields, the metric in Eq. (9) is inserted into the general expression of Eq. (78). This substitution leads to the tensor effective potential written as follows:

$$V_t = \left(\frac{1}{1-\ell} - \frac{2M}{r} + \frac{p^2}{r^2(1-2\ell)} + \frac{Q^2}{r^2(1-\ell)^2} \right) \times \left(\frac{l(l+1)}{r^2} - \frac{6M\ell^2 - 12M\ell + 6M}{r^3(\ell-1)^2} + \frac{4p^2}{r^4(1-2\ell)} + \frac{4Q^2}{r^4(\ell-1)^2} + \frac{2\ell - 2\ell^2}{r^2(\ell-1)^2} \right). \quad (86)$$

In the simultaneous limit $Q, p, \ell \rightarrow 0$, the tensor effective potential reduces to the standard Schwarzschild expression for the corresponding perturbative sector.

Table IV: Vector quasinormal spectrum in the $l = 1$ sector for $M = 1$. The frequencies ω_n are obtained with the 6th-order WKB approximation for several choices of ℓ , Q , and p .

$M, Q = p, \ell$	ω_0	ω_1	ω_2
1.0, 0.01, 0.1	0.287554 - 0.113896i	0.243983 - 0.363707i	0.195321 - 0.658795i
1.0, 0.10, 0.1	0.289090 - 0.114114i	0.245756 - 0.364238i	0.197417 - 0.659249i
1.0, 0.15, 0.1	0.291080 - 0.114387i	0.248064 - 0.364883i	0.200158 - 0.659730i
1.0, 0.20, 0.1	0.293960 - 0.114764i	0.251404 - 0.365777i	0.204115 - 0.660433i
1.0, 0.25, 0.1	0.297842 - 0.115235i	0.255933 - 0.366853i	0.209495 - 0.661144i
1.0, 0.1, 0.10	0.289090 - 0.114114i	0.245756 - 0.364238i	0.197417 - 0.659249i
1.0, 0.1, 0.15	0.313295 - 0.127679i	0.263725 - 0.408841i	0.210513 - 0.741849i
1.0, 0.1, 0.20	0.341132 - 0.143831i	0.284006 - 0.462193i	0.225347 - 0.840880i
1.0, 0.1, 0.21	0.347206 - 0.147430i	0.288380 - 0.474113i	0.228563 - 0.863028i
1.0, 0.1, 0.22	0.353466 - 0.151168i	0.292869 - 0.486506i	0.231869 - 0.886073i

Table V: Vector quasinormal spectrum for the $l = 2$ multipole with $M = 1$. The values of ω_n are extracted through the 6th-order WKB approximation for different configurations of ℓ , Q , and p .

$M, Q = p, \ell$	ω_0	ω_1	ω_2
1.0, 0.01, 0.1	0.534168 - 0.117134i	0.506875 - 0.359192i	0.461578 - 0.621867i
1.0, 0.10, 0.1	0.536748 - 0.117322i	0.509599 - 0.359713i	0.464548 - 0.62259i
1.0, 0.15, 0.1	0.540082 - 0.117556i	0.513125 - 0.360356i	0.468401 - 0.623472i
1.0, 0.20, 0.1	0.544903 - 0.117875i	0.518231 - 0.361227i	0.473989 - 0.624642i
1.0, 0.25, 0.1	0.551385 - 0.118267i	0.525109 - 0.362283i	0.481536 - 0.626013i
1.0, 0.1, 0.10	0.536748 - 0.117322i	0.509599 - 0.359713i	0.464548 - 0.622592i
1.0, 0.1, 0.15	0.584220 - 0.131464i	0.553009 - 0.403564i	0.501804 - 0.699711i
1.0, 0.1, 0.20	0.639257 - 0.148337i	0.603089 - 0.455974i	0.544502 - 0.792089i
1.0, 0.1, 0.21	0.651327 - 0.152101i	0.614040 - 0.467679i	0.553806 - 0.812744i
1.0, 0.1, 0.22	0.663792 - 0.156011i	0.625334 - 0.479844i	0.563385 - 0.834226i

Figure 10 presents the tensor effective potential V_t for different choices of l and ℓ . The barrier becomes higher as the Lorentz-violating parameter increases, showing that ℓ strengthens the radial confinement of the tensor modes, in agreement with the behavior observed in the scalar and vector

Table VI: Vector quasinormal spectrum in the $l = 3$ sector for the normalized mass $M = 1$. The frequencies ω_n are computed through the 6th-order WKB approximation while varying ℓ , Q , and p .

$M, Q = p, \ell$	ω_0	ω_1	ω_2
1.0, 0.01, 0.1	0.768134 - 0.117960 <i>i</i>	0.748443 - 0.357838 <i>i</i>	0.712487 - 0.608899 <i>i</i>
1.0, 0.10, 0.1	0.771754 - 0.118148 <i>i</i>	0.752168 - 0.358366 <i>i</i>	0.716404 - 0.609704 <i>i</i>
1.0, 0.15, 0.1	0.776431 - 0.118375 <i>i</i>	0.756983 - 0.359019 <i>i</i>	0.721475 - 0.610695 <i>i</i>
1.0, 0.20, 0.1	0.783192 - 0.118685 <i>i</i>	0.763948 - 0.359904 <i>i</i>	0.728818 - 0.612026 <i>i</i>
1.0, 0.25, 0.1	0.792275 - 0.119064 <i>i</i>	0.773317 - 0.360983 <i>i</i>	0.738712 - 0.613620 <i>i</i>
1.0, 0.1, 0.10	0.771754 - 0.118148 <i>i</i>	0.752168 - 0.358366 <i>i</i>	0.716404 - 0.609704 <i>i</i>
1.0, 0.1, 0.15	0.840831 - 0.132442 <i>i</i>	0.818287 - 0.401975 <i>i</i>	0.777353 - 0.684631 <i>i</i>
1.0, 0.1, 0.20	0.921047 - 0.149507 <i>i</i>	0.894887 - 0.454083 <i>i</i>	0.847685 - 0.774291 <i>i</i>
1.0, 0.1, 0.21	0.938658 - 0.153316 <i>i</i>	0.911680 - 0.465720 <i>i</i>	0.863067 - 0.794332 <i>i</i>
1.0, 0.1, 0.22	0.956850 - 0.157272 <i>i</i>	0.929017 - 0.477811 <i>i</i>	0.878936 - 0.815163 <i>i</i>

sectors. Figure 11 shows the same potential written in terms of the tortoise coordinate r^* . For each multipole number, the profile contains only one maximum, so no secondary barrier appears in this sector. The resulting smooth barrier structure also supports the use of the WKB approximation in the calculation of the tensor quasinormal frequencies.

The tensor spectra reported in Tables VII, VIII, and IX correspond to the multipoles $l = 2$, $l = 3$, and $l = 4$, respectively. These results make it possible to distinguish two sources of modification in the axial sector: the dyonic charges and the Lorentz-violating parameter.

For the configurations in which $\ell = 0.1$ remains fixed and the charges are varied according to $Q = p$, the changes in the spectrum are relatively small. As the common charge value increases, the real part of ω_n becomes larger, while the magnitude of the imaginary part also grows. Thus, the dyonic sector shifts the tensor modes toward slightly higher oscillation frequencies and produces a modest increase in the damping rate. This behavior occurs for all multipoles and overtones listed in the tables.

The role of ℓ is considerably more pronounced. When the charges are kept fixed at $Q = p = 0.1$, increasing the Lorentz-violating parameter produces a clear upward shift in both $\text{Re}(\omega_n)$ and $|\text{Im}(\omega_n)|$. Hence, the axial perturbations do not become longer lived as ℓ grows. Instead, the ringdown becomes faster in two senses: the oscillation frequency increases, and the decay time decreases. Notice again that this trend agrees with the potential analysis, since larger values of ℓ raise the height of the effective barrier and make its profile steeper.

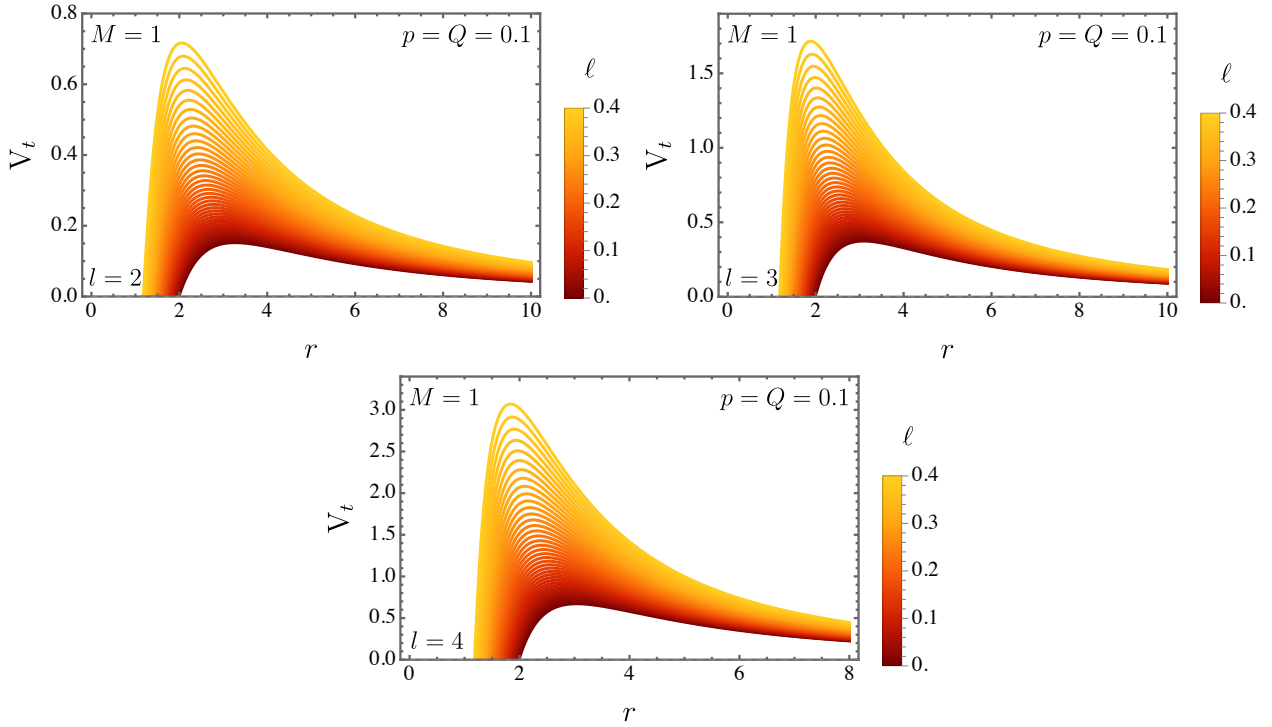


Figure 10: Tensor effective potential V_t as a function of the radial coordinate r for $M = 1$ and several choices of the Lorentz-violating parameter ℓ . The panels represent the multipole sectors $l = 2$ top-left, $l = 3$ top-right, and $l = 4$ bottom.

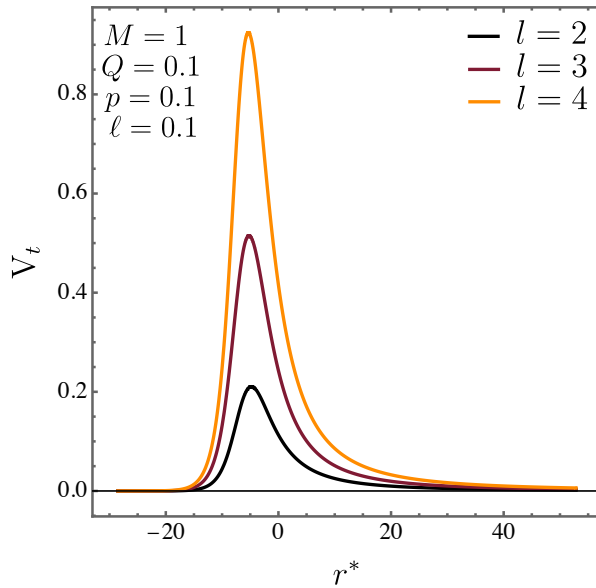


Figure 11: Tensor effective potential V_t written in terms of the tortoise coordinate r^* for $M = 1$ and fixed parameters $\ell = p = Q = 0.1$. The curves correspond to the multipole sectors $l = 2, 3, 4$.

The multipole dependence follows the usual ordering of black hole perturbations. At fixed M , Q , p , and ℓ , the real part of the frequency increases from $l = 2$ to $l = 4$, meaning that higher tensor multipoles oscillate more rapidly. The damping rate also changes with l , but less strongly than the oscillation frequency. Within each multipole sector, the fundamental mode ω_0 is the least damped

one and therefore controls the late-time response. By contrast, the overtones ω_1 and ω_2 have larger imaginary magnitudes, so they disappear more quickly and affect mainly the first part of the ringing signal.

When compared with the scalar and vector cases, the tensor sector generally yields smaller real frequencies for the same parameter choices and the same multipole number. The corresponding low-lying tensor modes also tend to have slightly weaker damping. Nevertheless, the overall parameter dependence remains the same across the three sectors: the charges Q and p generate mild shifts in the spectrum, whereas the Lorentz-violating parameter ℓ gives the dominant increase in both the oscillation frequency and the damping rate.

Table VII: Tensor quasinormal spectrum in the $l = 2$ sector for $M = 1$. The frequencies ω_n are obtained with the 6th-order WKB approximation for different choices of the ℓ .

$M, Q = p, \ell$	ω_0	ω_1	ω_2
1.0, 0.01, 0.1	0.436727 - 0.109106 <i>i</i>	0.400538 - 0.336570 <i>i</i>	0.337497 - 0.590785 <i>i</i>
1.0, 0.10, 0.1	0.438840 - 0.109279 <i>i</i>	0.402905 - 0.337028 <i>i</i>	0.340353 - 0.591289 <i>i</i>
1.0, 0.15, 0.1	0.441571 - 0.109495 <i>i</i>	0.405969 - 0.337594 <i>i</i>	0.344060 - 0.591898 <i>i</i>
1.0, 0.20, 0.1	0.445517 - 0.109790 <i>i</i>	0.410405 - 0.338367 <i>i</i>	0.349444 - 0.592705 <i>i</i>
1.0, 0.25, 0.1	0.450820 - 0.110155 <i>i</i>	0.416378 - 0.339314 <i>i</i>	0.356721 - 0.593652 <i>i</i>
1.0, 0.1, 0.10	0.438840 - 0.109279 <i>i</i>	0.402905 - 0.337028 <i>i</i>	0.340353 - 0.591289 <i>i</i>
1.0, 0.1, 0.15	0.478050 - 0.122177 <i>i</i>	0.436142 - 0.377451 <i>i</i>	0.363403 - 0.664381 <i>i</i>
1.0, 0.1, 0.20	0.523583 - 0.137560 <i>i</i>	0.474157 - 0.425899 <i>i</i>	0.388742 - 0.752699 <i>i</i>
1.0, 0.1, 0.21	0.533578 - 0.140993 <i>i</i>	0.482419 - 0.436750 <i>i</i>	0.394107 - 0.772594 <i>i</i>
1.0, 0.1, 0.22	0.543904 - 0.144560 <i>i</i>	0.490925 - 0.448037 <i>i</i>	0.399587 - 0.793319 <i>i</i>

D. Spinor perturbations

After treating the bosonic perturbations, we now extend the discussion to the fermionic sector. The spinor modes are governed by the following effective potential:

$$V_\psi = \frac{\left(l + \frac{1}{2}\right) \left(\frac{-2Mr + \frac{p^2}{1-2\ell} + \frac{Q^2}{(\ell-1)^2}}{r^2} + \frac{1}{1-\ell} \right) \left(2l - 2\sqrt{\frac{-2Mr + \frac{p^2}{1-2\ell} + \frac{Q^2}{(\ell-1)^2}}{r^2} + \frac{1}{1-\ell}} + \frac{2 \left(Mr + \frac{p^2}{2\ell-1} - \frac{Q^2}{(\ell-1)^2} \right)}{r^2 \sqrt{\frac{-2Mr + \frac{p^2}{1-2\ell} + \frac{Q^2}{(\ell-1)^2}}{r^2} + \frac{1}{1-\ell}}} + 1 \right)}{2r^2}. \quad (87)$$

In the Schwarzschild limit, obtained by setting $\ell = p = Q = 0$, the spinor potential reduces to the standard Dirac potential, which shows a direct check of the expression. The behavior of V_ψ is

Table VIII: Tensor quasinormal spectrum for the $l = 3$ multipole with $M = 1$. The values of ω_n are extracted through the 6th-order WKB approximation for several choices of ℓ .

$M, Q = p, \ell$	ω_0	ω_1	ω_2
1.0, 0.01, 0.1	0.701136 - 0.114000 <i>i</i>	0.679274 - 0.346410 <i>i</i>	0.639158 - 0.591190 <i>i</i>
1.0, 0.10, 0.1	0.704435 - 0.114214 <i>i</i>	0.682687 - 0.346942 <i>i</i>	0.642787 - 0.592004 <i>i</i>
1.0, 0.15, 0.1	0.708699 - 0.114443 <i>i</i>	0.687101 - 0.347602 <i>i</i>	0.647487 - 0.593006 <i>i</i>
1.0, 0.20, 0.1	0.714861 - 0.114756 <i>i</i>	0.693486 - 0.348499 <i>i</i>	0.654296 - 0.594358 <i>i</i>
1.0, 0.25, 0.1	0.72314 - 0.115141 <i>i</i>	0.702077 - 0.349597 <i>i</i>	0.663475 - 0.595987 <i>i</i>
1.0, 0.1, 0.10	0.704435 - 0.114214 <i>i</i>	0.682687 - 0.346942 <i>i</i>	0.642787 - 0.592004 <i>i</i>
1.0, 0.1, 0.15	0.767624 - 0.127817 <i>i</i>	0.742562 - 0.388519 <i>i</i>	0.696765 - 0.663725 <i>i</i>
1.0, 0.1, 0.20	0.841045 - 0.144018 <i>i</i>	0.811921 - 0.438082 <i>i</i>	0.758933 - 0.749355 <i>i</i>
1.0, 0.1, 0.21	0.857170 - 0.147629 <i>i</i>	0.827125 - 0.449134 <i>i</i>	0.772510 - 0.768471 <i>i</i>
1.0, 0.1, 0.22	0.873829 - 0.151378 <i>i</i>	0.842823 - 0.460612 <i>i</i>	0.786513 - 0.788327 <i>i</i>

Table IX: Tensor quasinormal spectrum associated with the $l = 4$ multipole for $M = 1$. The tabulated frequencies ω_n are obtained from the 6th-order WKB scheme for several values of ℓ .

$M, Q = p, \ell$	ω_0	ω_1	ω_2
1.0, 0.01, 0.1	0.946906 - 0.115991 <i>i</i>	0.930585 - 0.350480 <i>i</i>	0.899598 - 0.592320 <i>i</i>
1.0, 0.10, 0.1	0.951324 - 0.116174 <i>i</i>	0.935087 - 0.351022 <i>i</i>	0.904262 - 0.593170 <i>i</i>
1.0, 0.15, 0.1	0.957031 - 0.116402 <i>i</i>	0.940906 - 0.351688 <i>i</i>	0.910296 - 0.594221 <i>i</i>
1.0, 0.20, 0.1	0.965279 - 0.116712 <i>i</i>	0.949319 - 0.352594 <i>i</i>	0.919027 - 0.595644 <i>i</i>
1.0, 0.25, 0.1	0.976357 - 0.117094 <i>i</i>	0.960628 - 0.353704 <i>i</i>	0.930782 - 0.597370 <i>i</i>
1.0, 0.1, 0.10	0.951324 - 0.116174 <i>i</i>	0.935087 - 0.351022 <i>i</i>	0.904262 - 0.593170 <i>i</i>
1.0, 0.1, 0.15	1.036920 - 0.130113 <i>i</i>	1.018220 - 0.393294 <i>i</i>	0.982801 - 0.665091 <i>i</i>
1.0, 0.1, 0.20	1.136410 - 0.146732 <i>i</i>	1.114680 - 0.443720 <i>i</i>	1.073660 - 0.750972 <i>i</i>
1.0, 0.1, 0.21	1.158260 - 0.150438 <i>i</i>	1.135840 - 0.454970 <i>i</i>	1.093560 - 0.770144 <i>i</i>
1.0, 0.1, 0.22	1.180840 - 0.154287 <i>i</i>	1.157710 - 0.466655 <i>i</i>	1.114100 - 0.790062 <i>i</i>

displayed in Fig. 12 for different choices of the angular parameter l and of the Lorentz-violating parameter ℓ . The curves show that increasing ℓ lifts the potential barrier. The Lorentz-violating contribution makes the exterior barrier more pronounced for spinor perturbations, in the same

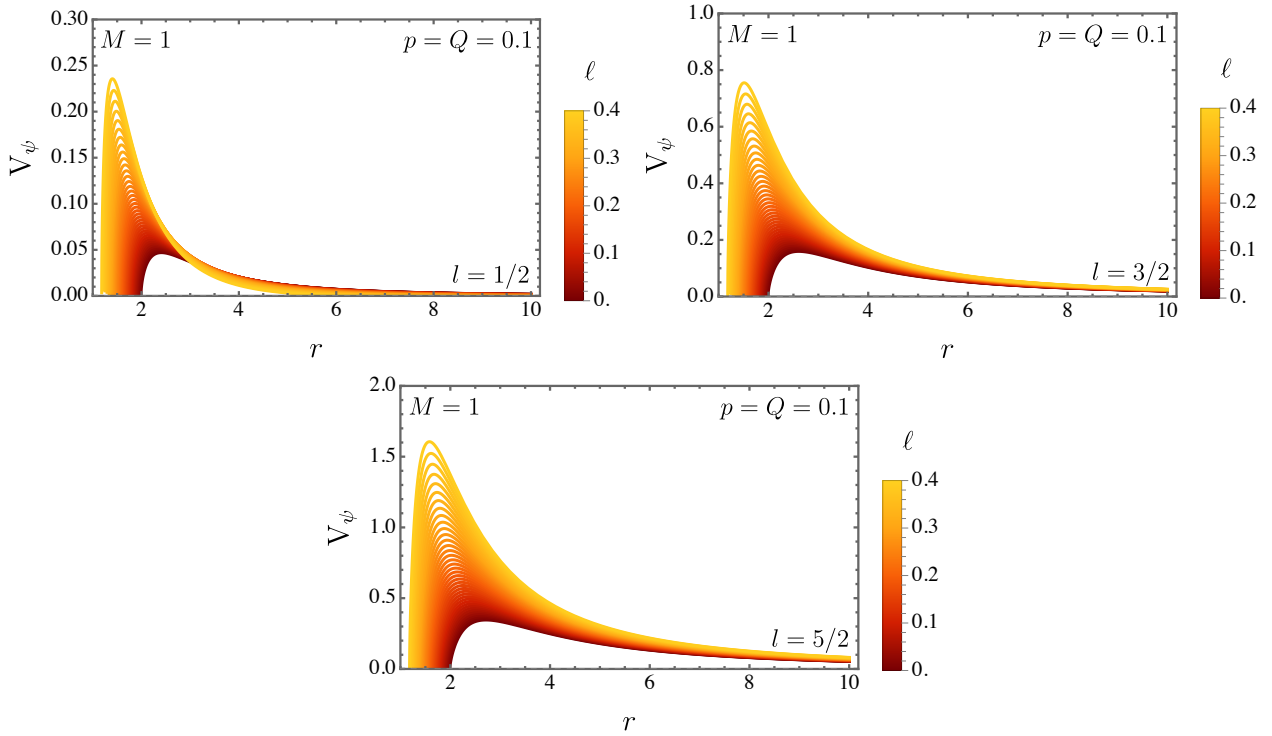


Figure 12: Spinor effective potential V_ψ as a function of the radial coordinate r for $M = 1$ and several values of the Lorentz-violating parameter ℓ . The panels correspond to $l = 1/2$ top-left, $l = 3/2$ top-right, and $l = 5/2$ bottom.

qualitative manner observed for the scalar, vector, and tensor sectors.

The representation in terms of the tortoise coordinate is shown in Fig. 13, where V_ψ is plotted as a function of r^* for $M = 1$ and $\ell = 0.1$. Each value of l leads to a single-barrier profile, with no additional maximum outside the event horizon. A direct comparison with the bosonic potentials is given in Fig. 14, where V_s , V_v , V_t , and V_ψ are plotted in the same r^* coordinate. For the parameter set considered, the barriers satisfy the ordering $V_\psi > V_s > V_v > V_t$. Since, in the WKB approximation, the peak of the potential gives the leading contribution to the oscillatory part of the quasinormal spectrum, this hierarchy suggests larger real frequencies for the sectors with higher barriers. This relation will be contrasted with the time-domain profiles in the following analysis.

The spinor potential vanishes at the horizon and also tends to zero at spatial infinity. Between these two asymptotic regions, it forms only one exterior barrier. Consequently, the potential does not create a cavity capable of repeatedly reflecting the perturbation. Under the usual black-hole boundary conditions, this structure does not favor echo-like signals in the spinor sector.

Tables X–XII report the spinor quasinormal frequencies associated with the three angular modes $l = 1/2$, $l = 3/2$, and $l = 5/2$, obtained from the 6th-order WKB approximation. A direct comparison among the entries shows that the Lorentz-violating parameter ℓ produces the clearest change in the spectrum. When the charges are fixed at $Q = p = 0.1$, increasing ℓ shifts the modes to larger values of $\text{Re}(\omega_n)$ and also increases the magnitude of $\text{Im}(\omega_n)$. Hence, the spinor field does not

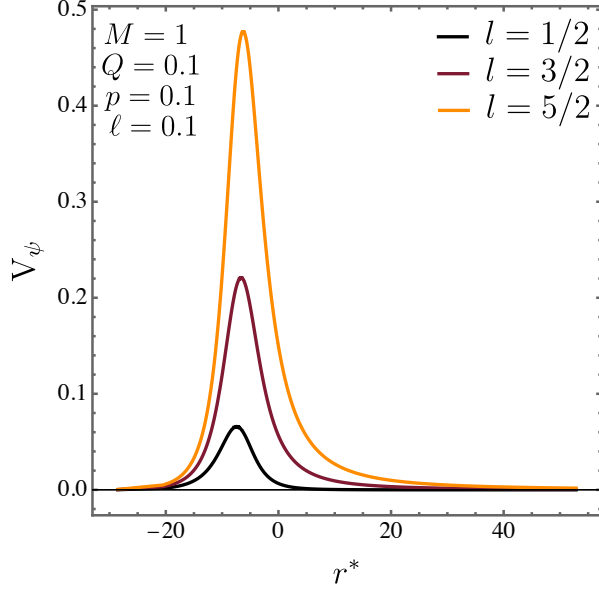


Figure 13: Spinor effective potential V_ψ expressed in terms of the tortoise coordinate r^* for $M = 1$ and $\ell = 0.1$, considering the multipole sectors $l = 1/2$, $l = 3/2$, and $l = 5/2$. The right panel covers a broader interval of r^* , making the single-peak structure explicit for each value of l .

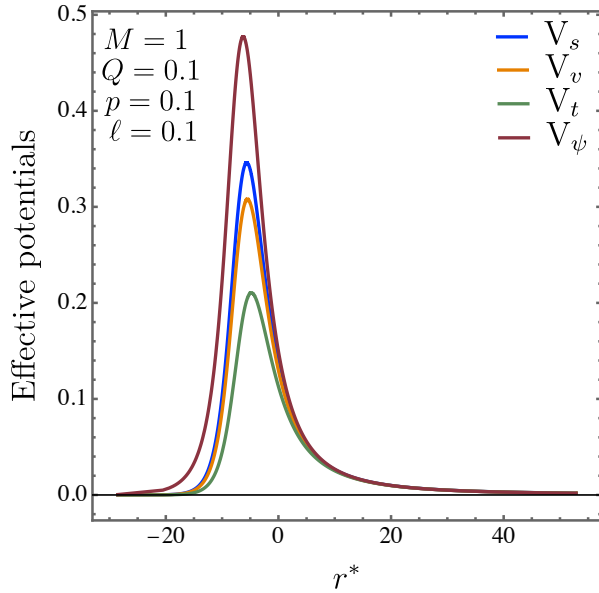


Figure 14: Effective potentials for the different perturbative sectors as functions of the tortoise coordinate r^* . The comparison uses $l = 5/2$ for the spinor field and $l = 2$ for the scalar, vector, and tensor fields, yielding the hierarchy $V_\psi > V_s > V_v > V_t$.

display a slower oscillatory response for stronger Lorentz violation. Instead, the ringdown becomes both faster in frequency and shorter lived in time.

The charge dependence appears in a more restricted form. For the set of rows in which $\ell = 0.1$ is kept fixed and $Q = p$ is varied, the fundamental frequency usually moves toward larger real values. In the $l = 3/2$ and $l = 5/2$ cases, the imaginary part of the fundamental mode also becomes slightly

more negative as the dyonic charge increases. This effect is not equally clear for all overtones. Some higher modes change only weakly, while others depart from a simple monotonic pattern, mainly in the $l = 1/2$ sector. The charge parameters therefore perturb the spectrum, but they do not drive its main behavior.

The comparison among different spinor multipoles gives another relevant feature of the data. At fixed M , $Q = p$, and ℓ , the real part of the fundamental mode grows as the angular number is increased. Thus, modes with larger l oscillate at higher frequencies. The imaginary part, however, does not follow an equally direct hierarchy. The $l = 1/2$ fundamental mode is strongly damped when compared with its oscillation frequency, which makes this sector more delicate from the numerical point of view. This is particularly important because WKB calculations are known to be less robust for low multipoles and higher overtone numbers.

The behavior of the overtones must therefore be interpreted with some caution. In the usual ringdown picture, the least damped mode gives the dominant late-time contribution, while the overtones decay faster and are mainly associated with the initial stage of the signal. However, the table for $l = 1/2$ contains an anomalously large real part for the second overtone, well above the corresponding values for the fundamental mode and the first overtone. This feature should be rechecked, since precisely this combination—low l and large n —is among the least favorable regimes for the WKB approximation.

Taken together, the spinor results reinforce the same physical tendency obtained for the scalar, vector, and tensor perturbations. The parameter ℓ increases the height and sharpness of the effective barrier, which is reflected in larger oscillation frequencies and stronger damping rates. The dyonic sector introduces smaller corrections, whereas the Lorentz-violating contribution remains the main source of spectral modification.

VIII. TIME-DOMAIN SOLUTION

To study the time evolution of scalar, vector, and tensor perturbations, we must go beyond a purely spectral description. A frequency-domain treatment identifies the quasinormal spectrum, but it does not by itself display how the perturbing field propagates, decays, and scatters during the evolution. The time-domain approach therefore provides the appropriate setting for tracking the waveform directly and for determining how the quasinormal ringing emerges from the initial disturbance. Because the effective potentials associated with these perturbations generally possess a nontrivial radial profile, the evolution requires a stable and accurate numerical scheme. We therefore employ the characteristic integration method introduced by Gundlach et al. [111].

Following the numerical strategies used in Refs. [40, 111–118], we rewrite the perturbation equation in the double-null variables $u = t - r^*$ and $v = t + r^*$. This choice places the evolution problem

Table X: Spinor field quasinormal spectrum for the mode $l = 1/2$ with $M = 1$. The frequencies ω_n are evaluated using the 6th-order WKB approximation for several choices of the Lorentz-violating parameter ℓ .

$M, Q = p, \ell$	ω_0	ω_1	ω_2
1.0, 0.01, 0.1	0.0443462 - 0.239504 <i>i</i>	0.124330 - 0.470598 <i>i</i>	1.317530 - 0.373190 <i>i</i>
1.0, 0.10, 0.1	0.0447141 - 0.239005 <i>i</i>	0.124178 - 0.471756 <i>i</i>	1.309470 - 0.373765 <i>i</i>
1.0, 0.15, 0.1	0.0454212 - 0.237110 <i>i</i>	0.125783 - 0.466390 <i>i</i>	1.313310 - 0.370378 <i>i</i>
1.0, 0.20, 0.1	0.0459516 - 0.236848 <i>i</i>	0.123786 - 0.474493 <i>i</i>	1.281640 - 0.375879 <i>i</i>
1.0, 0.25, 0.1	0.0470002 - 0.234629 <i>i</i>	0.124166 - 0.473432 <i>i</i>	1.267380 - 0.374857 <i>i</i>
1.0, 0.1, 0.10	0.0447141 - 0.239005 <i>i</i>	0.124178 - 0.471756 <i>i</i>	1.309470 - 0.373765 <i>i</i>
1.0, 0.1, 0.15	0.0498984 - 0.271985 <i>i</i>	0.139680 - 0.530286 <i>i</i>	1.420450 - 0.408968 <i>i</i>
1.0, 0.1, 0.20	0.0566830 - 0.310413 <i>i</i>	0.159182 - 0.593130 <i>i</i>	1.535960 - 0.445282 <i>i</i>

Table XI: Spinor quasinormal spectrum associated with the angular mode $l = 3/2$ for $M = 1$. The frequencies ω_n are obtained from the 6th-order WKB approximation by varying the Lorentz-violating parameter ℓ .

$M, Q = p, \ell$	ω_0	ω_1	ω_2
1.0, 0.01, 0.1	0.248415 - 0.125343 <i>i</i>	0.202180 - 0.406096 <i>i</i>	0.161473 - 0.757232 <i>i</i>
1.0, 0.10, 0.1	0.249450 - 0.125469 <i>i</i>	0.203380 - 0.406394 <i>i</i>	0.163033 - 0.757154 <i>i</i>
1.0, 0.15, 0.1	0.250786 - 0.125622 <i>i</i>	0.204944 - 0.406721 <i>i</i>	0.165074 - 0.756888 <i>i</i>
1.0, 0.20, 0.1	0.252702 - 0.125827 <i>i</i>	0.207169 - 0.407194 <i>i</i>	0.167962 - 0.756666 <i>i</i>
1.0, 0.25, 0.1	0.255267 - 0.126061 <i>i</i>	0.210196 - 0.407624 <i>i</i>	0.171924 - 0.755751 <i>i</i>
1.0, 0.1, 0.10	0.249450 - 0.125469 <i>i</i>	0.203380 - 0.406394 <i>i</i>	0.163033 - 0.757154 <i>i</i>
1.0, 0.1, 0.15	0.278841 - 0.141384 <i>i</i>	0.227909 - 0.457936 <i>i</i>	0.185895 - 0.851341 <i>i</i>
1.0, 0.1, 0.20	0.313859 - 0.160523 <i>i</i>	0.257338 - 0.519843 <i>i</i>	0.214141 - 0.963742 <i>i</i>
1.0, 0.1, 0.21	0.321669 - 0.164814 <i>i</i>	0.263932 - 0.533709 <i>i</i>	0.220589 - 0.988814 <i>i</i>
1.0, 0.1, 0.22	0.329778 - 0.169280 <i>i</i>	0.270784 - 0.548148 <i>i</i>	0.227321 - 1.014920 <i>i</i>

on a null grid and leads to a form that is particularly suitable for numerical propagation. In these coordinates, the master equation becomes:

$$\left(4 \frac{\partial^2}{\partial u \partial v} + V(u, v)\right) \tilde{\psi}(u, v) = 0. \quad (88)$$

Table XII: Spinor field quasinormal modes for the angular sector $l = 5/2$ with $M = 1$. The values of ω_n are calculated through the 6th-order WKB scheme for selected choices of the Lorentz-violating parameter ℓ .

$M, Q = p, \ell$	ω_0	ω_1	ω_2
1.0, 0.01, 0.1	0.416610 - 0.116786i	0.377934 - 0.363845i	0.316030 - 0.648066i
1.0, 0.10, 0.1	0.418139 - 0.116959i	0.379587 - 0.364331i	0.317936 - 0.648720i
1.0, 0.15, 0.1	0.420106 - 0.117175i	0.381716 - 0.364937i	0.320394 - 0.649530i
1.0, 0.20, 0.1	0.422930 - 0.117473i	0.384782 - 0.365764i	0.323948 - 0.650607i
1.0, 0.25, 0.1	0.426690 - 0.117846i	0.388879 - 0.366786i	0.328716 - 0.651885i
1.0, 0.1, 0.10	0.418139 - 0.116959i	0.379587 - 0.364331i	0.317936 - 0.648720i
1.0, 0.1, 0.15	0.468230 - 0.131478i	0.425037 - 0.409658i	0.356325 - 0.729529i
1.0, 0.1, 0.20	0.528012 - 0.148883i	0.479302 - 0.464003i	0.402280 - 0.826403i
1.0, 0.1, 0.21	0.541355 - 0.152778i	0.491418 - 0.476165i	0.412560 - 0.848080i
1.0, 0.1, 0.22	0.555218 - 0.156828i	0.504009 - 0.488813i	0.423251 - 0.870618i

The continuous problem is then replaced by its lattice counterpart. The (u, v) plane is sampled by a set of discrete points, and the differential equation is approximated through finite-difference relations on this null mesh. With this discretization, the value of the perturbation field at each new grid point is obtained from the neighboring points already known, so that the waveform is advanced step by step throughout the numerical domain

$$\tilde{\psi}(N) = -\tilde{\psi}(S) + \tilde{\psi}(W) + \tilde{\psi}(E) - \frac{h^2}{8}V(S)\left[\tilde{\psi}(W) + \tilde{\psi}(E)\right] + \mathcal{O}(h^4). \quad (89)$$

The numerical evolution is initialized on a uniform lattice in the (u, v) plane, whose spacing is fixed by the step size h . For each null cell, four grid points are assigned: the lower corner $S = (u, v)$, the two neighboring points $W = (u + h, v)$ and $E = (u, v + h)$, and the future vertex $N = (u + h, v + h)$, where the field value is obtained from the finite-difference update rule. The integration begins once the perturbation data are specified on the two initial null segments, $u = u_0$ and $v = v_0$. On the boundary $u = u_0$, the initial disturbance is prescribed as a Gaussian pulse, with center v_c and width σ . This pulse supplies the initial signal that is subsequently propagated across the full computational grid

$$\tilde{\psi}(\tilde{u} = u_0, v) = Ae^{-(v-v_0)^2/2\sigma^2}, \quad \tilde{\psi}(u, v_0) = \tilde{\psi}_0. \quad (90)$$

The evolution is started by fixing the second null boundary at $v = v_0$, where the condition $\tilde{\psi}(u, v_0) = 0$ is imposed. This choice provides a simple initial segment and avoids introducing

spurious contributions from that side of the grid. Once the boundary data have been specified, the finite-difference algorithm advances the field across the null lattice, determining $\tilde{\psi}$ at each new point from the neighboring values already computed. The update therefore follows the causal ordering naturally encoded in the (u, v) discretization.

In the present analysis, we restrict attention to massless perturbations and set the black hole mass to $M = 1$. The initial signal is introduced as a Gaussian packet located at $v = 0$ with width $\sigma = 1$, while the complementary boundary contribution is taken to vanish. The numerical domain covers the interval $0 \leq u, v \leq 1000$ and is divided with the uniform step size $h = 0.1$. This resolution is sufficient to resolve the quasinormal ringing and the subsequent decay of the perturbation signal.

To make the time-domain treatment consistent with the previous frequency-domain analysis, the numerical evolution is carried out for the different spin sectors considered in this work. The corresponding results are presented (with their comparison as well) in the following subsections.

A. Scalar perturbations

We begin with the scalar channel and evolve the corresponding master variable on the background given by Eq. (6). The resulting profiles are displayed in Fig. 15 for the parameter choice $M = 1$ and $Q = p = 0.1$, while the Lorentz-violating parameter is varied as $\ell = 0.1, 0.2, 0.3, 0.4$. The upper-left, upper-right, and lower panels refer, respectively, to the modes $l = 0, l = 1$, and $l = 2$. After the initial pulse crosses the numerical domain, the field enters a ringdown stage described by oscillations with a decreasing amplitude. This behavior is the time-domain counterpart of the quasinormal spectrum. A direct comparison among the curves shows that increasing ℓ shifts the scalar profile toward faster oscillations and stronger attenuation. In this manner, the Lorentz-violating parameter shortens the lifetime of the scalar signal, consistently with the increase of $|\text{Im}(\omega)|$ observed in the quasinormal frequencies.

Figure 16 presents the same evolutions through $\ln |\tilde{\psi}|$, keeping the same values of l and ℓ . This representation makes the decay pattern easier to identify. During the ringdown interval, the logarithmic amplitude follows an almost linear trend, as expected for an exponentially damped signal. At later times, the curves depart from this linear behavior, indicating the gradual dominance of the tail contribution. The ordering of the profiles shows that larger ℓ values lead to faster attenuation of the scalar perturbation. Hence, the waveform decays over a shorter time interval.

The final stage of the scalar evolution is emphasized in Fig. 17, where the signal is represented on a \ln - \ln scale. The same organization of panels is adopted in order to compare the three angular sectors directly. In this form, the late-time regime appears more clearly. The numerical curves therefore recover the standard tail behavior associated with perturbations around black hole backgrounds, while also showing how the Lorentz-violating parameter modifies the duration of the preceding

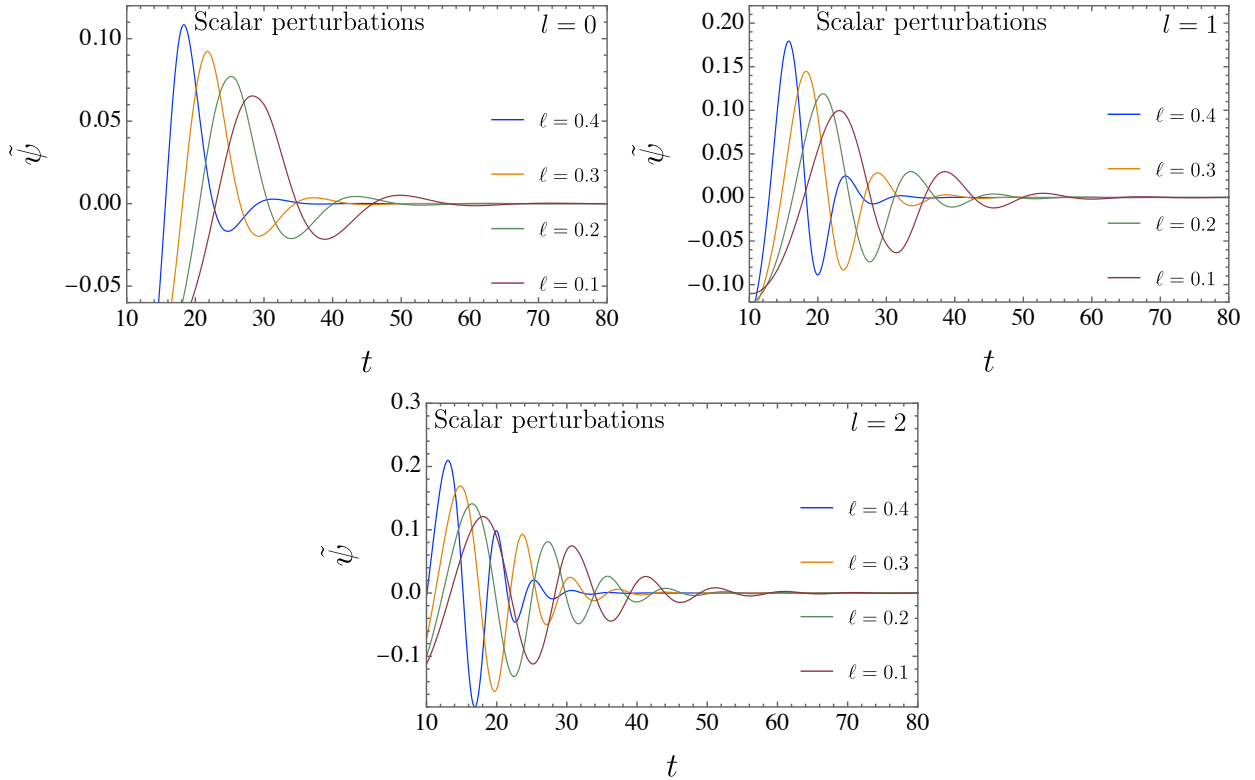


Figure 15: Scalar time-domain response $\tilde{\psi}$ for a black hole with $M = 1$ under four choices of the Lorentz-violating parameter, $\ell = 0.1, 0.2, 0.3, 0.4$. The upper-left, upper-right, and lower panels correspond to $l = 0, l = 1$, and $l = 2$, respectively, allowing a direct comparison of how the ringdown amplitude and decay rate vary as ℓ changes.

quasinormal phase.

B. Vector perturbations

We now consider the vector sector associated with the background metric in Eq. (6). The numerical profiles of $\tilde{\psi}$ are reported in Fig. 18 for $M = 1$, $Q = p = 0.1$, and $\ell = 0.1, 0.2, 0.3, 0.4$. The three panels correspond to the multipoles $l = 1, l = 2$, and $l = 3$, arranged in the upper-left, upper-right, and lower panels, respectively. After the initial pulse, the field enters the usual ringdown stage, with oscillations whose amplitudes decrease in time. Relative to the scalar sector, the vector waveforms present faster oscillation rates and a faster attenuation, so the signal remains visible for a longer interval. The same ordering with respect to ℓ also appears: larger values of the Lorentz-violating parameter increase the damping and let shorter the oscillatory regime.

The decay pattern is displayed more directly in Fig. 19, where the quantity $\ln|\tilde{\psi}|$ is plotted for the same set of parameters. In this representation, the quasinormal stage appears through nearly linear portions of the curves, reflecting the exponential suppression of the amplitude. At later times, the profiles depart from this behavior and approach the tail regime. This time-domain behavior

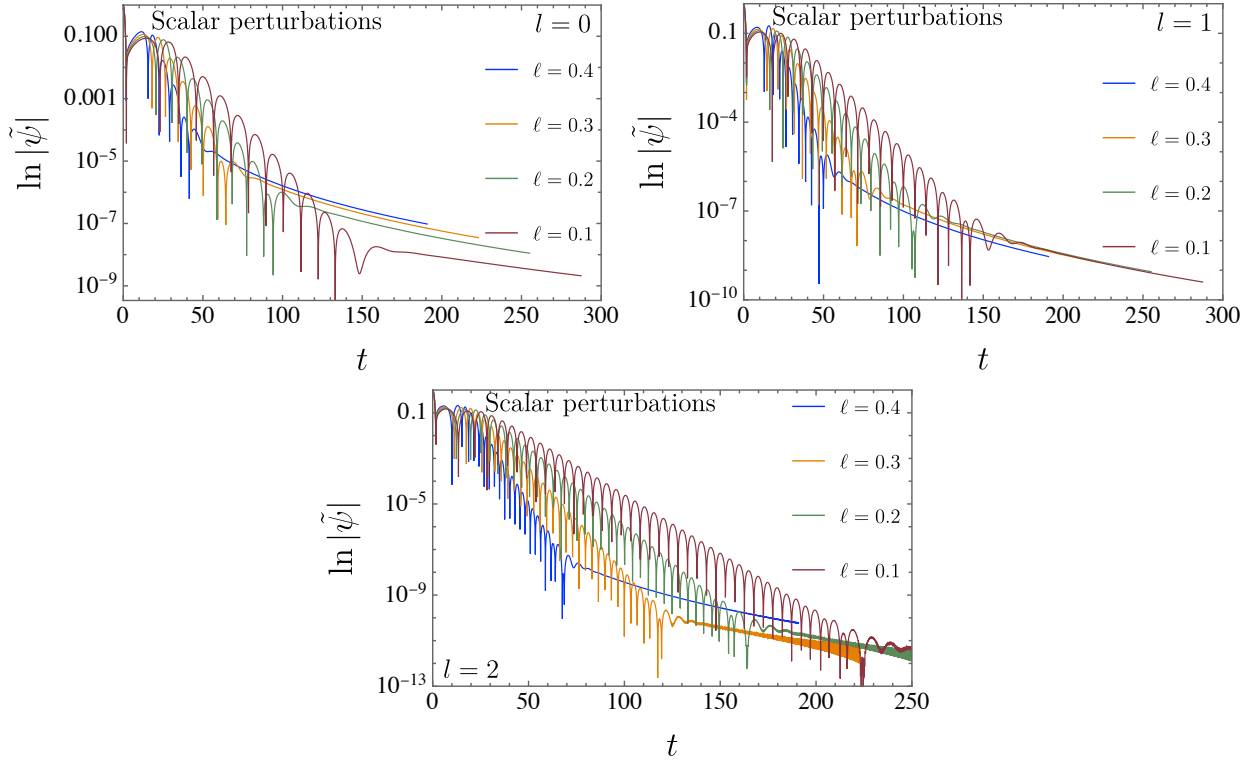


Figure 16: Logarithmic time–domain profile $\ln |\tilde{\psi}|$ of the scalar perturbation for $M = 1$ and $\ell = 0.1, 0.2, 0.3, 0.4$. The upper–left, upper–right, and lower panels display the modes $l = 0, l = 1$, and $l = 2$, respectively, highlighting the dependence of the attenuation rate on the Lorentz–violating parameter.

agrees with the frequency–domain analysis, since the modes with larger ℓ have higher damping rates. The vector perturbations also relax more rapidly than the scalar ones, which confirms the greater persistence of this sector.

The asymptotic part of the vector evolution is shown in Fig. 20 by using a double–logarithmic representation. The same panel structure is kept in order to compare the three multipoles. In this scale, the end of the exponentially damped ringdown and the subsequent power–law falloff become clearer. Although the general sequence of stages follows the scalar case, the vector field reaches the tail phase after a faster decay.

C. Tensor perturbations

The tensor sector is considered next for the black–hole geometry given in Eq. (6). Figure 21 displays the numerical evolution of the master variable $\tilde{\psi}$ for $M = 1$, $Q = p = 0.1$, and $\ell = 0.1, 0.2, 0.3, 0.4$. The panels represent the modes $l = 2, l = 3$, and $l = 4$, arranged in the upper–left, upper–right, and lower positions, respectively. Once the initial pulse has propagated through the grid, the signal settles into an oscillatory ringdown whose amplitude decreases with time. In comparison with the scalar and vector sectors, the tensor profiles exhibit higher oscillation rates

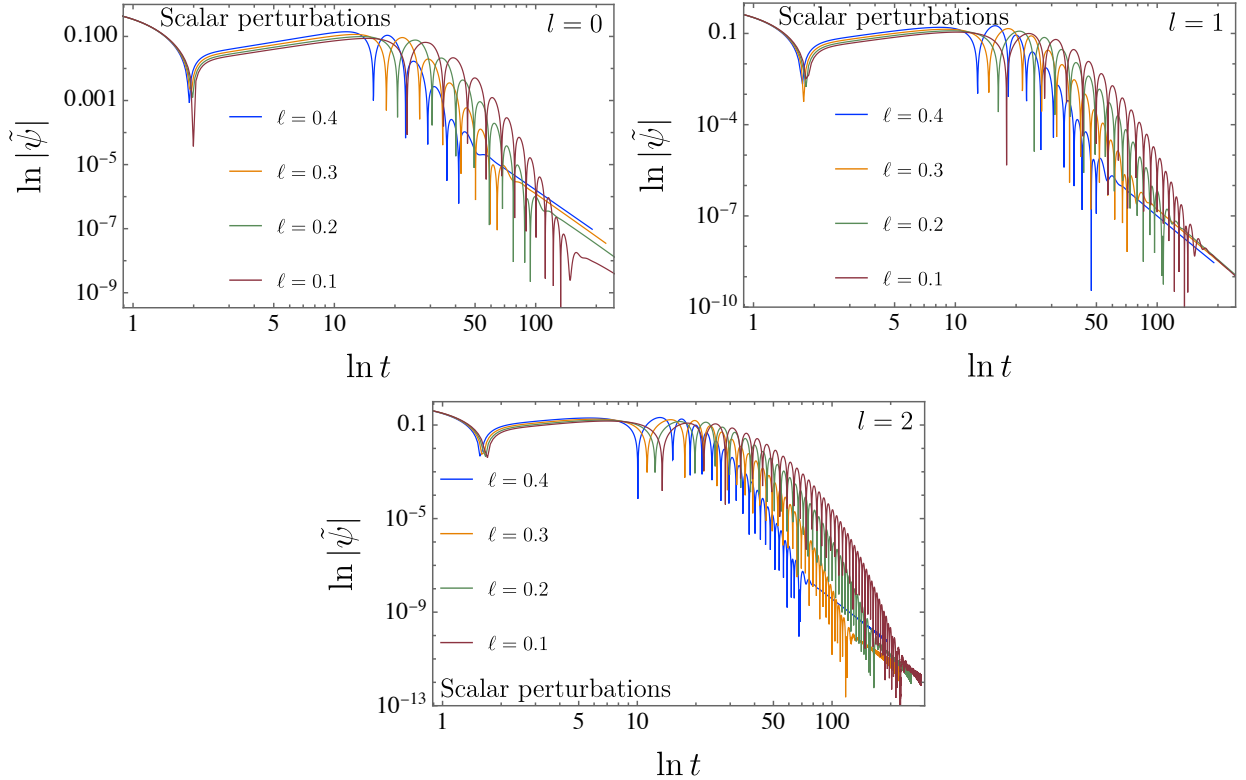


Figure 17: Late-time scalar response represented in logarithmic variables, with $\ln |\tilde{\psi}|$ displayed as a function of $\ln t$ for $M = 1$, $Q = p = 0.1$, and $\ell = 0.1, 0.2, 0.3, 0.4$. The upper-left, upper-right, and lower panels refer to the modes $l = 0$, $l = 1$, and $l = 2$, respectively, making explicit the transition toward the power-law tail at large times.

and a distinct damping pattern. The tensor signal remains visible over the interval displayed, but its attenuation is still governed by the imaginary part of the corresponding quasinormal frequencies. The dependence on the Lorentz-violating parameter follows the corrected tendency: larger values of ℓ increase the damping rate and shorten the ringing stage.

Figure 22 presents the same evolutions through $\ln |\tilde{\psi}|$, which makes the decay pattern easier to identify. During the quasinormal stage, the curves contain nearly straight portions, reflecting the exponential decrease of the waveform amplitude. At later times, this regime gives way to a tail contribution. The ordering of the curves remains consistent with the frequency-domain results, since increasing ℓ produces larger damping rates. Among the perturbative sectors analyzed here, the tensor modes still exhibit the slowest relaxation, remaining active for longer than the scalar and vector modes within the parameter range considered.

The final stage of the tensor evolution is isolated in Fig. 23 through a double-logarithmic plot with the same panel arrangement. In this representation, the transition from the ringdown regime to the asymptotic power-law decay becomes clearer. Although the sequence of stages resembles the one obtained for scalar and vector perturbations, the tensor field displays a more persistent late-time contribution over the interval shown. However, increasing ℓ does not lengthen the ringing

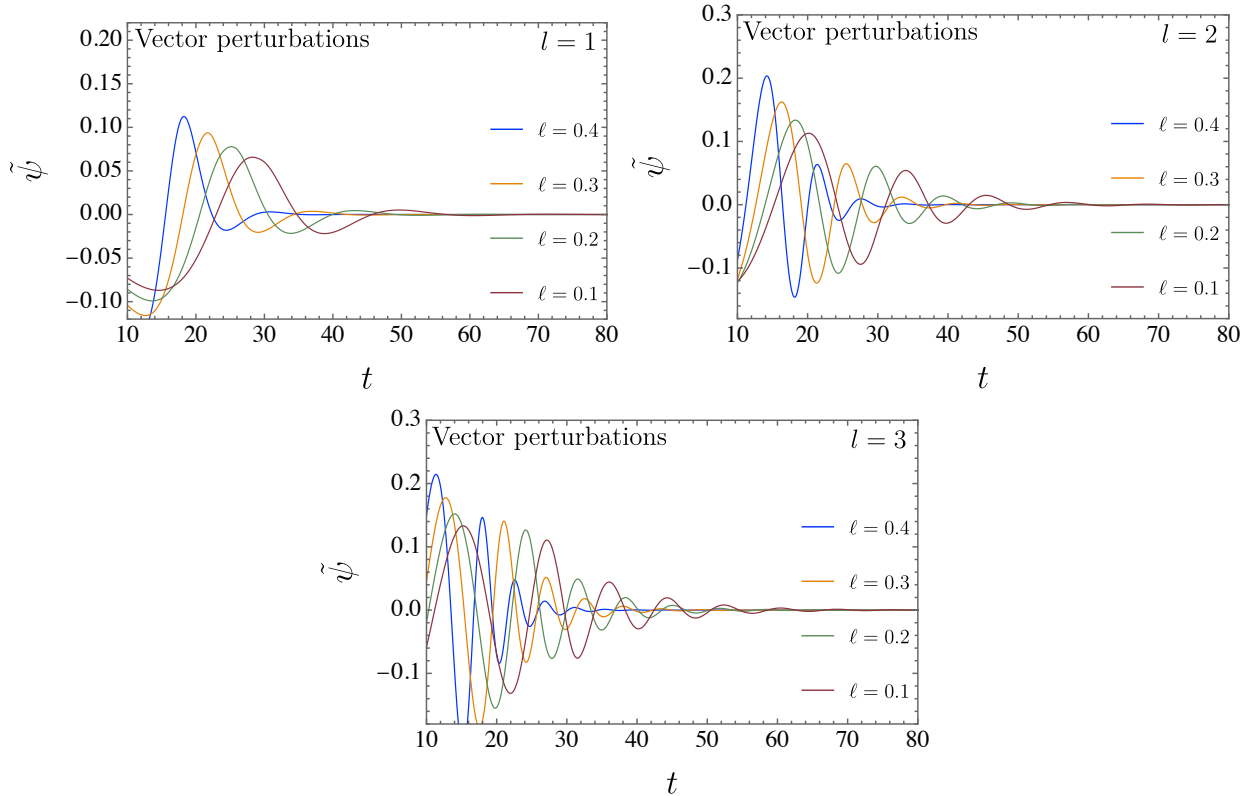


Figure 18: Vector perturbation profiles $\tilde{\psi}$ obtained in the time domain for $M = 1$, $Q = p = 0.1$, and $\ell = 0.1, 0.2, 0.3, 0.4$. The panels show the multipoles $l = 1$, $l = 2$, and $l = 3$ in the upper-left, upper-right, and lower positions, respectively, allowing the dependence of the ringdown signal on the Lorentz-violating parameter to be compared.

stage; instead, it enhances the damping rate, in agreement with the frequency-domain behavior. In this way, tensor perturbations remain the slowest-relaxing sector among those considered here, while larger values of ℓ shorten their decay time within the tensor sector itself.

D. Spinor perturbations

Spinor perturbations provide the final part of the time-domain analysis for the spacetime introduced in Eq. (6). The numerical signal $\tilde{\psi}$ is shown in Fig. 24 for $M = 1$, $Q = p = 0.1$, and $\ell = 0.1, 0.2, 0.3, 0.4$. The three panels display the half-integer modes $l = 1/2$, $l = 3/2$, and $l = 5/2$, respectively. After the initial Gaussian pulse evolves through the grid, the waveform enters a ringdown interval, where the oscillations are progressively suppressed. The spinor response differs from the bosonic cases: its oscillation frequency is higher than those obtained in the vector and tensor sectors, while its attenuation follows the damping scale determined by the corresponding quasinormal frequencies. Increasing ℓ does not delay the decay; instead, it enhances the damping rate and shortens the ringdown stage.

The decay rate is examined in Fig. 25 through the logarithmic amplitude $\ln|\tilde{\psi}|$. In this plot,

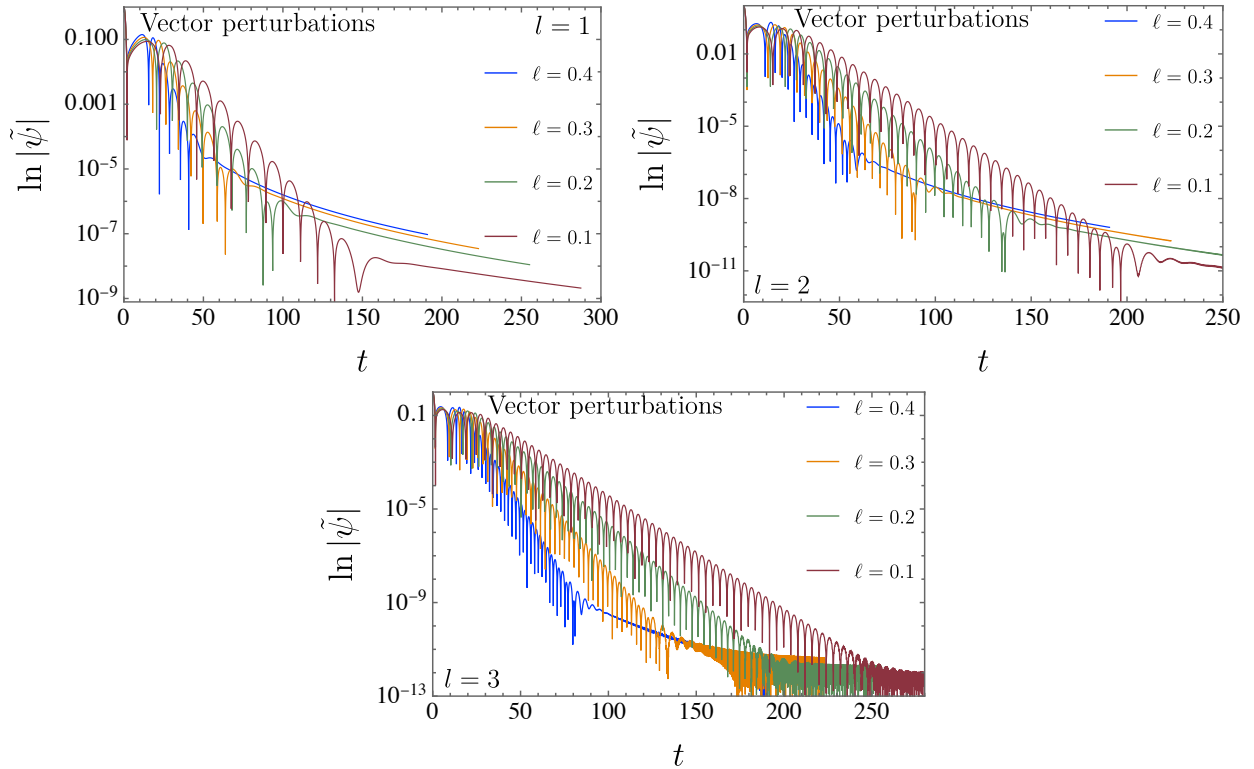


Figure 19: Logarithmic time–domain evolution of the vector perturbation, represented by $\ln|\tilde{\psi}|$, for $M = 1$, $Q = p = 0.1$, and $\ell = 0.1, 0.2, 0.3, 0.4$. The upper–left, upper–right, and lower panels correspond to $l = 1, l = 2$, and $l = 3$, respectively, displaying the attenuation pattern of each vector mode.

the quasinormal regime appears as an approximately linear portion of each curve, while the subsequent bending indicates the departure from exponential damping and the onset of the tail. The slope becomes steeper as ℓ grows, showing that the Lorentz–violating parameter strengthens the attenuation of the spinor perturbation. Thus, within the parameter range considered, the spinor field occupies an intermediate position in the relaxation sequence: it decays more slowly than the scalar field, but faster than the vector and tensor fields.

Figure 26 isolates the asymptotic regime by representing the signal on a \ln – \ln scale. This form makes the algebraic tail visible after the quasinormal ringing has faded. Although the same general pattern found for bosonic perturbations is recovered, the spinor sector follows its own attenuation scale. The full comparison among the sectors indicates the persistence ordering tensor $>$ vector $>$ spinor $>$ scalar within the plotted interval, while increasing ℓ shortens the decay time inside each sector.

A direct comparison of all spin configurations is provided in Fig. 27 for $\ell = p = Q = 0.1$ and $M = 1$. The waveform ordering reflects the structure of the effective potentials displayed in Fig. 14. In particular, during the early oscillatory stage, the temporal profiles follow the sequence suggested by $V_\psi > V_s > V_v > V_t$, once the scalar potential is consistently evaluated.

Therefore, we have verified that the time–domain evolutions carried out for the four perturbative

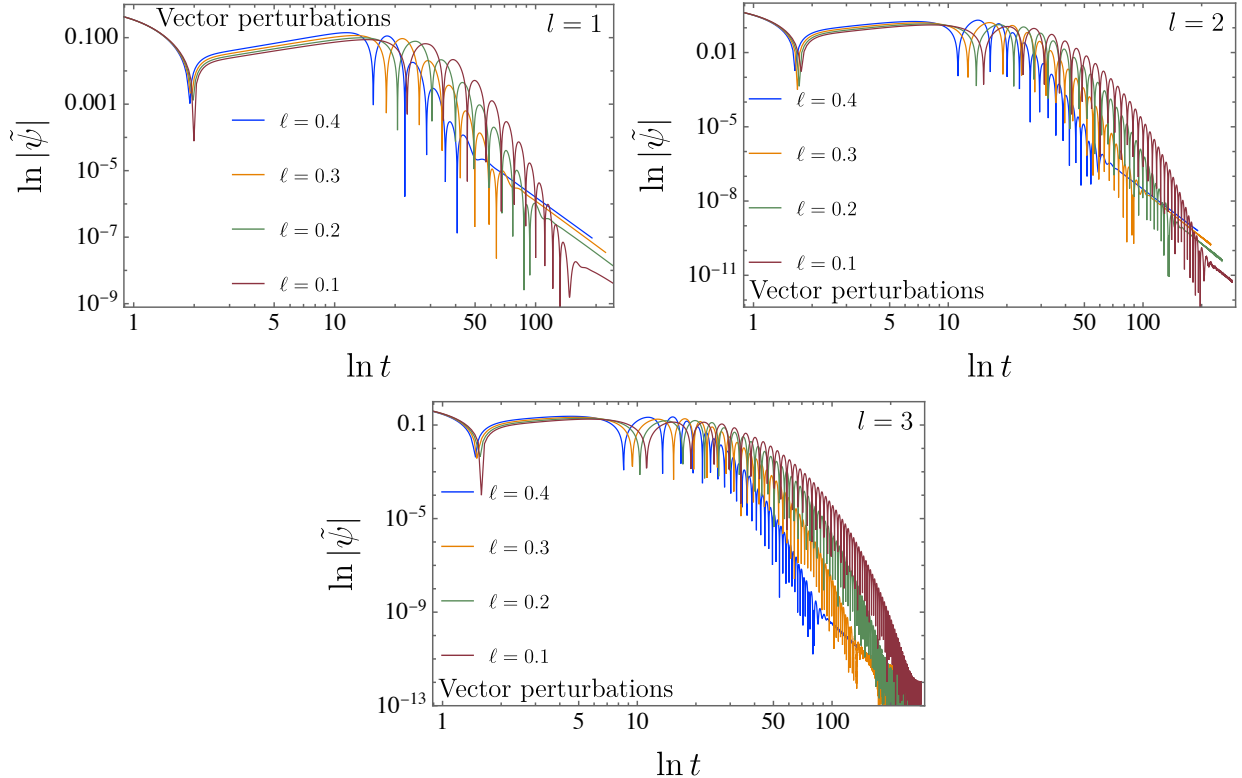


Figure 20: Asymptotic vector response displayed in a log–log representation, with $\ln |\tilde{\psi}|$ plotted versus $\ln t$ for $M = 1$, $Q = p = 0.1$, and $\ell = 0.1, 0.2, 0.3, 0.4$. The panels show the modes $l = 1$, $l = 2$, and $l = 3$ in the upper–left, upper–right, and lower positions, respectively, making the late–time power–law tail visible after the ringdown stage.

sectors, $s = 0, 1/2, 1$, and 2 , do not reveal any echo signal. This behavior follows from the structure of the effective potentials in the tortoise coordinate r^* . For each multipole l , the potential contains only one barrier and does not develop a secondary peak or a trapping well. In other words, the waveform displays the standard sequence of ringdown and late–time decay, without repeated delayed pulses.

IX. CONCLUSION

In this work, we investigated the perturbative dynamics, tidal effects, time delay, and relativistic frequency shifts associated with a dyonic Kalb–Ramond black hole. The background geometry was controlled by the mass M , the electric charge Q , the magnetic charge p , and the Lorentz–violating parameter ℓ , while the electric and magnetic sectors entered the main physical quantities through the effective combination $P_\ell^2 = \frac{Q^2}{(1-\ell)^2} + \frac{p^2}{1-2\ell}$. This structure showed that the Lorentz–violating parameter weighted the electric and magnetic charges differently, thereby modifying the horizon structure, the free-fall dynamics, the tidal response, and the perturbative spectrum. In the limit $\ell \rightarrow 0$, the dyonic Reissner–Nordström result was recovered, whereas the purely electric and uncharged Kalb–Ramond

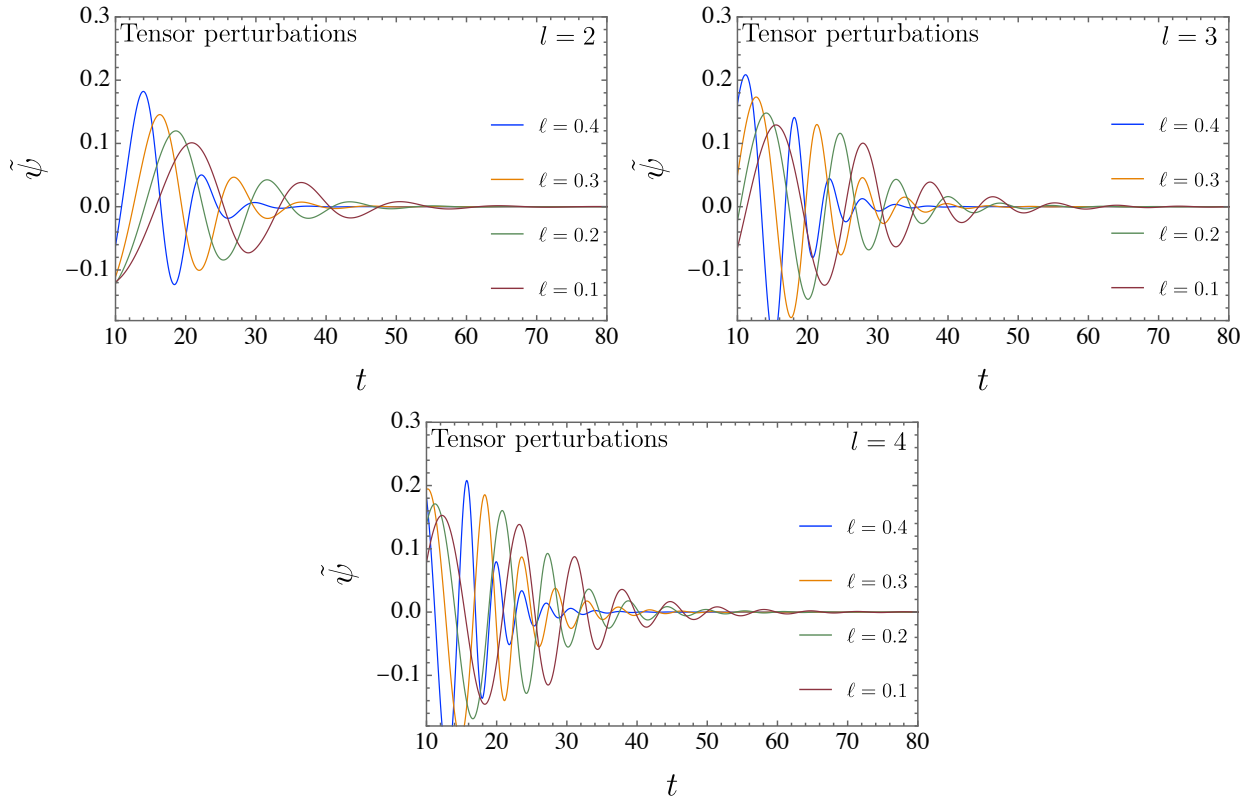


Figure 21: Time-domain tensor waveforms $\tilde{\psi}$ for $M = 1$, $Q = p = 0.1$, and $\ell = 0.1, 0.2, 0.3, 0.4$. The upper-left, upper-right, and lower panels correspond to the multipoles $l = 2, l = 3$, and $l = 4$, respectively, showing how the Lorentz-violating parameter affects the amplitude and damping of the tensor signal.

configurations were obtained through the corresponding charge reductions.

We first analyzed the gravitational Doppler effect for radial signal exchange between freely falling and static observers. For a source released from the asymptotic region, the exterior velocity approached the speed of light at the event horizon, and the frequency ratio measured by a static observer tended to zero for signals emitted outward by the infalling source. Conversely, signals emitted by the static observer and received by the freely falling observer yielded a finite horizon value equal to $1/2$. Inside the two-horizon region, the frequency ratio displayed a transition controlled by the radius $r_m = P_\ell^2/M$, which separated the redshift and blueshift regimes. The numerical analysis showed that increasing the dyonic charge shifted the frequency ratio upward and weakened the corresponding gravitational Doppler redshift.

We then computed the tidal forces experienced by a neutral body in radial free fall. The radial component contained the usual Schwarzschild stretching term together with a dyonic contribution that acted in the opposite direction near the inner region. As a result, the radial tidal force changed sign at $R_0^{\text{rad}} = \frac{3P_\ell^2}{2M}$, whereas its extremum occurred at $R_{\text{max}}^{\text{rad}} = \frac{2P_\ell^2}{M}$. The angular tidal force also changed sign, with its zero located at $R_0^{\text{ang}} = \frac{P_\ell^2}{M}$, and its minimum located at $R_{\text{min}}^{\text{ang}} = \frac{4P_\ell^2}{3M}$. Together with the turning radius $R_{\text{stop}} = P_\ell^2/(2M)$, these quantities satisfied the ordering $R_{\text{stop}} < R_0^{\text{ang}} <$

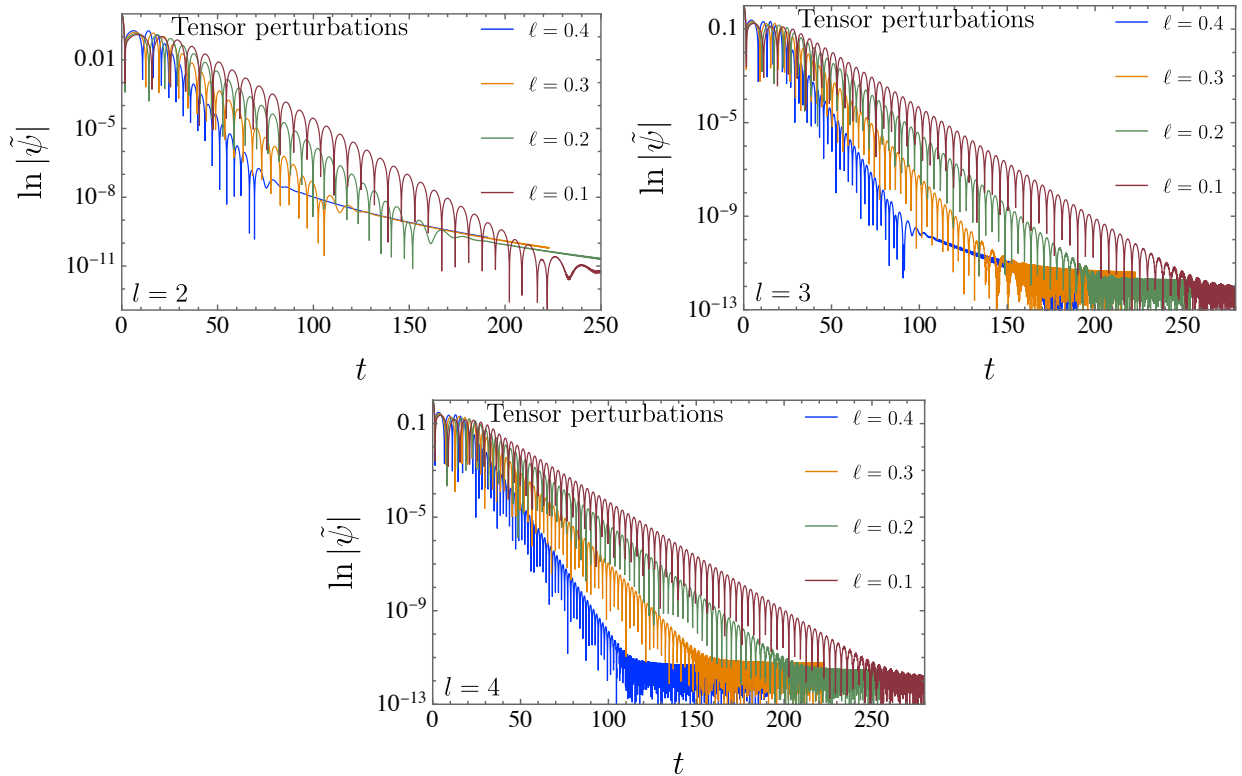


Figure 22: Logarithmic time–domain profiles of tensor perturbations, given by $\ln |\tilde{\psi}|$, for $M = 1$, $Q = p = 0.1$, and $\ell = 0.1, 0.2, 0.3, 0.4$. The panels correspond to the modes $l = 2, l = 3$, and $l = 4$ in the upper–left, upper–right, and lower positions, respectively, showing how the attenuation of the tensor signal changes with the Lorentz–violating parameter.

$R_{\min}^{\text{ang}} < R_0^{\text{rad}} < R_{\max}^{\text{rad}}$. This hierarchy indicated that the radial tidal component reversed its sign before the angular one during inward motion. The charge-sector plots showed that increasing either Q/M or p/M shifted all characteristic tidal radii toward larger values, while the outer and inner horizons approached each other until the extremal limit was reached.

The gravitational time delay was also evaluated for null trajectories in the same geometry. After subtracting the flat-space contribution, the resulting delay depended on the source position, the observer position, the closest-approach radius, and the dyonic parameters. The shifted time delay showed that the electric and magnetic charges reduced the delay relative to the reference configuration used in the numerical analysis. The Lorentz–violating parameter modified this behavior through the same effective dyonic combination that had appeared in the horizon, Doppler, and tidal sectors.

We further derived the effective potentials for scalar, vector, tensor, and spinor perturbations. The bosonic sectors were written in a common Schrödinger–like form, while the spinor sector was described by a pair of supersymmetric partner potentials, from which the representative potential V_{ψ}^{+} was used. After substituting the dyonic Kalb–Ramond metric, the resulting potentials displayed single-barrier profiles for the parameter ranges considered. This feature indicated that the

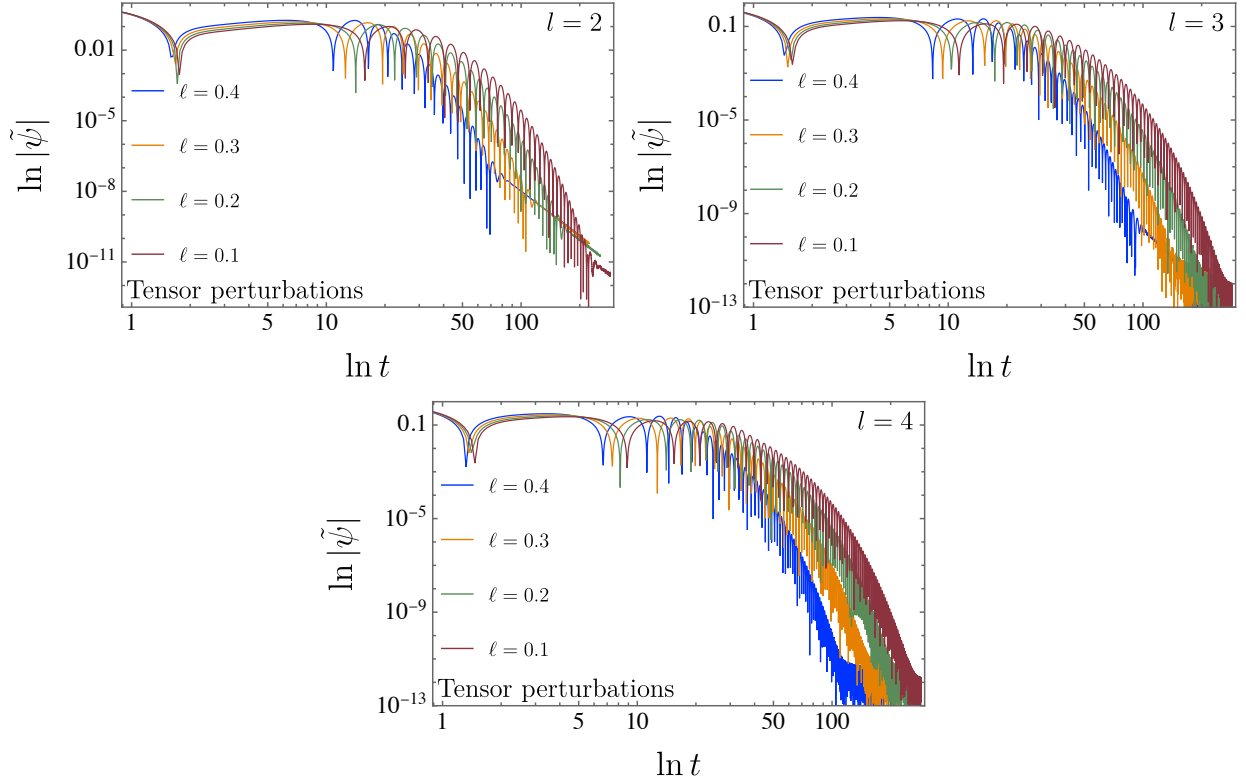


Figure 23: Late-time tensor signal in logarithmic representation, with $\ln |\tilde{\psi}|$ plotted as a function of $\ln t$ for $M = 1$, $Q = p = 0.1$, and $\ell = 0.1, 0.2, 0.3, 0.4$. The upper-left, upper-right, and lower panels display the modes $l = 2$, $l = 3$, and $l = 4$, respectively, making evident the algebraic tail that governs the asymptotic decay of the waveform.

perturbative sectors did not support echo-like structures in the cases analyzed here.

The quasinormal spectra were obtained through the sixth-order WKB approximation. For scalar, vector, tensor, and spinor perturbations, the numerical results showed that the Lorentz-violating parameter supplied the dominant correction to the quasinormal frequencies. The dyonic charge sector produced milder changes, although its effect became more visible for higher multipoles. In general, larger values of ℓ modified both the real and imaginary parts of the modes, showing that Lorentz violation affected not only the oscillation frequency but also the damping pattern of the ringdown. The spinor sector exhibited additional sensitivity at low multipole number, especially for higher overtones, so those modes required a more careful interpretation within the WKB scheme.

Finally, the time-domain evolution was obtained through the characteristic integration method. The scalar, vector, tensor, and spinor waveforms displayed the expected sequence of damped quasinormal ringing followed by a late-time power-law tail. The logarithmic profiles made the exponential attenuation stage clear, while the double logarithmic plots revealed the asymptotic tail behavior. These results confirmed the qualitative picture inferred from the effective potentials: the perturbations evolved through a standard black hole ringdown phase, and no echo-like signal appeared for the single-barrier configurations considered.

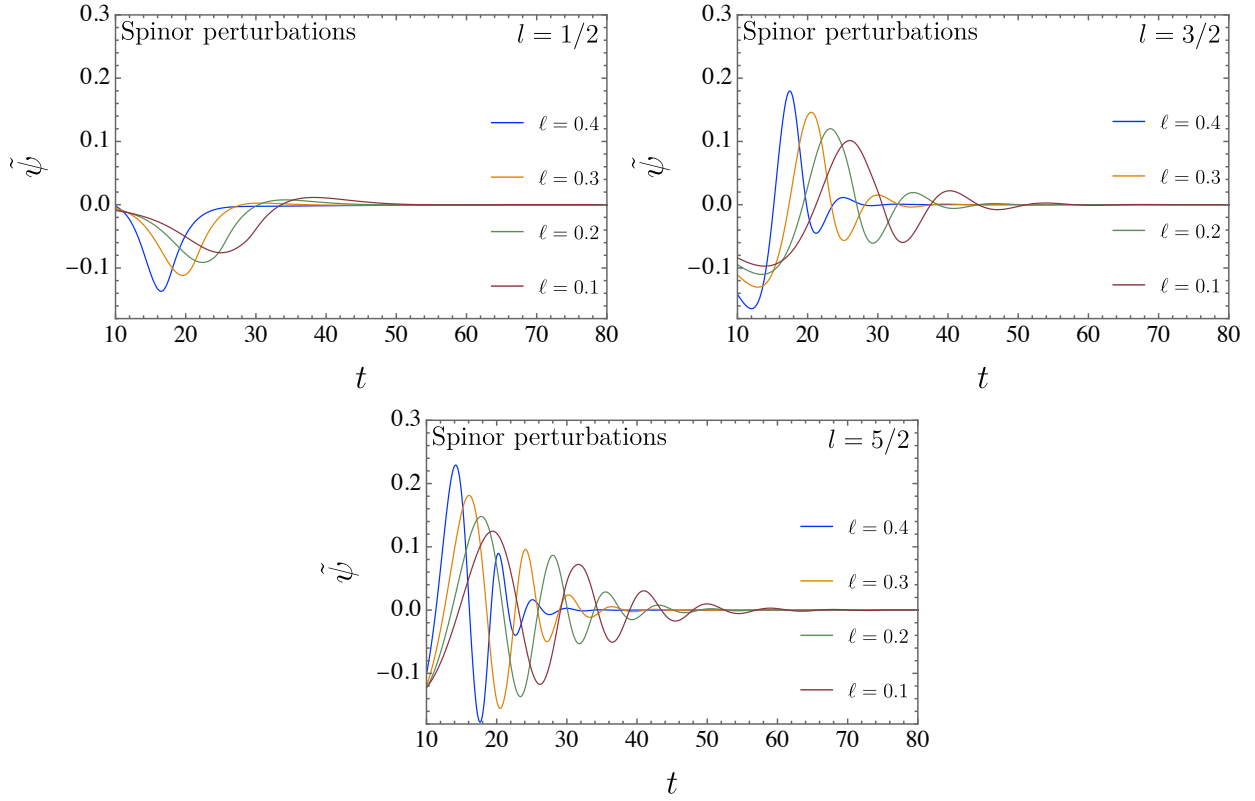


Figure 24: Time-domain spinor waveforms $\tilde{\psi}$ for $M = 1$, $Q = p = 0.1$, and $\ell = 0.1, 0.2, 0.3, 0.4$. The upper-left, upper-right, and lower panels display the modes $l = 1/2$, $l = 3/2$, and $l = 5/2$, respectively.

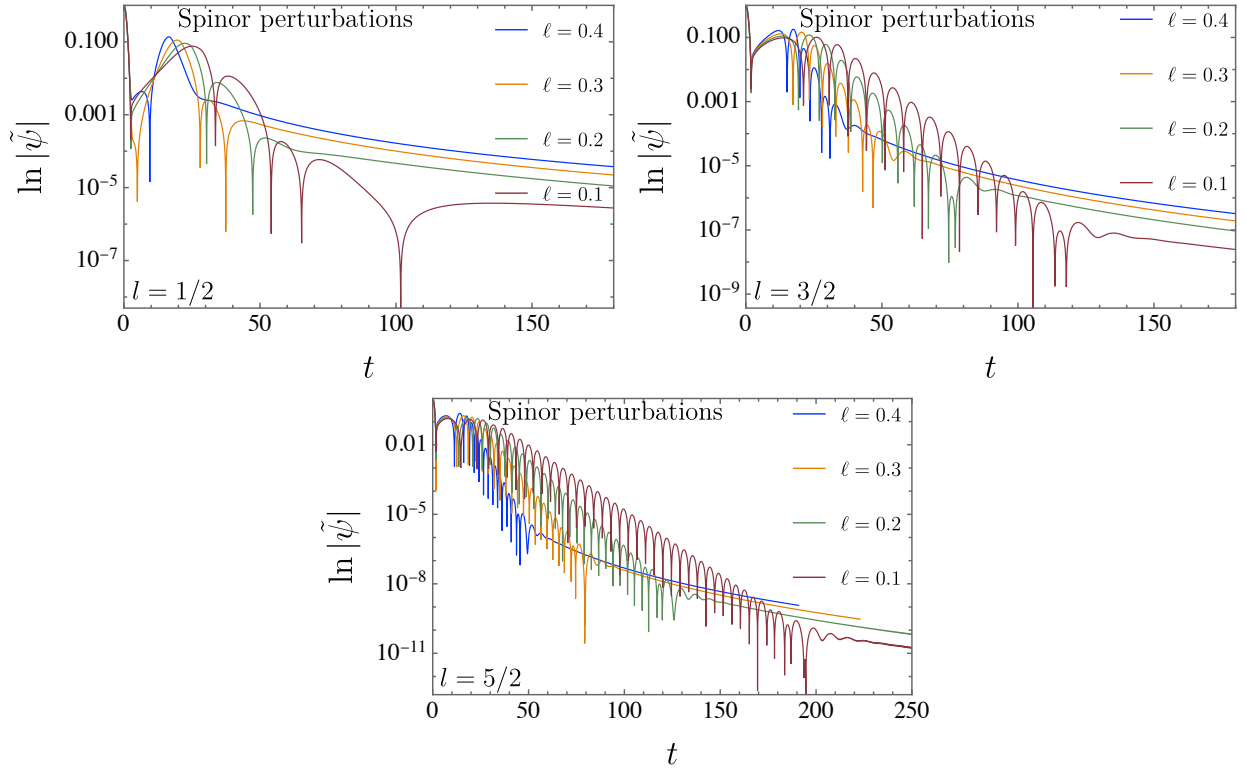


Figure 25: Logarithmic time-domain profiles of the spinor perturbation, represented by $\ln|\tilde{\psi}|$, for $M = 1$, $Q = p = 0.1$, and $\ell = 0.1, 0.2, 0.3, 0.4$. The upper-left, upper-right, and lower panels correspond to the modes $l = 1/2$, $l = 3/2$, and $l = 5/2$, respectively.

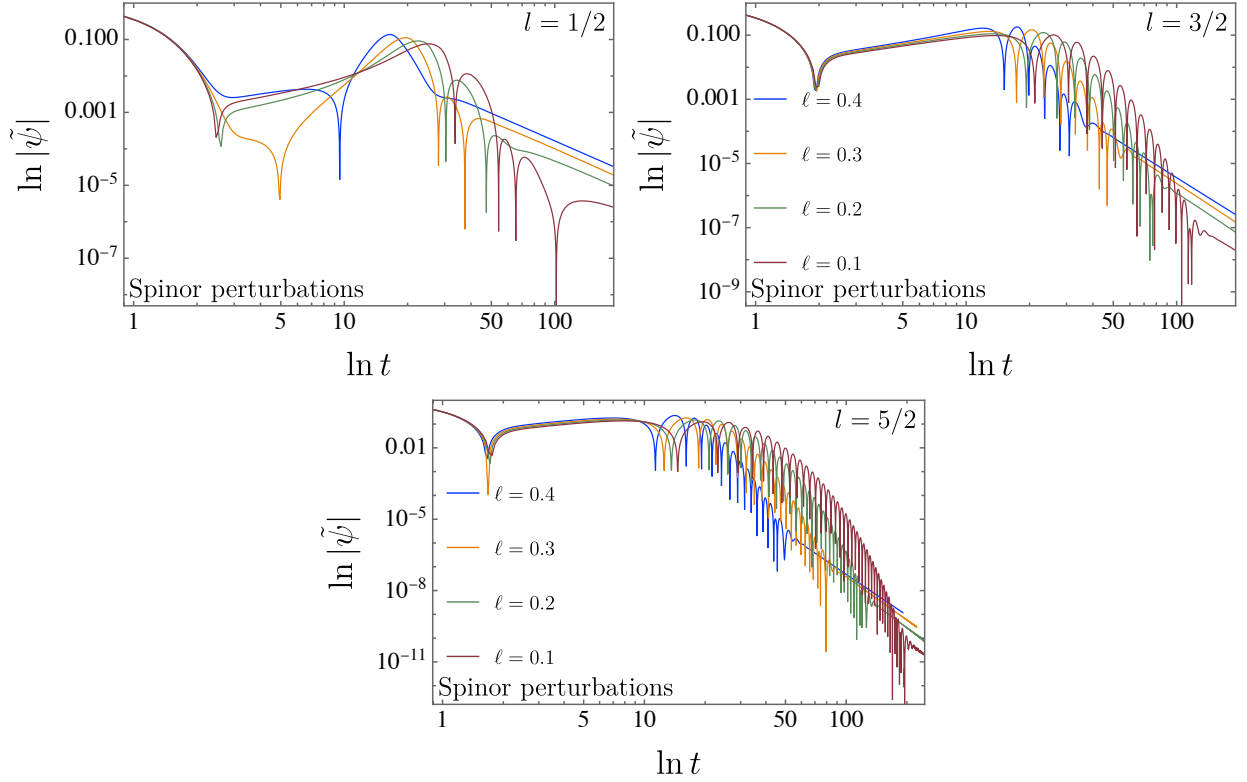


Figure 26: Asymptotic spinor signal shown in a log–log representation, where $\ln |\tilde{\psi}|$ is plotted as a function of $\ln t$ for $M = 1$, $Q = p = 0.1$, and $\ell = 0.1, 0.2, 0.3, 0.4$. The upper–left, upper–right, and lower panels correspond to the modes $l = 1/2$, $l = 3/2$, and $l = 5/2$, respectively.

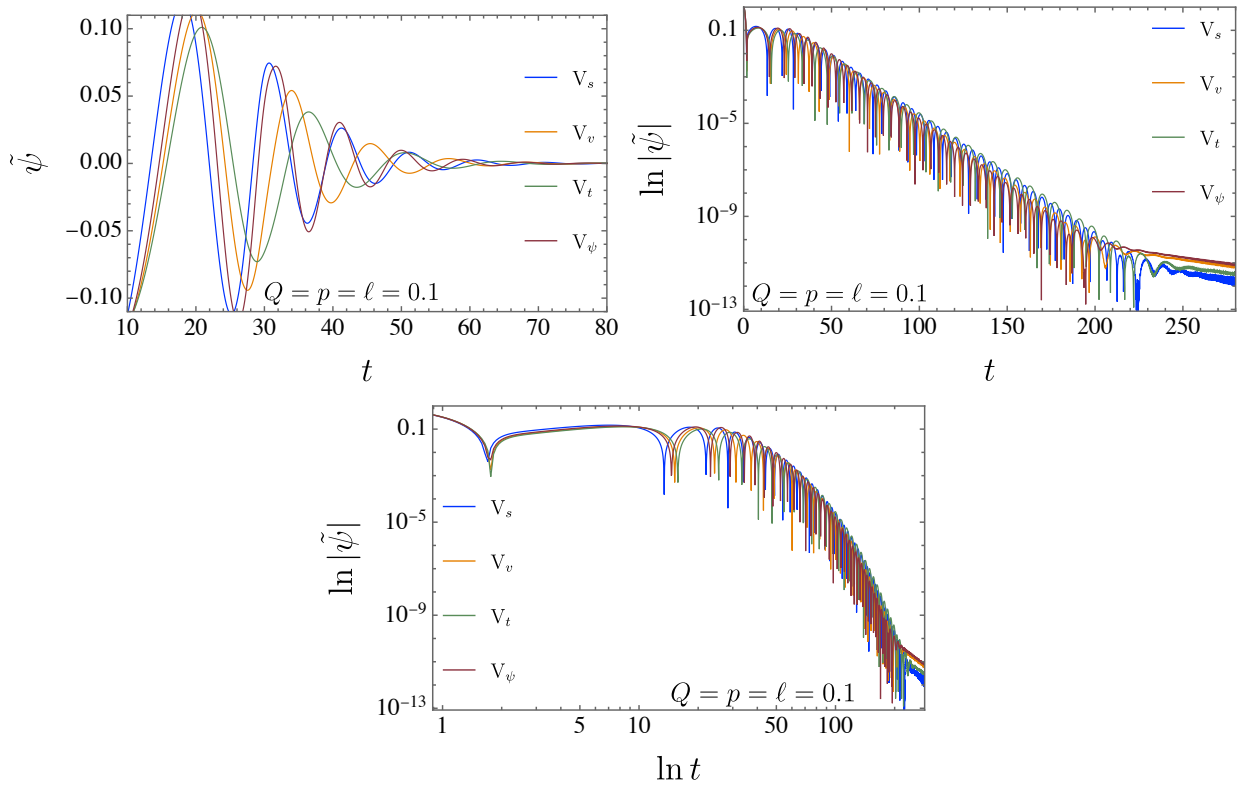


Figure 27: Time–domain comparison among the scalar, vector, tensor, and spinor sectors for $\ell = 0.1$, $M = 1$, and $Q = p = 0.1$. The figure displays both $\tilde{\psi}$ and $\ln |\tilde{\psi}|$.

As a further extension, we may examine the gravitational lensing sector by applying the Gauss–Bonnet method in the weak–deflection regime and Tsukamoto’s formalism in the strong–deflection regime. Additional developments may include the calculation of greybody factors and greybody bounds, together with particle creation through the quantum tunneling method for bosonic and fermionic modes. Neutrino oscillations and matter accretion also provide natural directions for broadening the physical analysis of this spacetime. These studies have already been carried out, and the corresponding manuscripts are now in their final stage; they are expected to appear on arXiv shortly.

Acknowledgments

A.A.A.F. is supported by Conselho Nacional de Desenvolvimento Científico e Tecnológico (CNPq) with project number 150223/2025-0.

Data Availability Statement

Data Availability Statement: No Data associated with the manuscript

-
- [1] V. A. Kostelecký and C. D. Lane, “Constraints on lorentz violation from clock-comparison experiments,” *Physical Review D*, vol. 60, no. 11, p. 116010, 1999.
 - [2] D. Colladay and V. A. Kostelecký, “Cpt violation and the standard model,” *Physical Review D*, vol. 55, no. 11, p. 6760, 1997.
 - [3] V. A. Kostelecký, “Gravity, lorentz violation, and the standard model,” *Physical Review D*, vol. 69, no. 10, p. 105009, 2004.
 - [4] V. A. Kostelecký and S. Samuel, “Spontaneous breaking of lorentz symmetry in string theory,” *Physical Review D*, vol. 39, no. 2, p. 683, 1989.
 - [5] V. A. Kostelecký and N. Russell, “Data tables for lorentz and cpt violation,” *Reviews of Modern Physics*, vol. 83, no. 1, pp. 11–31, 2011.
 - [6] R. Bluhm, S.-H. Fung, and V. A. Kostelecký, “Spontaneous lorentz and diffeomorphism violation, massive modes, and gravity,” *Physical Review D—Particles, Fields, Gravitation, and Cosmology*, vol. 77, no. 6, p. 065020, 2008.
 - [7] R. Bluhm and V. A. Kostelecký, “Spontaneous lorentz violation, nambu-goldstone modes, and gravity,” *Physical Review D—Particles, Fields, Gravitation, and Cosmology*, vol. 71, no. 6, p. 065008, 2005.

- [8] R. Bluhm and Y. Zhi, “Spontaneous and Explicit Spacetime Symmetry Breaking in Einstein–Cartan Theory with Background Fields,” *Symmetry*, vol. 16, no. 1, p. 25, 2024.
- [9] R. V. Maluf, V. Santos, W. T. Cruz, and C. A. S. Almeida, “Matter-gravity scattering in the presence of spontaneous Lorentz violation,” *Phys. Rev. D*, vol. 88, no. 2, p. 025005, 2013.
- [10] R. V. Maluf, C. A. S. Almeida, R. Casana, and M. M. Ferreira, Jr., “Einstein-Hilbert graviton modes modified by the Lorentz-violating bumblebee Field,” *Phys. Rev. D*, vol. 90, no. 2, p. 025007, 2014.
- [11] R. Bluhm, H. Bossi, and Y. Wen, “Gravity with explicit spacetime symmetry breaking and the Standard-Model Extension,” *Phys. Rev. D*, vol. 100, no. 8, p. 084022, 2019.
- [12] V. A. Kostelecký and S. Samuel, “Photon and graviton masses in string theories,” *Physical Review Letters*, vol. 66, no. 14, p. 1811, 1991.
- [13] T. Jacobson and D. Mattingly, “Einstein-aether waves,” *Physical Review D*, vol. 70, no. 2, p. 024003, 2004.
- [14] O. Bertolami and J. Paramos, “The Flight of the bumblebee: Vacuum solutions of a gravity model with vector-induced spontaneous Lorentz symmetry breaking,” *Phys. Rev. D*, vol. 72, p. 044001, 2005.
- [15] R. Casana, A. Cavalcante, F. P. Poulis, and E. B. Santos, “Exact Schwarzschild-like solution in a bumblebee gravity model,” *Phys. Rev. D*, vol. 97, no. 10, p. 104001, 2018.
- [16] W. Liu, C. Wen, and J. Wang, “Lorentz violation alleviates gravitationally induced entanglement degradation,” *JHEP*, vol. 01, p. 184, 2025.
- [17] A. A. Araújo Filho, “How does non-metricity affect particle creation and evaporation in bumblebee gravity?,” *JCAP*, vol. 06, p. 026, 2025.
- [18] D. Liang, R. Xu, X. Lu, and L. Shao, “Polarizations of gravitational waves in the bumblebee gravity model,” *Phys. Rev. D*, vol. 106, no. 12, p. 124019, 2022.
- [19] R. Oliveira, D. M. Dantas, and C. A. S. Almeida, “Quasinormal frequencies for a black hole in a bumblebee gravity,” *EPL*, vol. 135, no. 1, p. 10003, 2021.
- [20] H.-F. Liu, W. Liu, Y.-X. Liu, Q. Su, and D.-f. Zeng, “Gravitational-Bumblebee perturbations: Exact decoupling and isospectrality,” 5 2026.
- [21] I. Güllü and A. Övgün, “Schwarzschild-like black hole with a topological defect in bumblebee gravity,” *Annals Phys.*, vol. 436, p. 168721, 2022.
- [22] S. Kumar Jha, H. Barman, and A. Rahaman, “Bumblebee gravity and particle motion in Snyder noncommutative spacetime structures,” *JCAP*, vol. 04, p. 036, 2021.
- [23] A. A. Araújo Filho, N. Heidari, I. P. Lobo, Y. Shi, and F. S. N. Lobo, “The Flight of the Bumblebee in a Non-Commutative Geometry: A New Black Hole Solution,” 9 2025.
- [24] R. V. Maluf and J. C. S. Neves, “Black holes with a cosmological constant in bumblebee gravity,” *Phys. Rev. D*, vol. 103, no. 4, p. 044002, 2021.

- [25] M. Gonzalez-Espinoza, G. Panotopoulos, and F. Tello-Ortiz, “Cosmological implications of Bumblebee theory on an FLRW background,” 12 2025.
- [26] Z.-C. Li and H. Lu, “When Bumblebee Meets NLED: Lorentz-Violating Black Holes and Regular Spacetimes,” 5 2026.
- [27] C. Ding, C. Liu, R. Casana, and A. Cavalcante, “Exact Kerr-like solution and its shadow in a gravity model with spontaneous Lorentz symmetry breaking,” *Eur. Phys. J. C*, vol. 80, no. 3, p. 178, 2020.
- [28] C. Liu, C. Ding, and J. Jing, “Thin accretion disk around a rotating Kerr-like black hole in Einstein-bumblebee gravity model,” 10 2019.
- [29] A. Ovgün, K. Jusufi, and I. Sakalli, “Gravitational lensing under the effect of Weyl and bumblebee gravities: Applications of Gauss–Bonnet theorem,” *Annals Phys.*, vol. 399, pp. 193–203, 2018.
- [30] Z. Li, G. Zhang, and A. Övgün, “Circular Orbit of a Particle and Weak Gravitational Lensing,” *Phys. Rev. D*, vol. 101, no. 12, p. 124058, 2020.
- [31] Y. Sekhmani, W. Liu, W. Deng, and K. Boshkayev, “Quasinormal Modes of Massive Scalar Perturbations in Slow-Rotation Bumblebee Black Holes with Traceless Conformal Electrodynamics,” 10 2025.
- [32] W. Deng, W. Liu, F. Long, K. Xiao, and J. Jing, “Quasinormal Modes of a Massive Scalar Field in Slowly Rotating Einstein-Bumblebee Black Holes,” 7 2025.
- [33] S. Long, Z.-w. Xia, H. Gong, Z. Cao, Q. Pan, and J. Jing, “Constraining Lorentz symmetry breaking in bumblebee gravity with extreme mass-ratio inspirals,” 5 2026.
- [34] M. Kalb and P. Ramond, “Classical direct interstring action,” *Phys. Rev. D*, vol. 9, p. 2273, 1974.
- [35] R. V. Maluf, A. A. Araújo Filho, W. Cruz, and C. Almeida, “Antisymmetric tensor propagator with spontaneous lorentz violation,” *Europhysics Letters*, vol. 124, p. 61001, 2019.
- [36] B. Altschul, Q. Bailey, and V. Kostelecky, “Lorentz violation with an antisymmetric tensor,” *Phys. Rev. D*, vol. 81, p. 065028, 2010.
- [37] K. Yang, Y.-Z. Chen, Z.-Q. Duan, and J.-Y. Zhao, “Static and spherically symmetric black holes in gravity with a background Kalb-Ramond field,” *Phys. Rev. D*, vol. 108, no. 12, p. 124004, 2023.
- [38] F. Atamurotov, D. Ortiqboev, A. Abdujabbarov, and G. Mustafa, “Particle dynamics and gravitational weak lensing around black hole in the kalb-ramond gravity,” *Eur. Phys. J. C*, vol. 82, p. 659, 2022.
- [39] A. A. A. Filho, J. A. A. S. Reis, and H. Hassanabadi, “Exploring antisymmetric tensor effects on black hole shadows and quasinormal frequencies,” *JCAP*, vol. 05, p. 029, 2024.
- [40] W.-D. Guo, Q. Tan, and Y.-X. Liu, “Quasinormal modes and greybody factor of a Lorentz-violating black hole,” *Journal of Cosmology and Astroparticle Physics*, vol. 07, p. 008, 2024.
- [41] E. L. B. Junior, J. T. S. S. Junior, F. S. N. Lobo, M. E. Rodrigues, D. Rubiera-Garcia, L. F. D. da Silva, and H. A. Vieira, “Gravitational lensing of a schwarzschild-like black hole in kalb-ramond

- gravity,” *Physical Review D*, vol. 110, no. 2, p. 024077, 2024.
- [42] E. L. B. Junior, J. T. S. S. Junior, F. S. N. Lobo, M. E. Rodrigues, D. Rubiera-Garcia, L. F. D. da Silva, and H. A. Vieira, “Spontaneous Lorentz symmetry-breaking constraints in Kalb–Ramond gravity,” *Eur. Phys. J. C*, vol. 84, no. 12, p. 1257, 2024.
- [43] E. L. B. Junior, J. T. S. S. Junior, F. S. N. Lobo, M. E. Rodrigues, D. Rubiera-Garcia, L. F. D. da Silva, and H. A. Vieira, “Periodical orbits and waveforms with spontaneous Lorentz symmetry-breaking in Kalb–Ramond gravity,” *Eur. Phys. J. C*, vol. 85, no. 5, p. 557, 2025.
- [44] S. Jumaniyozov, S. U. Khan, J. Rayimbaev, A. Abdujabbarov, S. Urinbaev, and S. Murodov, “Circular motion and qpos near black holes in kalb–ramond gravity,” *The European Physical Journal C*, vol. 84, no. 9, p. 964, 2024.
- [45] Y.-H. Jiang and X. Zhang, “Accretion of vlasov gas onto a black hole in the kalb–ramond field,” *Chinese Physics C*, 2024.
- [46] A. A. Araújo Filho, “Particle creation and evaporation in Kalb-Ramond gravity,” *JCAP*, vol. 04, p. 076, 2025.
- [47] Y. Shi, A. A. Araújo Filho, K. E. L. de Farias, V. B. Bezerra, and A. R. Queiroz, “Neutrino oscillations in a Kalb-Ramond black hole background,” 12 2025.
- [48] Y. Shi and A. A. Araújo Filho, “Influence of a Kalb-Ramond black hole on neutrino behavior,” *JHEP*, vol. 08, p. 028, 2025.
- [49] Z.-Q. Duan, J.-Y. Zhao, and K. Yang, “Electrically charged black holes in gravity with a background Kalb–Ramond field,” *Eur. Phys. J. C*, vol. 84, no. 8, p. 798, 2024.
- [50] A. al Badawi, S. Shaymatov, and I. Sakalli, “Geodesics structure and deflection angle of electrically charged black holes in gravity with a background Kalb–Ramond field,” *Eur. Phys. J. C*, vol. 84, no. 8, p. 825, 2024.
- [51] M. Zahid, J. Rayimbaev, N. Kurbonov, S. Ahmedov, C. Shen, and A. Abdujabbarov, “Electric Penrose, circular orbits and collisions of charged particles near charged black holes in Kalb–Ramond gravity,” *Eur. Phys. J. C*, vol. 84, no. 7, p. 706, 2024.
- [52] A. A. Araújo Filho, “Antisymmetric tensor influence on charged black hole lensing phenomena and time delay,” *Journal of High Energy Astrophysics*, p. 100401, 2025.
- [53] A. A. Araújo Filho, N. Heidari, J. A. A. S. Reis, and H. Hassanabadi, “The impact of an antisymmetric tensor on charged black holes: evaporation process, geodesics, deflection angle, scattering effects and quasinormal modes,” *Classical and Quantum Gravity*, vol. 42, no. 6, p. 065026, 2025.
- [54] J.-T. Yao, K.-J. He, Z.-C. Lin, and H. Yu, “Energy extraction from rotating charged black holes in kalb-ramond gravity,” *Physics Letters B*, p. 140562, 2026.
- [55] H. Chen, M. Y. Zhang, A. A. A. Filho, F. Hosseinifar, and H. Hassanabadi, “Thermal, topological, and scattering effects of an AdS charged black hole with an antisymmetric tensor background,”

Commun. Theor. Phys., vol. 78, no. 2, p. 025404, 2026.

- [56] A. A. Araújo Filho, N. Heidari, and I. P. Lobo, “A non-commutative Kalb-Ramond black hole,” *JCAP*, vol. 09, p. 076, 2025.
- [57] Y. Sekhmani, A. Al-Badawi, M. Fathi, A. Vachher, and S. G. Ghosh, “Black hole solutions surrounded by an anisotropic fluid in a Kalb–Ramond two–form background,” 3 2026.
- [58] Y. Sekhmani, S. K. Maurya, J. Rayimbaev, M. Altanji, I. Ibragimov, and S. Muminov, “Lorentz-violating ModMax black holes in phantom-enhanced Kalb–Ramond gravity: Thermodynamics and topological charges,” *Phys. Dark Univ.*, vol. 50, p. 102079, 2025.
- [59] Y. Sekhmani, A. Baruah, S. K. Maurya, J. Rayimbaev, M. Altanji, I. Ibragimov, and S. Muminov, “Kalb-Ramond black holes sourced by ModMax electrodynamics: Some perturbative properties in the phantom sector,” *Phys. Dark Univ.*, vol. 50, p. 102157, 2025.
- [60] F. Ahmed, A. Al-Badawi, and I. Sakalli, “Constraining Kalb-Ramond gravity with cloud of strings using EHT shadow observations and X-ray binary QPO data,” *Phys. Dark Univ.*, vol. 52, p. 102315, 2026.
- [61] F. Ahmed, M. Fathi, and E. O. Silva, “Charged Black Holes in KR-gravity Surrounded by Perfect Fluid Dark Matter,” 4 2026.
- [62] F. Ahmed and E. O. Silva, “Dyonic ModMax Black Holes in Kalb-Ramond gravity with a Cloud of Strings as Source,” 3 2026.
- [63] L. A. Lessa, R. B. Magalhães, and M. M. Ferreira Junior, “Self-consistency of compact objects in Lorentz-violating gravity theories,” *Phys. Rev. D*, vol. 112, no. 6, p. 064031, 2025.
- [64] W. Liu, D. Wu, and J. Wang, “Static neutral black holes in Kalb-Ramond gravity,” *JCAP*, vol. 09, p. 017, 2024.
- [65] W. Liu, D. Wu, and J. Wang, “Shadow of slowly rotating Kalb-Ramond black holes,” *JCAP*, vol. 05, p. 017, 2025.
- [66] W. Deng, W. Liu, K. Xiao, and J. Jing, “Quasinormal modes of scalar, electromagnetic, and gravitational perturbations in slowly rotating Kalb–Ramond black holes,” *Eur. Phys. J. C*, vol. 86, no. 3, p. 232, 2026.
- [67] F. M. Belchior, R. V. Maluf, A. Y. Petrov, and P. J. Porfírio, “Global monopole in a Ricci-coupled Kalb–Ramond bumblebee gravity,” *Eur. Phys. J. C*, vol. 85, no. 6, p. 658, 2025.
- [68] Y.-X. Lin, J.-Z. Liu, and Y.-X. Liu, “Dyonic Black Holes in Lorentz-Violating Gravity with a Background Kalb–Ramond Field,” 5 2026.
- [69] B. P. Abbott *et al.*, “Observation of Gravitational Waves from a Binary Black Hole Merger,” *Phys. Rev. Lett.*, vol. 116, no. 6, p. 061102, 2016.
- [70] K. Akiyama, A. Alberdi, W. Alef, J. C. Algaba, R. Anantua, K. Asada, R. Azulay, U. Bach, A.-K. Baczko, D. Ball, *et al.*, “First sagittarius a* event horizon telescope results. i. the shadow of the

- supermassive black hole in the center of the milky way,” *The Astrophysical Journal Letters*, vol. 930, no. 2, p. L12, 2022.
- [71] T. E. H. T. Collaboration, “First M87* event horizon telescope results. i. the shadow of the supermassive black hole,” *The Astrophysical Journal Letters*, vol. 875, no. 1, p. L1, 2019.
- [72] R. A. Konoplya and A. Zhidenko, “Quasinormal modes of black holes: From astrophysics to string theory,” *Reviews of Modern Physics*, vol. 83, no. 3, pp. 793–836, 2011.
- [73] R. A. Konoplya and A. Zhidenko, “Massive charged scalar field in the Kerr-Newman background I: quasinormal modes, late-time tails and stability,” *Physical Review D*, vol. 88, p. 024054, 2013.
- [74] R. Karmakar, D. J. Gogoi, and U. D. Goswami, “Quasinormal modes and thermodynamic properties of gup-corrected schwarzschild black hole surrounded by quintessence,” *International Journal of Modern Physics A*, vol. 37, no. 28n29, p. 2250180, 2022.
- [75] R. A. Konoplya, A. Zhidenko, and A. F. Zinhailo, “Higher order WKB formula for quasinormal modes and grey-body factors: recipes for quick and accurate calculations,” *Class. Quant. Grav.*, vol. 36, p. 155002, 2019.
- [76] R. Karmakar and U. D. Goswami, “Quasinormal modes, thermodynamics and shadow of black holes in Hu–Sawicki $f(R)$ gravity theory,” *The European Physical Journal C*, vol. 84, no. 9, p. 969, 2024.
- [77] R. A. Konoplya and A. Zhidenko, “Decay of a charged scalar and Dirac fields in the Kerr-Newman-de Sitter background,” *Physical Review D*, vol. 76, no. 8, p. 084018, 2007. [Erratum: Phys.Rev.D 90, 029901 (2014)].
- [78] K. D. Kokkotas, R. A. Konoplya, and A. Zhidenko, “Quasinormal modes, scattering and Hawking radiation of Kerr-Newman black holes in a magnetic field,” *Physical Review D*, vol. 83, p. 024031, 2011.
- [79] K. Jusufi, “Connection Between the Shadow Radius and Quasinormal Modes in Rotating Spacetimes,” *Physical Review D*, vol. 101, no. 12, p. 124063, 2020.
- [80] R. A. Konoplya and A. Zhidenko, “Correspondence between grey-body factors and quasinormal modes,” *Journal of Cosmology and Astroparticle Physics*, vol. 09, p. 068, 2024.
- [81] R. Konoplya and A. Zhidenko, “Correspondence between grey-body factors and quasinormal frequencies for rotating black holes,” *Physics Letters B*, vol. 861, p. 139288, 2025.
- [82] N. Franchini and S. H. Völkel, *Testing general relativity with black hole quasi-normal modes*, pp. 361–416. Springer, 2024.
- [83] D. S. J. Cordeiro, E. L. B. Junior, J. T. S. S. Junior, F. S. N. Lobo, M. E. Rodrigues, D. Rubiera-Garcia, L. F. D. da Silva, and H. A. Vieira, “Free-falling test particles in a charged Kalb-Ramond black hole: Gravitational Doppler effect and tidal forces,” *Phys. Rev. D*, vol. 112, no. 10, p. 104018, 2025.
- [84] P. Crawford and I. Tereno, “Generalized observers and velocity measurements in general relativity,”

General Relativity and Gravitation, vol. 34, pp. 2075–2088, 2002.

- [85] A. Radosz, A. T. Augousti, and K. Ostasiewicz, “The doppler shift in a schwarzschild spacetime,” *Physics Letters A*, vol. 373, pp. 801–803, 2009.
- [86] A. T. Augousti, P. Gusin, B. Kuśmierz, J. Masajada, and A. Radosz, “On the speed of a test particle inside the schwarzschild event horizon and other kinds of black holes,” *General Relativity and Gravitation*, vol. 50, p. 131, 2018.
- [87] A. Radosz, P. Gusin, A. T. Augousti, and F. Formalik, “Inside spherically symmetric black holes or how a uniformly accelerated particle may slow down,” *European Physical Journal C*, vol. 79, p. 876, 2019.
- [88] D. S. J. Cordeiro, E. L. B. Junior, J. T. S. S. Junior, F. S. N. Lobo, M. E. Rodrigues, D. Rubiera-Garcia, L. F. Dias da Silva, and H. A. Vieira, “Free-falling test particles in a charged kalb–ramond black hole: Gravitational doppler effect and tidal forces,” *Physical Review D*, vol. 112, no. 10, p. 104018, 2025.
- [89] C. W. Misner, K. S. Thorne, and J. A. Wheeler, *Gravitation*. San Francisco: W. H. Freeman, 1973.
- [90] S. Chandrasekhar, *The Mathematical Theory of Black Holes*. Oxford: Clarendon Press, 1983.
- [91] R. M. Wald, *General Relativity*. Chicago: University of Chicago Press, 1984.
- [92] E. Poisson, *A Relativist’s Toolkit: The Mathematics of Black-Hole Mechanics*. Cambridge: Cambridge University Press, 2004.
- [93] L. C. B. Crispino, A. Higuchi, L. A. Oliveira, and E. S. de Oliveira, “Tidal forces in reissner–nordström spacetimes,” *Eur. Phys. J. C*, vol. 76, no. 3, p. 168, 2016.
- [94] C.-K. Qiao and P. Su, “Time delay of light in the gravitational lensing of supermassive black holes in dark matter halos,” *Eur. Phys. J. C*, vol. 84, no. 10, p. 1032, 2024.
- [95] N. Heidari, A. A. Araújo Filho, R. C. Pantig, and A. Övgün, “Absorption, scattering, geodesics, shadows and lensing phenomena of black holes in effective quantum gravity,” *Phys. Dark Univ.*, vol. 47, p. 101815, 2025.
- [96] A. A. Araújo Filho, “Analysis of a nonlinear electromagnetic generalization of the Reissner–Nordström black hole,” *Eur. Phys. J. C*, vol. 85, no. 4, p. 454, 2025.
- [97] A. A. Araújo Filho, “Remarks on a nonlinear electromagnetic extension in AdS Reissner–Nordström spacetime,” *JCAP*, vol. 01, p. 072, 2025.
- [98] A. A. Araújo Filho, N. Heidari, I. P. Lobo, and V. B. Bezerra, “Gravitational aspects of a new bumblebee black hole,” *Annals Phys.*, vol. 489, p. 170469, 2026.
- [99] A. Baruah, Y. Sekhmani, S. K. Maurya, A. Deshamukhya, and M. K. Jasim, “Quasinormal modes, greybody factors, and Hawking radiation sparsity of black holes influenced by a global monopole charge in Kalb–Ramond gravity,” *JCAP*, vol. 08, p. 023, 2025.
- [100] A. A. A. Filho, K. Jusufi, B. Cuadros-Melgar, and G. Leon, “Dark matter signatures of black holes

- with Yukawa potential,” *Phys. Dark Univ.*, vol. 44, p. 101500, 2024.
- [101] A. A. A. Filho, K. Jusufi, B. Cuadros-Melgar, G. Leon, A. Jawad, and C. E. Pellicer, “Charged black holes with Yukawa potential,” *Phys. Dark Univ.*, vol. 46, p. 101711, 2024.
- [102] A. A. Araújo Filho, N. Heidari, and F. S. N. Lobo, “Spin effects on particle creation and evaporation in $f(R, T)$ gravity,” 10 2025.
- [103] A. A. Araújo Filho, N. Heidari, I. P. Lobo, and V. B. Bezerra, “Gravitational signatures of a nonlinear electrodynamics in $f(R, T)$ gravity,” *JCAP*, vol. 09, p. 015, 2025.
- [104] A. A. Araújo Filho, N. Heidari, and I. P. Lobo, “Black Hole Gravitational Phenomena in Higher-Order Curvature-Scalar Gravity,” 9 2025.
- [105] C.-Y. Chen and P. Chen, “Gravitational perturbations of nonsingular black holes in conformal gravity,” *Phys. Rev. D*, vol. 99, no. 10, p. 104003, 2019.
- [106] M. Bouhmadi-López, S. Brahma, C.-Y. Chen, P. Chen, and D.-h. Yeom, “A consistent model of non-singular Schwarzschild black hole in loop quantum gravity and its quasinormal modes,” *JCAP*, vol. 07, p. 066, 2020.
- [107] S. Albuquerque, I. P. Lobo, and V. B. Bezerra, “Massless dirac perturbations in a consistent model of loop quantum gravity black hole: quasinormal modes and particle emission rates,” *Classical and Quantum Gravity*, vol. 40, no. 17, p. 174001, 2023.
- [108] A. Al-Badawi and S. K. Jha, “Massless dirac perturbations of black holes in $f(q)$ gravity: quasinormal modes and a weak deflection angle,” *Communications in Theoretical Physics*, vol. 76, no. 9, p. 095403, 2024.
- [109] A. Arbey, J. Auffinger, M. Geiller, E. R. Livine, and F. Sartini, “Hawking radiation by spherically-symmetric static black holes for all spins: Teukolsky equations and potentials,” *Physical Review D*, vol. 103, no. 10, p. 104010, 2021.
- [110] S. Devi, R. Roy, and S. Chakrabarti, “Quasinormal modes and greybody factors of the novel four dimensional gauss–bonnet black holes in asymptotically de sitter space time: scalar, electromagnetic and dirac perturbations,” *The European Physical Journal C*, vol. 80, no. 8, p. 760, 2020.
- [111] C. Gundlach, R. H. Price, and J. Pullin, “Late time behavior of stellar collapse and explosions: 1. Linearized perturbations,” *Physical Review D*, vol. 49, pp. 883–889, 1994.
- [112] M. Skvortsova, “Ringing of extreme regular black holes,” *Gravitation and Cosmology*, vol. 30, no. 3, pp. 279–288, 2024.
- [113] Z.-H. Yang, C. Xu, X.-M. Kuang, B. Wang, and R.-H. Yue, “Echoes of massless scalar field induced from hairy schwarzschild black hole,” *Physics Letters B*, vol. 853, p. 138688, 2024.
- [114] S. V. Bolokhov, “Late time decay of scalar and Dirac fields around an asymptotically de Sitter black hole in the Euler–Heisenberg electrodynamics,” *The European Physical Journal C*, vol. 84, no. 6, p. 634, 2024.

- [115] A. Baruah, A. Övgün, and A. Deshamukhya, “Quasinormal modes and bounding greybody factors of GUP-corrected black holes in Kalb–Ramond gravity,” *Annals of Physics*, vol. 455, p. 169393, 2023.
- [116] C.-Y. Shao, C. Zhang, W. Zhang, and C.-G. Shao, “Scalar fields around a loop quantum gravity black hole in de Sitter spacetime: Quasinormal modes, late-time tails and strong cosmic censorship,” *Physical Review D*, vol. 109, no. 6, p. 064012, 2024.
- [117] A. C. L. Santos, L. A. Lessa, R. V. Maluf, and G. J. Olmo, “Echoes and quasinormal modes of asymmetric black bounces,” *JCAP*, vol. 04, p. 010, 2026.
- [118] B. C. Lütfüoğlu, “Long-lived quasinormal modes, grey-body factors and absorption cross-section of the black hole immersed in the Hernquist galactic halo,” 10 2025.